Synthesis and photophysical investigations of silver nanoparticles inside aqueous and acetonitrile microemulsion

A dissertation

as partial fulfilment of requirement

for the degree of Doctor of Philosophy in Chemistry

by

Debabrata Singha

Roll No: 126122008

Thesis Supervisor: Dr. Kalyanasis Sahu

Department of Chemistry

Indian Institute of Technology Guwahati

Guwahati -781039

India

May 2019

Dedicated to my Grandfather

Late Iresh Chandra Singha

INDIAN INSTITUTE OF TECHNOLOGY GUWAHATI

Department of Chemistry

DECLARATION

I do hereby declare that the work contained in this thesis entitled "***Synthesis and photophysical investigations of silver nanoparticles inside aqueous and acetonitrile microemulsion***" is the outcome of the research work carried out by me under the supervision of Dr. Kalyanasis Sahu, Associate Professor, Department of Chemistry, Indian Institute of Technology Guwahati, India.

In keeping with the general practice of reporting scientific observations, due acknowledgements have been made whenever work described here has been based on the findings of other investigators. This work has not been submitted elsewhere for the award of any degree or diploma.

Dated:

Debabrata Singha
(Senior research scholar)
Department of Chemistry
IIT Guwahati
Assam - 781039, India

INDIAN INSTITUTE OF TECHNOLOGY GUWAHATI

Department of Chemistry

CERTIFICATE

This is to certify that **Debabrata Singha** (Roll No. 126122008) has been working under my supervision since July, 2012 as a Ph. D. student. His thesis entitled **"*Synthesis and photophysical investigations of silver nanoparticles inside aqueous and acetonitrile microemulsion*"** is an authentic record of the results obtained from the research work carried out under my supervision in the Department of Chemistry, Indian Institute of Technology Guwahati, Assam, India. I am forwarding his thesis to submit for the award of degree of Doctor of Philosophy, from this institute. I hereby certify that he has fulfilled all the requirements, according to the rules of this institute regarding the investigations embodied in his thesis and this work has not been submitted elsewhere for a degree.

Dr. Kalyanasis Sahu
(Thesis Supervisor)
Associate Professor
Department of Chemistry
IIT Guwahati
Assam - 781039, India

Acknowledgement

Undertaking this PhD has been truly a life-changing experience for me and it would not have been possible to do without the support and guidance that I received from many people. Firstly, I would like to extend my deepest gratitude to my parents, sister, maternal uncles, my beloved wife ,my mother in law and all my relatives whose sacrifices, love and motivation made on my behalf was what sustained me to strive towards my goal. Secondly, I would like to express my appreciation towards my brother and friend Dillip kumar Sahu, who not only helped me in my research but also given an unimaginable support throughout this journey.

At this stage of ending my PhD, I would like to express my earnest gratitude and respect to the man, who not only introduced me to the fascinating world of Chemistry but also helped in shaping my research carrier with invaluable guidance and expert advice. The man is none other than my PhD supervisor, Dr. Kalyanasis Sahu. His enthusiasm, encouragement and endless efforts have helped me in making this thesis a reality.

I would like to thank my doctoral committee members Prof. G. Krishnamoorthy (Chairman), Prof. Sandip Paul and Dr. A.S. Achalkumar for their valuable suggestions, encouragement and comments that helped a lot in improving my thesis. I would like to express my sincere thanks to Prof. T. Punniyamurthy (HOD), all faculty members, other technical and non-technical staff members of the Department of Chemistry, IIT Guwahati for their continuous support. Special thanks to Center of Instruments Facility, IIT Guwahati to give access to the research facilities.

I would like to thank my lab members Aparajita, Dillip, Sudipta, Tousif, Rabiul, Tapash, Nilanjona and Priyanka for stimulating discussions, encouragement and for all the fun, we have had in this entire journey. I wish all of them success in every aspect of their life. Last but not least I would like to thank all my friends to be with me.

Sincerely

Debabrata Singha

TABLE OF CONTENTS

LIST OF ABBREVIATIONS

AA	Ascorbic Acid
AA-RM	Ascorbic Acid containing Reverse micelles
AgCl NPs	Silver Chloride Nanoparticle
AgNCs	Silver Nanoclusters
AgNPs	Silver Nanoparticles
AgNP-RM	Silver Nanoparticle containing Reverse Micelles
AOT or Aerosol OT	Bis(2-ethylhexyl) sulfosuccinate sodium salt
aq-RMs	Aqueous Reverse Micelles
AuNPs	Gold Nanoparticles
2-AS	2-anthracene sulfonate
4-AP	4-aminophthalimide
BMC	Bi-continuous Microemulsion
CTAB	Cetyltrimethylammonium Bromide
C153	Coumarin 153
C480	Coumarin 480
C343	Coumarin 343
C(t)	Solvent correlation function
DLS	Dynamic Light Scattering
ESPR	Extended Surface Plasmon Resonance
FITC	Fluorescein Isothiocyanate
FL	Fluorescein
FWHM	Full Width at Half Maxima
LSPR	Localized Surface Plasmon Resonance
MNPs	Metal nanoparticles
MIC	Maximum Inhibitory Concentration
NSET	Nanomaterial Surface Energy Transfer
nonaq-RMs	Non-aqueous Reverse micelles
O/W microemulsion	Oil in Water microemulsion
PDI	Polydispersity Index
PF	Plasmon-Fluorophore
QY	Quantum Yield
RMs	Reverse Micelles
REES	Red-Edge Excitation Shift
SPR	Surface Plasmon Resonances
SAF	Safranine O
SERS	Surface Enhanced Raman Spectroscopy
TEM	Transmission Electron Microscopy
TCSPC	Time Correlated Single Photon Counting
TRES	Time Resolved Emission Spectra
TRANES	Time Resolved Area Normalized Spectra
W/O microemulsion	Water in Oil microemulsion
w_0	[water]/[AOT]
w_s	[acetonitrile]/[AOT].
ϕ_f	Quantum Yield
τ_f	Lifetime
σ_{ext}	Extinction Coefficient

SYNOPSIS OF THE THESIS

ABSTRACT

The thesis describes a facile synthesis of silver nanoparticles (AgNPs) within both aqueous and non-aqueous microemulsions with very high optical quality, which are subsequently used to perform several photophysical studies. The content of the thesis has been spread into seven chapters. In *Chapter 1,* a brief introduction of optical properties of metal nanoparticles (MNPs), structural and dynamical characteristics of microemulsions, primarily formed by an anionic surfactant sodium dioctylsulfosuccinate (AOT) and its applications in synthesis of various nanoparticles is provided. Details of instrumental techniques and measurement methods have been summarized in *Chapter 2*. In *Chapter 3*, a facile synthesis protocol is demonstrated to obtain superior optical quality AgNPs inside water/AOT/*n*-heptane reverse micelles (RMs). The growth of the AgNP within the RMs core may severely influence the structural organization of the reverse micellar interface. The modification of the interfacial layer associated with nanoparticle formation has been probed by a solvatochromic probe coumarin 343 (C343) in the *Chapter 4.* In the *Chapter 5,* application of superior optical quality AgNPs is demonstrated in plasmon- fluorophore interaction by exploiting the natural confinement of RM to act simultaneously as a template for AgNP and to host the fluorophores. In the succeeding *Chapters,* I intend to produce high optical quality AgNPs inside a non-aqueous acetonitrile/AOT/*n*-heptane microemulsion. However, nature of the microemulsion template remains debated in the literature and hence, first probed the morphology of the acetonitrile microemulsion at different w_s (= [acetonitrile]/[AOT]) using a solvatochromic probe 4-aminophthalimide (4-AP) in *Chapter* 6. It is observed that the microemulsion undergoes a morphological transition from RM to bicontinuous microemulsion (BMC) above a certain w_s. Finally, in *Chapter* 7, synthesis of AgNPs has been performed in the microemulsion at various w_s and it is found that structural and optical properties of the synthesized AgNPs correlate nicely with the microemulsion template morphology proposed in the *Chapter 6.*

CHAPTER 1: INTRODUCTION

The fascinating optical properties of MNPs arise from surface plasmon resonance (SPR), which are a collective oscillation of free electrons clouds.[1-4] In this chapter, I provided a brief overview of MNPs SPR, theoretical and experimental techniques for SPR measurements, uniqueness of AgNPs SPR compared to all other MNPs and its implications in plasmonic applications. SPR of MNPs has the ability to interact with closely spaced molecular fluorophore and this phenomenon is known as plasmon-fluorophore (PF) interaction.[5-6] The concept and necessary conditions for PF interaction and its implications on various photophysical processes of a fluorophore are discussed. In this chapter, I also reviewed several interesting reports of PF interaction involving various metal nanostructures with an emphasis on the confined systems (MNPs in micelles, block copolymers and RMs).

The nano-confined core of microemulsion acts as a nanoreactor for material synthesis and provide numerous advantage (exceptional control over size, aniosotropy and shape) compared to other synthetic methods.[7-12] Here I provide a brief overview of various types of microemulsion (polar and non-polar) and different phases of microemulsion with RM as sub-phase.[13-15] Numerous surfactants are used in RMs formation however; sodium dioctylsulfosuccinate (AOT) is most popular as RMs are formed without aid of co-surfactant.[13, 16] The structure and properties of AOT RMs and transition of RMs to bi-continuous microemulsion (BMC) are briefly discussed. Here I provide a brief overview of general synthetic procedure, necessary conditions and mechanism of nanoparticles formation inside AOT RM.[9-10, 17] In this chapter, I also reviewed several interesting reports on the optical properties AgNPs synthesized by AOT reverse micellar route. Nanoparticle formation inside AOT RMs induce significant changes in their structural organizations and I presented several interesting reports on this.[7, 18-19]

CHAPTER 2: MATERIALS, METHODS AND INSTRUMENTATION

In this chapter, I mentioned sources of all chemicals that are used in our studies. Various sample preparation procedures, data analysis methods are given. Here I also provided specifications of all the instruments used in our works including UV-Vis

spectroscopy, steady-state and time-resolved fluorescence spectroscopy, transmission electron microscopy (TEM) and dynamic light scattering (DLS) etc.

CHAPTER 3: A FACILE SYNTHESIS OF HIGH OPTICAL QUALITY SILVER NANOPARTICLES BY ASCORBIC ACID REDUCTION INSIDE AOT REVERSE MICELLES

In this *Chapter*, our effort on developing an exceptionally easy method to fabricate high optical quality AgNPs is presented by using ascorbic acid (AA) as a reducing agent inside AOT RM at w_0 values of 2, 6 and 10. For the first time, it is shown that RM can support a chemical reduction that cannot proceed in aqueous medium at room temperature. Simply, addition of $AgNO_3$ and AA solutions into AOT/*n*-heptane mixtures leads to formation of AgNPs at room temperature in the absence of inert atmosphere or prolonged stirring. The optical quality of the SPR band of AgNPs are found to be superior compared to AgNPs obtained by common reducing agents like sodium borohydride or hydrazine under similar conditions. TEM and DLS measurements shows that the nanoparticles are spherical, and are slightly larger than the pure RMs. In addition, the size and the polydispersity gradually increase with increase in the w_0 value.

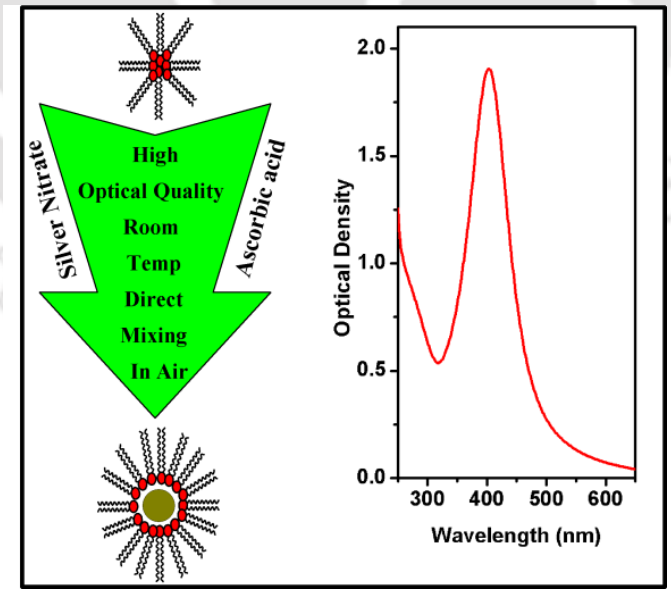

Figure 3.1: Schematic representation of superior optical quality silver nanoparticles synthesized inside water/AOT/n-heptane reverse micellar systems.

CHAPTER 4: SELECTIVE PROBING OF THE INTERFACIAL REGION OF AOT REVERSE MICELLE UPON NANOPARTICLE FORMATION USING DYNAMIC STOKES SHIFT MEASUREMENTS

In the previous *Chapter*, it is demonstrated that superior optical quality AgNPs can be easily synthesized inside AOT reverse micellar assemblies. However, the grown AgNPs may severely influence the structural organization of the original RMs interface. In this *Chapter*, I probed the hydration and organization of the interfacial layer using a site-selective hydrophilic probe, coumarin 343 (C343). I have characterize of the interfacial layer of water/AOT/*n*-heptane RMs before and after AgNPs formation by combination of steady-state absorption, excitation, emission spectroscopy, time-resolved fluorescence anisotropy and dynamic stokes shift measurements. It is observed that both solvation dynamics and rotational dynamics inside the interfacial region of the RM become significantly faster upon AgNPs formation, particularly at low w_0 (at w_0=2) but at higher w_0 values dynamics of the AgNPs containing RM becomes nearly identical to the pure RM. The results indicate that the interfacial region of the RMs becomes more hydrated, less packed upon nanoparticle formation particularly at low w_0 value. The results are in accordance with the significant size change of the RM to accommodate the nanoparticle at low water content.

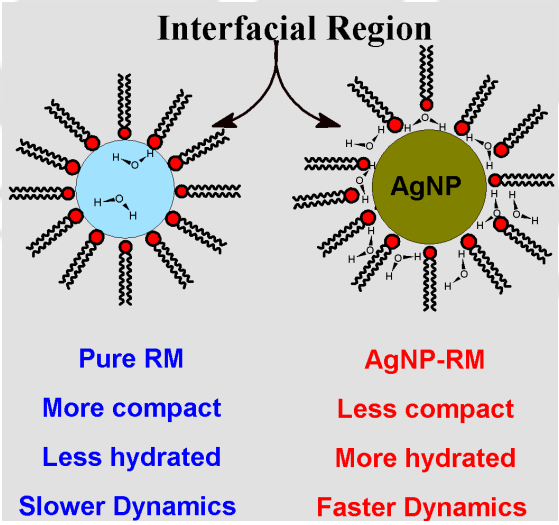

Figure 4.1: A schematic representation of perturbation of reverse micellar interface before and after formation of silver nanoparticles inside the reverse micelles.

CHAPTER 5: INTERACTION OF MOLECULAR TRANSITION WITH SURFACE PLASMON RESONANCE OF SILVER NANOPARTICLE INSIDE RESTRICTED ENVIRONMENT OF AOT REVERSE MICELLE

In this *Chapter*, the utility of high optical quality AgNPs in plasmon- fluorophore interaction is demonstrated by exploiting the natural confinement of a RM to act simultaneously as a template for AgNPs formation and to host the fluorophores. The fluorophores, fluorescein (FL) and safranine O (SAF) and reducing agent (AA) are loaded together into the water pool; thereafter, silver salt was added and subsequently, spectral modification and size evolution are observed by steady-state and time-resolved spectroscopy. In the FL-AgNP composite system, the SPR band of AgNPs undergoes a strong redshift. Moreover, significant modification of both the fluorescence intensity and lifetime of FL is found when AgNPs were gradually formed inside the RM core. On the contrary, in the SAF-AgNP composite, no such effect is noticed and the composite system retains the original optical characteristics of their constituents. This differential effect has been rationalized by dissimilar plasmon-fluorophore coupling in the two systems controlled by a combination of different spatial distribution and spectral detuning of the molecular absorption maxima of the dyes (455 nm and 530 nm for FL and SAF, respectively) from the SPR band maximum (~400 nm) of AgNPs.

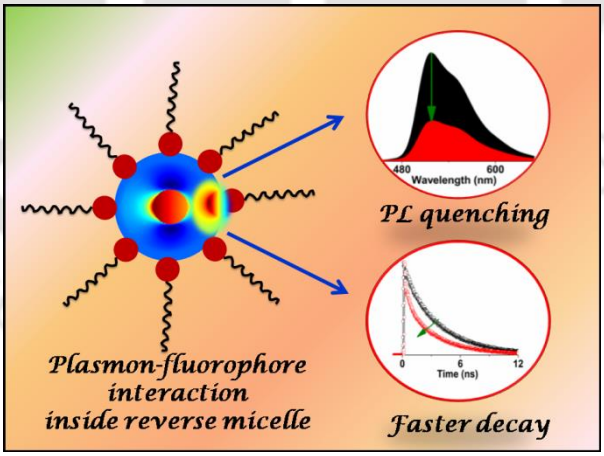

Figure 5.1: A schematic representation plasmon- fluorophore interaction and its implications on the emission properties of fluorescein inside restricted environment of AOT reverse micelles.

CHAPTER 6: ANOMALOUS SPECTRAL BEHAVIOR OF 4-AMINOPHTHALIMIDE INSIDE NON-AQUEOUS ACETONITRILE MICROEMULSION: IMPLICATION ON REVERSE MICELLE TO BI-CONTINUOUS MICROEMULSION TRANSITION

Now I try to explore new methods to produce high optical quality AgNPs in non-aqueous environment. As $AgNO_3$ exhibits very high solubility in acetonitrile, acetonitrile/AOT/*n*-heptane microemulsion is chosen as a template for synthesis of AgNPs. However, microemulsion morphology of the template remains debated in the literature and hence in this *Chapter*, I first investigated the debated acetonitrile/AOT/*n*-heptane microemulsion whether it exists as RMs or BMC, using a hydrophilic solvatochromic fluorophore 4-aminophthalimide (4-AP) at different w_s (= [acetonitrile]/[AOT]). Herein, it is observed that the emission properties vary anomalously at lower and higher w_s regions. The quantum yield (ϕ_f) and lifetime (τ_f) of 4-AP first increase up to w_s = ~1, and thereafter, decrease upon further increase in the w_s values. The emission maximum of 4-AP shifts to higher wavelength from 445 nm at w_s = 0 to 475 nm at w_s = 8. Interestingly, unlike aqueous RMs, the emission maximum at w_s = 1 matches with the emission maximum in neat acetonitrile and the emission maximum shifts to even longer wavelength at higher w_s. Steady-state anisotropy also shows a break around w_s = 1; anisotropy decreases very sharply from w_s = 0 to 1, and

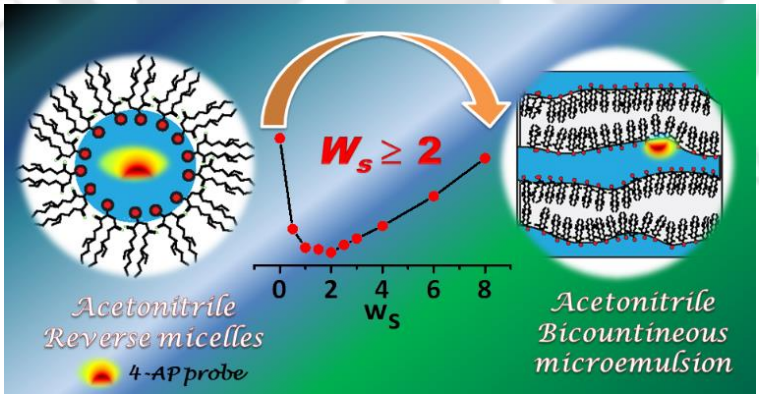

Figure 6.1: Systematic representation of reverse micelles to bi-continuous microemulsion transition of the acetonitrile/AOT/*n*-heptane microemulsion with gradual increment in the acetonitrile content (w_s).

afterward remains constant. Solvation dynamics becomes gradually faster with increase of the acetonitrile content only in the low w_s regimes but remains almost independent of w_s after $w_s > 2$. All of the results clearly indicate that the morphology of the microemulsion may change at an intermediate w_s (~1); below this, the system behaves like RMs and above this, the system may remain as BMC.

CHAPTER 7: HYDROPOBIC SILVER NANOPARTICLE SYNTHESIS INSIDE ACETONITRILE MICROEMULSION AND ITS IMPLICATION IN PROBING THE STRUCTURAL TRANSITION OF THE MICROEMULSION

In the previous *Chapter*, it is observed that acetonitrile/AOT/*n*-heptane microemulsion may undergo structural transition from RM to BMC after certain w_s. Herein, a unique strategy is developed for probing of this transition by using microemulsion itself as a template for synthesis of silver colloids. Precursors (silver nitrate) and reducing agents (AA) are insoluble in *n*-heptane phase and thus, Ag colloids formation occur solely inside the acetonitrile fraction and therefore, the structural morphology of the Ag colloids provides valuable information regarding the structure of the template where Ag colloids formation occur. The synthesized AgNPs were found to be very stable at dry conditions and exhibit very high optical quality compared to all other AOT microemulsion based synthesis methods (both aqueous and non-aqueous).

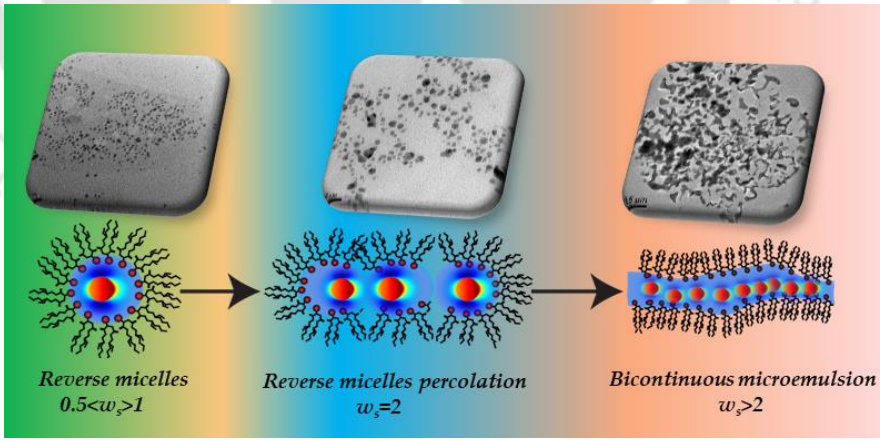

Figure 7.1: Systematic representation of evidence of transformation of reverse micellar structure to the bi-continuous microemulsion of acetonitrile/AOT/n-heptane microemulsion through *in situ* silver nanoparticles synthesized inside systems at different w_s.

At low w_s (≤ 1), synthesized silver colloids exhibits remarkably strong SPR band but the strength of SPR remarkably drops at $w_s = 2$ and almost vanishes at $w_s = 3$. TEM measurements revealed the presence of isolated spherical monodispersed AgNPs of ~6 nm diameter at lower w_s and larger distribution of nanoparticle sizes at $w_s = 2$. Most interestingly, interconnected Ag colloids packed channels were found at $w_s = 3$ which directly shows footprint of the BMC nature of the microemulsion template. Thus, the characteristics of Ag colloids (i.e. size distribution and optical quality) provide valuable information about interfacial structure of the microemulsion and suggested that microemulsion switches from RM to BMC nature at an intermediate w_s.

SUMMARY AND FUTURE OUTLOOK

In the present thesis a facile synthesis method has been developed to obtain high optical quality AgNPs inside aqueous and non-aqueous (acetonitrile) AOT microemulsion. This has been achieved by using a mild reducing agent ascorbic acid (AA). To the best of our knowledge, the optical quality of the AgNPs synthesized by this route was found to be much superior than previously reported other aqueous and non-aqueous AOT microemulsion routes. The synthesized AgNPs were found to be highly stable, redispersable and even retained optical quality in coated form. The high optical quality of AgNPs is effectively used in selective probing the interfacial region of microemulsion, plasmon-fluorophore interaction and probing acetonitrile microemulsion structure. This work is expected to open new avenue towards synthesis of various other metal nanoparticles, bimetallic nanoparticles, metal oxides and sulphide nanoparticles etc. It will be very interesting to see the optical properties of other metal nanoparticles especially copper and gold synthesized by this route. A detailed summary and future outlook is provided in the end of the thesis.

REFERENCES

1. Mulvaney, P., Surface Plasmon Spectroscopy of Nanosized Metal Particles. *Langmuir* **1996**, *12*, 788-800.
2. Kelly, K. L.; Coronado, E.; Zhao, L. L.; Schatz, G. C., The Optical Properties of Metal Nanoparticles: The Influence of Size, Shape, and Dielectric Environment. *J. Phys. Chem. B* **2003**, *107*, 668-677.
3. Henry, A.-I.; Bingham, J. M.; Ringe, E.; Marks, L. D.; Schatz, G. C.; Van Duyne, R. P., Correlated Structure and Optical Property Studies of Plasmonic Nanoparticles. *J. Phys. Chem. C* **2011**, *115*, 9291-9305.
4. Mayer, K. M.; Hafner, J. H., Localized Surface Plasmon Resonance Sensors. *Chem. Rev.* **2011**, *111*, 3828-3857.
5. Lakowicz, J. R., *Principles of Fluorescence Spectroscopy*; Springer: New York, 2006.
6. Lakowicz, J. R.; Ray, K.; Chowdhury, M.; Szmacinski, H.; Fu, Y.; Zhang, J.; Nowaczyk, K., Plasmon-Controlled Fluorescence: A New Paradigm in Fluorescence Spectroscopy. *Analyst* **2008**, *133*, 1308-1346.
7. Setua, P.; Ghatak, C.; Rao, V. G.; Das, S. K.; Sarkar, N., Dynamics of Solvation and Rotational Relaxation of Coumarin 480 in Pure Aqueous-Aot Reverse Micelle and Reverse Micelle Containing Different-Sized Silver Nanoparticles inside Its Core: A Comparative Study. *J. Phys. Chem. B* **2012**, *116*, 3704-3712.
8. Wang, C.-y.; Liu, C.-y.; Wang, Y.; Shen, T., Spectral Characteristics and Photosensitization Effect on Tio2of Fluorescein in Aot Reversed Micelles. *J. Colloid. Int. Sci.* **1998**, *197*, 126-132.
9. Zhang, W.; Qiao, X.; Chen, J., Synthesis and Characterization of Silver Nanoparticles in Aot Microemulsion System. *Chem. Phys.* **2006**, *330*, 495-500.
10. Zhang, W.; Qiao, X.; Chen, J.; Wang, H., Preparation of Silver Nanoparticles in Water-in-Oil Aot Reverse Micelles. *J. Colloid. Int. Sci.* **2006**, *302*, 370-373.
11. Solanki, J. N.; Murthy, Z. V. P., Controlled Size Silver Nanoparticles Synthesis with Water-in-Oil Microemulsion Method: A Topical Review. *Industrial and Engineering Chemistry Research* **2011**, *50*, 12311-12323.
12. Petit, C.; Lixon, P.; Pileni, M. P., In Situ Synthesis of Silver Nanocluster in Aot Reverse Micelles. *J. Phys. Chem.* **1993**, *97*, 12974-12983.
13. Correa, N. M.; Silber, J. J.; Riter, R. E.; Levinger, N. E., Nonaqueous Polar Solvents in Reverse Micelle Systems. *Chem. Rev.* **2012**, *112*, 4569-4602.
14. Elles, C. G.; Levinger, N. E., Reverse Micelles Solubilizing Dmso and Dmso/Water Mixtures. *Chem. Phys. Lett.* **2000**, *317*, 624-630.
15. Riter, R. E.; Undiks, E. P.; Kimmel, J. R.; Levinger, N. E., Formamide in Reverse Micelles: Restricted Environment Effects on Molecular Motion. *J. Phys. Chem. B* **1998**, *102*, 7931-7938.
16. Brown, D.; Clarke, J. H. R., Molecular Dynamics Simulation of a Model Reverse Micelle. *J. Phys. Chem.* **1988**, *92*, 2881-2888.
17. Bagwe, R. P.; Khilar, K. C., Effects of Intermicellar Exchange Rate on the Formation of Silver Nanoparticles in Reverse Microemulsions of Aot. *Langmuir* **2000**, *16*, 905-910.

LIST OF PUBLICATIONS

Paper included in this thesis:

1. **Singha, D.;** Barman, N.; Sahu, K., A Facile Synthesis of High Optical Quality Silver Nanoparticles by Ascorbic Acid Reduction in Reverse Micelles at Room Temperature. *J. Colloid. Int. Sci.* **2014**, *413*, 37-42.
2. **Singha, D.;** Barman, N.; Phukon, A.; Sahu, K., Selective Probing of Reverse Micelle Interfacial Layer Upon Silver Nanoparticle Formation Using Dynamic Stokes Shift Measurements. *J. Phys. Chem. C* **2014**, *118*, 10366-10374.
3. **Singha, D.;** Sahu, D. K.; Sahu, K., Coupling of Molecular Transition with the Surface Plasmon Resonance of Silver Nanoparticles inside the Restricted Environment of Reverse Micelles. *ACS Omega* **2017**, *2*, 5494-5503.
4. **Singha, D.;** Sahu, D. K.; Sahu, K., Anomalous Spectral Modulation of 4-Aminophthalimide inside Acetonitrile/AOT/n-Heptane Microemulsion: New Insights on Reverse Micelle to Bicontinuous Microemulsion Transition. *J. Phys. Chem. B* **2018**, *122*, 6966-6974.
5. **Singha, D.;** Sahu, D. K.; Sahu, K., Probing the Interfacial Transition of Acetonitrile/AOT/*n*-heptane Microemulsion Through *in situ* Silver Colloid Synthesis**.** *Colloids Surf. A* ***2019****, 574, 171-177.*

Paper not included in this thesis:

1. Barman, N.; **Singha, D.**; Sahu, K., Fluorescence Quenching of Hydrogen-Bonded Coumarin 102-Phenol Complex: Effect of Excited-State Hydrogen Bonding Strength. *J. Phys. Chem. A* **2013**, *117*, 3945-3953**.**
2. Barman, N.; **Singha, D**.; Sahu, K., Faster Photoinduced Electron Transfer in a Diluted Mixture Than in a Neat Donor Solvent: Effect of Excited-State H-Bonding. *Phys. Chem. Chem. Phys.* **2014**, *16*, 6159-6166.
3. Sahu, D. K.; **Singha, D**.; Sahu, K., Sensing of Iron(Iii)-Biomolecules by Surfactant-Free Fluorescent Copper Nanoclusters. *Sens Biosensing Res.* **2019**, *22*, 100250.

LIST OF CONFERENCE PROCEEDINGS

1. International Conference on Advanced Nanomaterial and Nanotechnology (**ICCAN 2013).**
   Organized by center of Nanotechnology, Indian institute of technology, Guwahati.
2. Recent Trends in Fundamental and Applied Chemical Sciences ***(RTFACS-14)***
   Organized by Dibrugarh University
3. International Symposium Advances in Spectroscopy and Ultrafast Dynamics ***(ASUD 2014)***.
   Organized by Indian Association of Cultivation of Science, Kolkata.
4. Frontiers in Chemical Sciences ***(FICS 2014)***
   Organized by department of chemistry, Indian institute of technology, Guwahati.
5. **Reflux 2015.**
   Organized by department of chemical engineering, Indian institute of technology, Guwahati.
6. **Reflux 2018.**
   Organized by department of chemical engineering, Indian institute of technology, Guwahati.

LIST OF SCHEMES

Scheme 6.1: Representation of RM and bi-continuous microemulsion models along with the chemical structures of the surfactant sodium 1,4-bis(2-ethylhexyl)sulfosuccinate (AOT) and the fluorophore 4-aminophthalimide (4-AP).

Scheme 6.2: Systematic conversation of acetonitrile/AOT/*n*-heptane reverse microemulsion to bi-continuous microemulsion with gradual addition acetonitrile.

Scheme 7.1: Template-directed expected growth of silver nanoparticles within acetonitrile/AOT/*n*-heptane microemulsion at different w_s.

LIST OF FIGURES

implication in PF interaction. (b) Probe location dependent interaction between 2-AS (fluorophore) and AuNPs in micelles of triblock copolymers of F127 and P123.

Figure 1.9: Schematic representation modification of microemulsion structures from w/o droplets to o/w droplets with increase in the amount of water content (w_0). Note that there is an intermediate phase where oil and water together known as bi-continuous phase.

Figure 1.10: Comparison of optical quality of the AgNPs SPR band at w_0=10 by the work of (a) Petit et al. with (b) Bagwe et al work. Petit et al. used $NaBH_4$ reduction in NaAOT by using(– – –) silver nitrate and (–) silver sulfosuccinate as silver precursor, $[AOT]_{total}$=0.1 M; $[AgNO_3]$= [AgAOT]=10^{-3} M, $[NaBH_4]$= 10^{-4} M. Bagwe et al used $NaBH_4$ reduction in NaAOT by using silver nitrate as a precurssor, $[AgNO_3]$= 1.8×10^{-3} M, $[NaBH_4]$= 9×10^{-4} M in presence of different surfactant additives.

Figure 1.11: Spectra showing (a) a relation between of SPR bandwidth with particle diameters synthesized by AOT microemuslion route using $NaBH_4$ and N_2H_4 (hollow circle) as reducing agents. The dash line represents Mie simulation curve. (b) Variation of SPR peak with w_0 values of AOT microemulsion. Note that a blue shift in SPR maxima is noticed with increase in w_0 values.

Figure 1.12: Schematic representation of probing of AOT reverse micellar interface before and after AgNPs formation inside (a) non-aqueous ethylene glycol and (b) aqueous reverse micelles**.**

Figure 3.1: The UV-Vis spectra of water/AOT/n-heptane reverse micellar systems at w_0 = 2,6 and 10 containing different additives- (a) water, (b) 0.3 mM $AgNO_3$, (c) 0.3 mM $AgNO_3$ and 0.01 mM AA, (d) 0.3 mM $AgNO_3$ and 0.05 mM AA, (e) 0.3 mM $AgNO_3$ and 0.10 mM AA, and (f) 0.3 mM $AgNO_3$ and 0.20 mM AA. All concentrations represent the overall concentration. The inset represents snapshots of these solutions when viewed under ordinary light.

Figure 3.2: Comparison of the UV-Vis spectra of the AgNP formed in the water/AOT/n-heptane reverse micellar systems at different w_0 values (a) w_0 = 2, (b) w_0 = 6, and w_0 = 10. The overall concentrations of AOT, $AgNO_3$ and AA were 90, 0.30

and 0.10 mM, respectively. The inset represents snapshots of these solutions when viewed under ordinary light.

Figure 3.3: Comparison of optical quality of SPR band of AgNP at w_0 =10 obtained in this work with Petit et al (a) Present work by AA reduction using [AOT]=0.09 M, $[AgNO_3]=0.3\times10^{-3}$ M, $[AA]=0.5\times10^{-4}$ M (b) By Petit et al. via $NaBH_4$ reduction in NaAOT by using(– – –) silver nitrate and (–) silver sulfosuccinate as silver precursor. $[AOT]_{total}$=0.1 M; $[AgNO_3]$= [AgAOT]=10^{-3} M, $[NaBH_4]$= 10^{-4} M

Figure 3.4: UV-Vis spectra of the AgNPs formed in the water/AOT/n-heptane reverse micellar systems at w_0 = 6 showing the effect of different reducing agents (top) $NaBH_4$ and (bottom) $N_2H_4.H_2O$ at different concentrations of the reducing agents; 0.05, 0.1, 0.3 mM. The overall concentrations of AOT and $AgNO_3$ were 90 and 0.30 mM, respectively. The inset represents snapshots of these solutions when viewed under ordinary light.

Figure 3.5: Size distributions obtained from dynamic light scattering (DLS) measurements at different w_0 values for pure reverse micelles, and reverse micelles containing the synthesized AgNPs.

Figure 3.6: TEM images and size distribution histograms of AgNPs synthesized by AA reduction at (a) w_0 = 2, (b) w_0 = 6 and (c) w_0 = 10, respectively. The overall concentrations of $AgNO_3$ and AA were 0.30 and 0.10 mM, respectively.

Figure 4.1: The UV-visible spectra of water/AOT/n-heptane reverse micellar system at w_0 = 6 comprising (a) AgNPs only (black), (b) C343 and AgNPs (red), (c) C343 only (blue). The green curve represents the difference spectrum [(b)-(c)]. The absorption spectrum of C343 in the pure reverse micelle and the difference spectrum are compared in a magnified scale in the inset.

Figure 4.2: Emission spectra of coumarin 343 (C343) at various excitation wavelengths (λ_{ex}) for the pure and the AgNP containing RMs at w_0= 2. The plot of the emission maxima against λ_{ex} for the two cases are shown in the inset.

Figure 4.3: Absorption spectrum (black), excitation spectra using a standard 10 mm cuvette (red) and in a glass capillary tube (0.8 mm internal diameter) (green) of C343

in pure RMs (top panel) and in AgNP containing RMs at $w_0 = 2$ (bottom panel). The excitation spectra are recorded at an emission wavelength of 490 nm.

Figure 4.4: TEM images and size distribution histograms of the AgNPs in RMs at w_0=6 in (a) the absence of C343 (top) (b) in the presence of 10 µM C343 (bottom).

Figure 4.5: Fluorescence anisotropy decays, r(t) of C343 recorded at 470 nm and excited at 405 nm in the pure RMs (RM, black) and in the silver nanoparticle containing RMs (AgNP-RM, blue) at different w_0 values.

Figure 4.6: Decay of the solvent response function, C(t) of C343 in pure (o) and silver nanoparticle containing (o) RMs at w_0 values of 2, 6 and 10. The points represent the actual values while the solid lines denote the best fit to bi-exponential decay.

Figure 4.7: Time resolved emission spectra (TRES) and time resolved area-normalised emission spectra (TRANES) spectra of the C343 at different time in pure (RM) and silver nanoparticle containing (AgNP-RM) reverse micellar system at $w_0 = 6$.

Figure 5.1: Evolution of extinction spectra of different systems with time: (a) AgNP inside AOT reverses micelle, (b) AgNP and safranin O in RM (c) AgNP and fluorescein in RM. The variation of SPR maxima with time for various systems is added in plot (d).

Figure 5.2: Normalized UV-visible extinction spectra of only AgNP, only fluorophore and AgNP-fluorophore composite and calculated combined (AgNP+fluorophore) extinction spectrum. Safranine O (SAF) and fluorecein (FL) are respectively used in the top and bottom panels. Extinction spectrum of the AgNP-SAF system has strong similarity with the comibed spectrum but the extinction spectrum of the AgNP-FL system deviates much from the calculated spectrum.

Figure 5.3: Dynamic light scattering measurements of FL-AgNPs composites at different time.

Figure 5.4: Variation of steady state excitation (left panel) and emission intensity of safranin (λ_{ex}= 510, λ_{em}= 570 nm) and fluorescein (λ_{ex}= 445 nm, λ_{em}= 530 nm) in the presence of growing silver nanoparticle with time inside reverse micellar solution. Inset of right panel shows normalized intensity of respective fluorophore and arrow indicates

increase in shoulder peak with time. For clear visibility of peak position in excitation spectrum only spectra before and after complete growth of AgNPs are provided.

Figure 5.5: Fluorescence anisotropy decays, r(t), of safranin (λ_{ex}= 510 nm, λ_{em}= 565 nm) and fluorescein (λ_{ex}= 405 nm, λ_{em}= 520 nm) before and after complete growth of AgNPs.

Figure 5.6: Fluorescence decays of safranin (λ_{ex}= 510 nm, λ_{em}= 565 nm) and fluorescein (λ_{ex}= 405nm, λ_{em}= 520 nm) inside AOT reverse micellar solution, before and after AgNPs nanoparticle formation.

Figure 6.1: (a) Absorption spectra of 4-AP in acetonitrile/AOT/*n*-heptane microemulsion at different w_s. Absorption spectrum of neat acetonitrile (dotted line) is also included for comparison (b) Emission spectra ($\lambda_{ex.}$=360 nm) of 4-AP in acetonitrile/AOT/*n*-heptane microemulsion at different w_s values. Inset shows emission maxima (in nm) vs w_s plot.

Figure 6.2: Variation of the red-edge excitation shift (REES, Δν in nm) of 4-AP inside acetonitrile/AOT/*n*-heptane microemulsion with gradual increment in the w_s. Inset shows emission spectra of 4-AP at various excitation wavelengths (λ_{ex}) at w_s = 1

Figure 6.3: Steady state fluorescence anisotropy (left panel) of 4-AP inside acetonitrile/AOT/*n*-heptane microemulsion at various acetonitrile contents measured at the emission maxima (λ_{ex}=360 nm). Fluorescence decays of 4-AP (right panel) inside acetonitrile/AOT/*n*-heptane microemulsion at various w_s measured at the corresponding emission maximum (λ_{ex} = 375 nm).

Figure 6.4: The relative shift in time resolved emission maxima $\Delta\,\lambda_{em}^{max} = \lambda_{em}^{max}\,(t = 60\,ns) - \lambda_{em}^{max}\,(t = 0.1\,ns)$ of probe 4-AP in acetonitrile/AOT/*n*-heptane microemulsion at different w_s.

Figure 6.5: (a) Emission spectra and (b) emission maxima (λ_{max}) of 4-AP($\lambda_{ex.}$=360 nm) in acetonitrile solvent as a function of AOT concentration.

Figure 6.6: Hydrodynamic diameter of acetonitrile/AOT/*n*-heptane microemulsion at different w_s values obtained from dynamic light scattering (DLS) measurements. At

low w_s (0-1), mostly single size distribution exists (a) but at high w_s, distribution becomes highly polydispersed (b).

Figure 7.1: The UV-Vis spectra of Ag colloids formed in the acetonitrile/AOT/*n*-heptane microemulsions at w_s = 0.5, 1, 2 and 3. The concentration of $AgNO_3$ and AA is fixed at 0.3 mM and 0.20 mM, respectively. Photographs of each solution are given in the inset.

Figure 7.2: Hydrodynamic diameter of acetonitrile/AOT/*n*-heptane microemulsion at different w_s values obtained from DLS measurements in absence of silver nanoparticles (a) and in presence of AgNP (b). The concentration of $AgNO_3$ and AA is fixed at 0.3 mM and 0.20 mM, respectively.

Figure 7.3: TEM images and size distribution histograms of Ag colloids synthesized by AA reduction at w_s = 0.5, 1, 2 and 3 respectively. The overall concentrations of $AgNO_3$ and AA are 0.30 and 0.20 mM, respectively. Histograms are generated by excluding larger AgNP aggregates and TEM micrograph at w_s =3 are represented in lower resolution (500 nm scale bar).

Figure 7.4: Comparison of UV-Vis spectra of as prepared AgNPs formed in the acetonitrile/AOT/*n*-heptane microemulsions at w_s=0.5 and after evaporation followed by re-dispersing in n-heptane. Photographs of as prepared, evaporated and re-dispersed solutions are given in the inset.

भारतीय प्रौद्योगिकी संस्थान गुवाहाटी
Indian Institute of Technology Guwahati

Chapter-1

Introduction

CHAPTER 1: INTRODUCTION

1.1. OPTICAL PROPERTIES OF METAL NANOPARTICLES

Metal nanoparticles (MNPs) are neither unknown nor a new area of research; they are around us since ancient times. The unique size-dependent light absorbing and scattering properties of MNPs found extensive applications in various decorating substances to display beautiful vivid colours. These fascinating colours (or optical properties) of MNPs have been attracting people for centuries. One of the oldest examples is Lycurgus cup (Byzantine Empire, 4th century). When light is shone on the cup, it appears to be red when viewed through transmitted direction but appears to be green in reflected direction (**Figure 1.1**).[1] The underlying fact is that sidewall of cup is embedded with silver and gold nanoparticles (Ag/Au NPs) with diameter ~100 nm and their surface plasmon resonance (SPR) is responsible for such anomalous behaviours, may not be understood at that time.[1-2] Although, the optical properties of MNPs are used for centuries, however the scientific knowledge have emerged recently with increasing understanding of the atomic world. Presently, MNPs are not merely limited to the field of optics but are used in diverse areas like catalysis,[3-4] biological imaging and therapy,[5-6] sensing,[7] detection,[8] molecular switches,[9] antimicrobial action,[10-11] and so on.

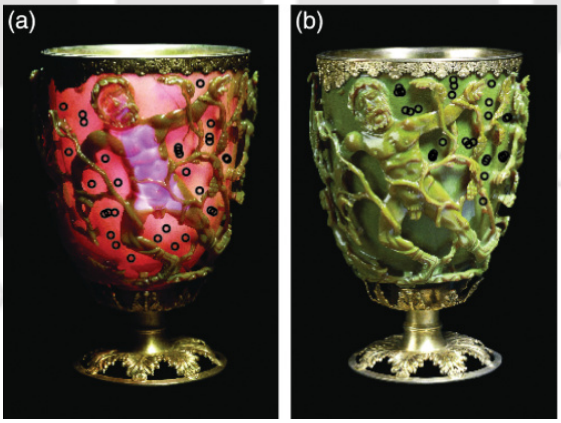

Figure 1.1: Lycurgus cup in British Museum appears to be (a) red in transmission direction and (b) green in reflected direction of light (reproduced with permission).[1]

1.1.1. Surface Plasmon Resonance

The MNPs exhibit vivid colours as it can support plasmon, which define as collective oscillations of electron clouds near MNP surface. When the size of MNPs

are ≤ 100 nm, the surface plasmonic resonance (SPR) band falls in the visible regions of the spectrum and hence MNPs are coloured. A brief overview of SPR phenomena is presented here. However, it is not intend to cover the entire theoretical details of plasmonic resonance, as such details are available in numerous other review articles.[12-15]

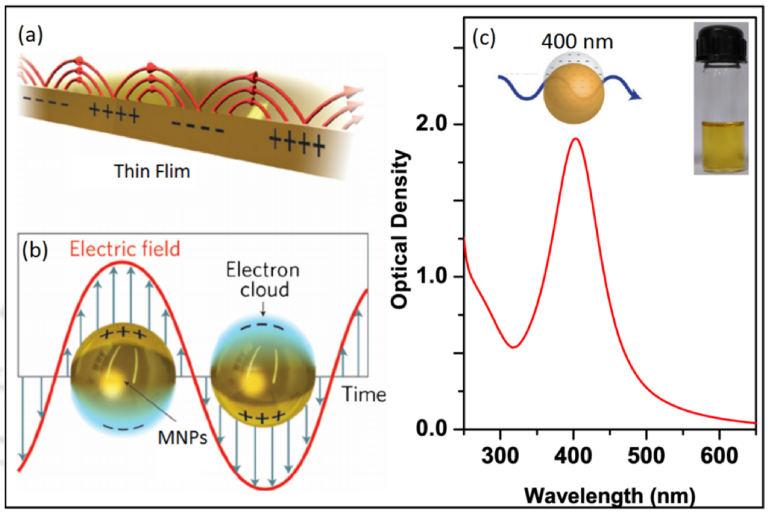

Scheme 1.1: Schematic representations of (a) propagating surface plasmon resonance at thin metal surface,[16] (b) localized surface plasmon resonance on metal nanoparticles,[16] (c) UV-visible spectrum of the silver nanoparticle solution along with image of the solution viewed under ordinary light and schematic representation of plamonic oscillation of the electronic clouds around nanoparticle surface (reproduced with permission).[17-18]

A metal sheet is composed of periodic arrangements of positive lattice (or nuclei) containing loosely bound electron densities held together by columbic force of attraction. When an electromagnetic radiation of appropriate frequency falls on the material surface, the electric field component of the electromagnetic radiation undergoes coupling with surface electron densities of MNPs, which result in the displacement of electron densities form the MNPs surface. Simultaneously, the positive metal lattice attracts the electron densities towards itself, as a result of this phenomena a coherent oscillation of electron densities are produced and the oscillations are termed as SPR.[12-13, 15, 19-20] Since, positive lattice acts as a restoring force and hence, SPR entirely depends on the type of positive lattice (or the material used). Moreover, SPR can produce enormous electromagnetic field which can travel beyond the lattice to the

medium and hence, SPR also depends on the dielectric medium around the material. In thin materials, the SPR can propagate through the material and hence termed as propagating or extended surface plasmon resonance (ESPR) as shown in the **Scheme 1.1**. Interestingly, ESPR can absorb light in the infrared region and rest of the light is reflected back and therefore these martial are reflective and appeared shinny.[21-23]

MNPs can be considered as an ultra-small portion above metal lattice that are even smaller than wavelength of the incident electromagnetic radiation. MNPs primarily display two distinct differences over a thin film, first it can undergo instantaneous excitation with incident light, and secondly the surface curvature of MNPs are no longer in a plane with respect to incident electromagnetic radiations. Due to this curvature shape, plasmons not able to propagate and become confined within the particle surface and hence, they termed as localized surface plasmon resonance (LSPR). Unlike ESPR, LSPR falls in visible region and hence MNPs are colored.[12, 17, 21] For example, **Scheme 1.1c** shows dark yellow coloured of AgNPs solution with diameter ~5 nm.[18] The UV-visible spectrum of the AgNPs dispersion indicates that dark yellow colour is primarily due to the SPR band with a maximum at ~400 nm.

1.1.2. Experimental aspects of SPR

Primarily two phenomena are associated with SPR of MNPs far field and near field.[14-16] Far field properties are mainly manifested in the absorption/extinction spectra of MNPs and can be measured simply with UV-VIS-NIR spectrophotometer by taking solution, or thin film of MNPs immobilized in the optically transparent glass or quartz plate. **Figure 1.2** shows extinction spectra and colours of AgNPs solutions of different diameters.[24] It is apparent from the figure that the peak positions and spectral widths of SPR depend on the size of the nanoparticles; with increase in the size a red shift in SPR peak is noticed. MNPs has the ability to absorb as well as scatter incident light and hence the overall absorption (for MNPs referred as extinction) spectra comprises of both absorption and scattering constituents of the MNPs.

MNPs are polydisperse in nanoscopic regimes and hence the overall extinction spectrum represents an ensemble average of the all SPR spectra.[15, 21, 25] However, nowadays it is also possible to record SPR in single particle domain, usually a dark field microscope in conjunction with a UV-VIS-NIR spectrophotometer is used to record

SPR of an individual nanoparticle. For example, **Figure 1.2c** shows a comparison of the SPR spectrum of silver nanocube dispersion in water (ensemble average) and in single particle domain measured by dark field microscopy.[25] Moreover, near field properties can also be measured with a number of techniques, such as, near field scanning optical microscopy (NSOM),[26] electron density loss spectroscopy (EELS),[27] energy filtered transmission electron microscopy (EFTEM)[28] and so on. In addition to these methods, currently surface enhanced Raman spectroscopy (SERS) becomes very popular method in probing near field properties.[29-30]

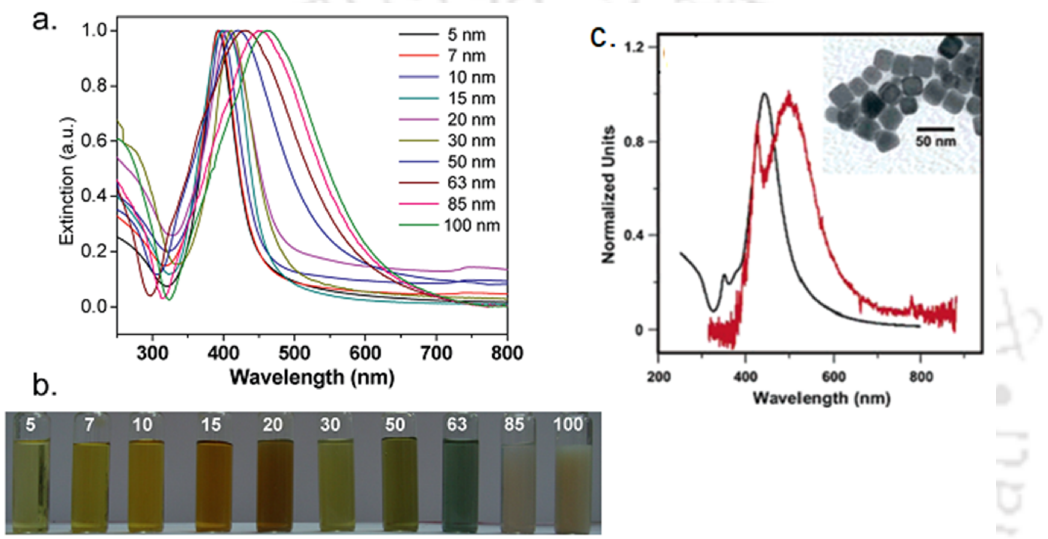

Figure 1.2: (a) UV-vis extinction spectra and (b) colours of different sized silver nanoparticles in water.[24] (c) Comparison of SPR spectra silver nanocubes ensemble average extinction spectra (black) and spectra of single silver nanocube under dark field scattering (red) in water (reproduced with permission).[25]

1.1.3. Theoretical aspects of SPR

In the beginning of 20th century, Gustav Mie proposed a theory in order to explain the interaction of light with matter having size smaller than wavelength of the incident radiation, popularly known as "Mie theory".[31] The extinction cross-section of a spherically symmetric sphere can be simulated with the help of Mie equation as[14-15]

$$C_{ext} = \frac{24\pi^2 R^3 \varepsilon_m^{3/2}}{\lambda}\left[\frac{\varepsilon_2}{(\varepsilon_1+2\varepsilon_m)^2+\varepsilon_2^2}\right] \qquad (1.1)$$

Where C_{ext} is extinction cross section of a sphere of radius R, ε_m is dielectric constant of the medium, ε_1 and ε_2 are real and imaginary part of the complex metal dielectric function, λ wavelength of the incident electromagnetic radiation. Mie theory was successfully used in simulating the optical properties of numerous nanoparticles. For examples, Bilankohi used Mie theory to simulate extinction cross-section of AgNPs at different wavelengths (**Figure 1.3a).**[32] Apart from Mie theory several others simulation methods such as discrete dipole approximation (DDA), boundary element method (BEM), finite-difference time-domain (FDTD), finite element method (FEM), time dependent density functional theory (TD DFT) etc. are regularly used in simulating the optical properties of MNPs .[14-16, 21, 23, 33]

1.1.4. Unique optical properties of AgNP compared to other MNPs

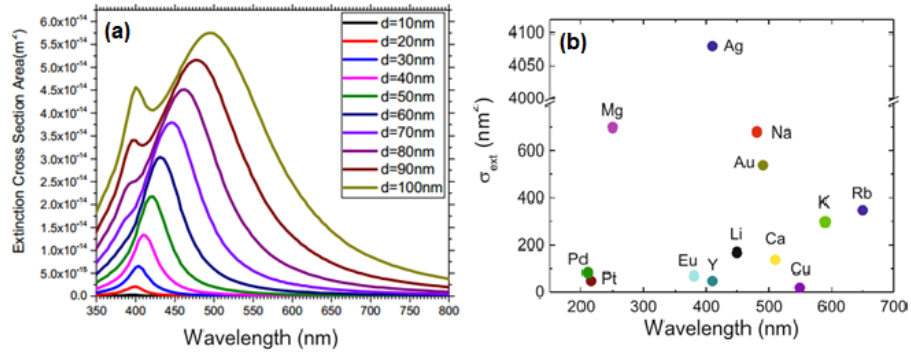

Figure 1.3: (a) Mie simulation of extinction cross-section of silver nanoparticles at different wavelengths with different size.[32] (b) Resonance frequencies and extinction cross-sections of various MNPs with 10 nm size embedded inside silica (reproduced with permission).[34]

AgNP exhibits several unique optical properties compared to other MNPs. The SPR of AgNP appears in the visible region; extinction cross-section is highest among the all the MNPs (**Figure 1.3b)** etc. Although, NaNPs and MgNPs have high extinction cross-sections values (**Figure 1.3b)** but they get easily oxidized and hence considered as unstable for plasmonic applications.[34] Another important aspects MNP is CuNPs, however instability and poor SPR are the two major limitations associated with it. Interestingly, extinction cross-section of AgNPs is approximately seven times higher than AuNPs. Such a high value arises due to the fact that AgNPs exhibits larger negative real part of metal dielectric function than AuNPs.[15, 29] Hence AgNPs is usually preferred over AuNPs in plasmonic applications.[19, 32] However, due to bio-inertness, AuNPs is

preferred over AgNPs for in vivo applications.[15] For large-scale applications, cost of the material is also an important factor. Both Al and Cu are cheaper than Ag however; they have serious limitations due to lower extinction cross-section value. Due to excellent plasmonic properties, diverse nanostructures and material cost AgNPs usually preferred in plasmonics over AuNPs.

Besides plasmonic applications, AgNPs sustains ever-green research interest in catalysis,[3-4, 35] antimicrobial action,[10-11] biological imaging,[5, 36] water purification and splitting,[37-38] nanofluids,[39] photothermal therapy,[19,32] and so on. The applications of AgNPs are extremely size specific. For example, Agnihotri et al. have shown size specific antimicrobial action of AgNPs on various bacterial strains.[24] They found that MIC (maximum inhibitory concentration) value of 5 nm AgNPs is ~20 μg ml^{-1} which is almost six times lower than 100 nm particles (~110 μg ml^{-1}).

1.2. PLASMON FLUOROPHORE INTERACTION

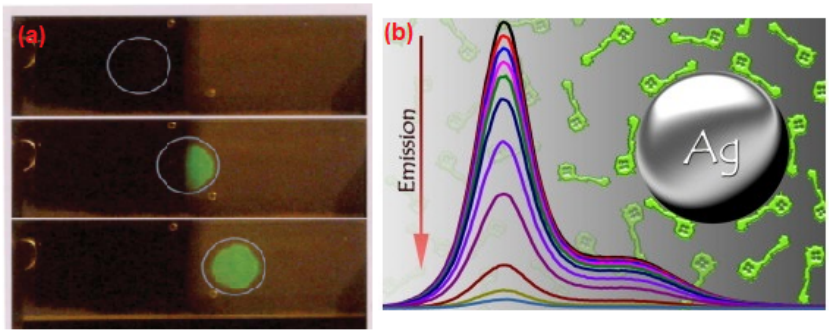

Figure 1.4: Effects of AgNPs on emission properties of (a) surface bound fluorescein-labelled protein and (b) chlorophyll extracts respectively.[19] Uncoated and AgNPs coated portions represents by left and right side of the slide. Fluorescein exhibits emission enhancement whereas chlorophyll displayed quenching (reproduced with permission).

SPR has the ability to trap and concentrate light and can produce enormous electromagnetic fields near the MNP surface (**Section 1.1.1**). The enhanced fields interacts with nearby fluorophores and thus can alter the radiative decay rates of an emitter. Based on the distance between nanoparticle surface and fluorophore, both quenching as well as emission enhancement is reported. Plasmon-fluorophore (PF) interaction produces unique optical properties in the composite that are entirely different from their constituents and have found extensive applications in optical signal

modification,[40-41] cellular imaging and photodynamic therapy,[6, 42] sensing,[7, 43] infrared detection,[8] molecular switches [9] and so on. In order to explain PF interaction, extensive utilization of electrodynamic theories are required, which may be still inadequate to explain the actual phenomena.

Lakowicz and co-workers described PF interaction as "radiative decay engineering", because the radiative rates of the fluorophores can be engineered in the presence of MNPs.[19, 44] Molecular fluorophores in a free space acts like an oscillating dipole. When a nearby metallic surface interacts with an oscillating dipole, the electric field felt by the fluorophore gets drastically modified. This interaction can either increase or decrease the incident electric field experienced by the fluorophore and hence may either increase or decrease the radiative decay rates. For example, **Figure 1.4** shows the effect of AgNPs on emission properties of fluorescein and chlorophyll. It is apparent that AgNPs coated fluorescein shows remarkable brighter emission compared to uncoated side. On other hand, the fluorescence of chlorophyll exhibits substantial quenching.[45-47] Several advantages are associated with metal-enhanced fluorescence over traditional fluorescence measurements such as high efficiency of fluorescence emission, better detection sensitivity, protection against fluorophore photobleaching at high laser power, applicable to both intrinsic and extrinsic fluorophores and so on.[13-19]

1.2.1 Jablonski diagram for Plasmon Fluorophore interaction

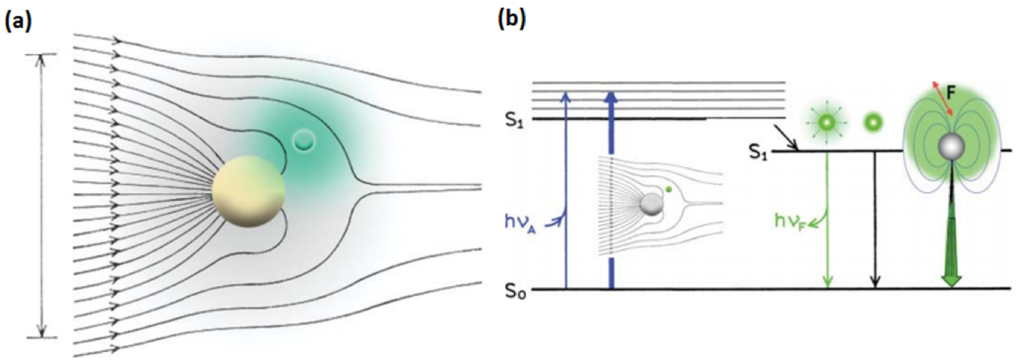

Figure 1.5: (a) Interaction of light with MNP, the arrow represents the direction of the propagating light and green sphere represents presence of fluorophore near MNP (yellow sphere). (b) Alteration in the Jablonski diagram of a plasmon fluorophore composite system. The thick arrow in the diagram represents enhanced rates of excitation and emission in presence of MNP (reproduced with permission).[48]

MNPs exhibit optical cross-section 10^5 times larger than traditional fluorophores.[19, 32] On account of such an enormous optical cross-section, the electric field component of light tends to bend towards the MNP surface as shown in the **Figure 1.5**.[48] Presence of local field results an increase in the excitation process of a fluorophore positioned near MNP surface. Simultaneously another important effect also takes place; excited state fluorophore interacts with nearby MNP to produce induced plasmons. It is shown that fluorophore induced plasmons has the ability to radiate in the far field and create observable radiation.[49]

Emission spectra of PF systems are nearly same as that of the fluorophore; it is often ambiguous as which species is actually emitting. Usually, in PF composite system decrease of lifetime is observed as compared to the isolated fluorophores. Besides plasmonic decays are usually occurs in ultrafast domain (~50 fs),[50] thus it seems that MNPs itself may be the emitting species in PF composite system which result in decrease of overall lifetime. On the other hand, emission profile of PF composite system nearly remains the same as that of fluorophore suggesting that fluorophore is the emitting species. Lakowicz and co-workers elaborately discussed about this confusion and they suggested that PF composite system itself was the emitting species, as emission is convoluted with both the properties of fluorophore and MNPs, and hence they refer this type of system as plasmophore or fluoron.[44, 48, 51]

In a typical fluorescence experiment, modification of quantum yield and lifetime are primarily due to change in the k_{nr} pathways. Both the quantum yield and lifetime of a fluorophore simultaneously either increase or decrease but usually do not change in the opposite directions. However, several unique changes in the emissive properties are possible for plasmophoric system.[19, 44] For example, Viger et al. have shown that when fluorescein isothiocyanate (FITC) interacts with AgNPs, quantum yield and lifetime changes in opposite direction. They concluded that FITC emission underwent 14 times enhancement along with decrease in lifetime form 1.72 ns to 0.025 ns.[52]

The quantum yield (ϕ_0) and lifetime (τ_0) of fluorophore in free space condition is given by

$$\phi_0 = \frac{\tau}{\tau + k_{nr}} \qquad \textbf{(1.2)}$$

$$\tau_0 = \frac{1}{\tau + k_{nr}} \quad \textbf{(1.3)}$$

The quantum yield (ϕ) and lifetime (τ) of fluorophore near MNPs are given by

$$\phi = \frac{\tau + \tau_m}{\tau + \tau_m + k_{nr}} \quad \textbf{(1.4)}$$

$$\tau = \frac{1}{\tau + \tau_m + k_{nr}} \quad \textbf{(1.5)}$$

Where, τ and k_{nr} are the radiative and non-radiative decay rates. Radiative rates in the presence of MNP is denoted by τ_m. When a fluorophore is placed near the metal colloids, τ_m increases which result in the decrease of lifetime of the composite (see the **Equation 1.5)**.

1.2.2 Various conditions for effective plasmon fluorophore interaction

The extent of PF interaction depends on several factors such as nanostructure type,[53-55] aspect ratio, [19, 56] fluorophore,[57] location and orientation of the fluorophore with respect to the metallic surface, [19, 56] overlap of absorption or emission bands of the fluorophore with the SPR band [46, 58] etc. However, distance between the nanostructure surface and fluorophore is found to be the most crucial. Lakowicz showed the distance dependent interaction between MNPs and fluorescence, in a very small distance, (≤ 10 nm) emission quenching is observed whereas emission enhancement is usually noticed at comparatively large distance (≥ 20 nm).[19, 44]

1.2.3 Plasmon fluorophore interaction in various metal nanostructures

Various nanostructures such as thin films,[59-61] single nanorod,[20] nanorod assemblies,[7, 40, 46] spherical nanoparticles[45, 62-63] etc. are used to probe PF interaction. Among various other metal nanostructures, specifically Ag and Au nanoparticles have attained considerable research interest. Several tricky synthetic methods are used to keep fluorophore in close proximity of MNPs. However, three synthetic procedures are routinely followed in most of the studies. First, nanoparticle solution is prepared and fluorophores of different concentrations are gradually added to this solution or conversely fluorophore solution is made where nanoparticles are gradually added to this solution.[64-66]. Secondly, nanoparticle are coated with silica over layer or charged polyelectrolyte layer and fluorophore gets attached to this layer by electrostatic

interactions.[20, 46, 58, 67] Thirdly, nanoparticle are deposited in form of thin film on a silica surface and fluorophore gets attached due to adsorption.[60]

1.2.4. Plasmon fluorophore interaction in silica-capped nanostructures

In majority of the PF interaction studies, substrate preparation is performed by this procedure. At first, nanostructures are synthesized by using a range of stabilizers (usually surfactants) and subsequently surface coating is performed with various charged polyelectrolytes or silica. Silica coating is very popular in field of plasmon induced emission enhancement spectroscopy. Thickness of the silica layer around the MNPs can be controlled and by this the distance between the fluorophore and nanoparticle can be restrained. For example, Cheng et al. synthesized AgNPs using citrate reduction method and attuned the distance between fluorophore FITC and AgNP by tuning SiO_2 layers thickness.[68] They demonstrated that FITC emission can be engineered by controlling distance; at close distance (~1 nm) fluorescence quenching occurred. However with gradual increase in the distance, emission enhancement is noticed as shown in the **Figure 1.6**. The optimum distance was found to be ~21 nm where 4.8 times emission enhancement was recorded.

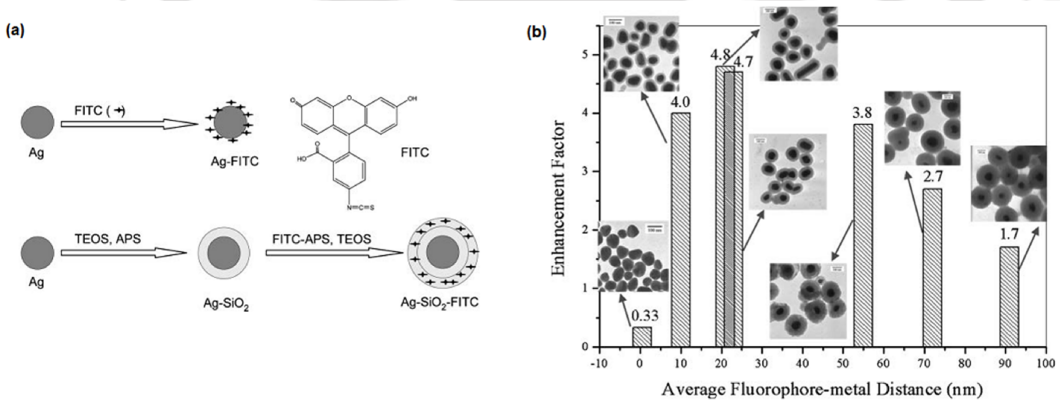

Figure 1.6: (a) Schematic representation of the synthesis of AgNP-FITC composite and AgNP-SiO_2-FITC composite. (b) Distance dependent emission enhancement of FITC by SiO_2 coated AgNPs (reproduced with permission). [68]

1.2.5 Plasmon fluorophore interaction inside organized assemblies

Several tedious synthetic methods are used to keep fluorophore near the nanostructure. However, organized assemblies such as micelles, block co-polymers and

reverse micelles etc. provides natural confined environment to host both fluorophore and nanostructure. In organized assemblies, a close distance between nanostructure and fluorophore is maintained *in situ*. Thus, without using the tricky silica or polyelectrolytes coating, the distance between the fluorophore and nanoparticle can be controlled. Besides, organized assemblies are routinely used in the synthesis of various nanostructures and therefore provide a very efficient system to probe PF interaction.

1.2.5.1 Plasmon fluorophore interaction in citrate capped MNPs

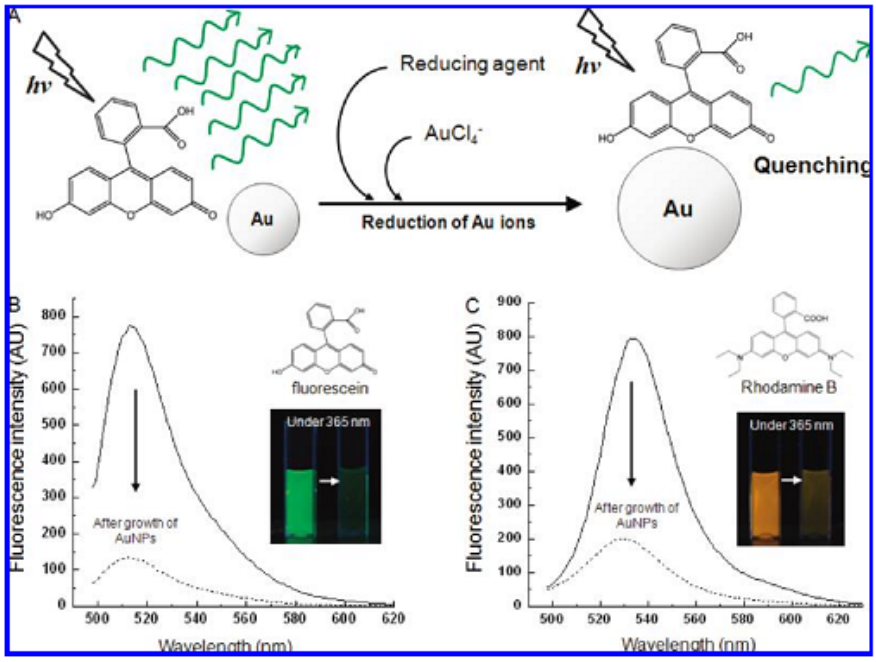

Figure 1.7: Schematic representation emission quenching with increase in the size of AuNPs through reduction of Au ions in presence of reducing agent and $AuCl_4^-$. Emission quenching of fluorescein and rhodamine before and after (dotted line) are shown with increase in the size of AuNPs (reproduced with permission). [64]

A number of reports are available in literature where citrate capped MNPs are used to study PF interaction. For example, Parkin and co-workers used citrate micelles capped AgNPs to probe PF interaction in a range of catatonic and anionic fluorophores.[66] They found that cationic fluorophores interacted strongly with AuNPs whereas anionic fluorophores exhibited only trivial interaction. They explained this behaviour on the basis of preferential binding of fluorophores with the nanoparticles. Similar study Lim et al. showed that AuNPs coupling with fluorophores could be used

in detection of toxic analytes.[64] They first synthesized AuNPs by citrate method and then incorporated fluorophores fluorescein and rhodamine B. Thereafter various analytes (H_2O_2, quinones, acetylthiocholine etc.) were gradually added to this solution. Here the analytes itself acted as reducing agent and hence, gradually increases the size of AuNPs. With increase in the size, interaction between AuNPs and fluorophore surged and hence the quenching (**Figure 1.7)**. Similar study Rabga et al. shown large PF interaction exist between AgNPs (citrated capped) and fluorescein, they reported ~3 times emission enhancement.

1.2.5.2 Plasmon fluorophore interaction in block copolymers

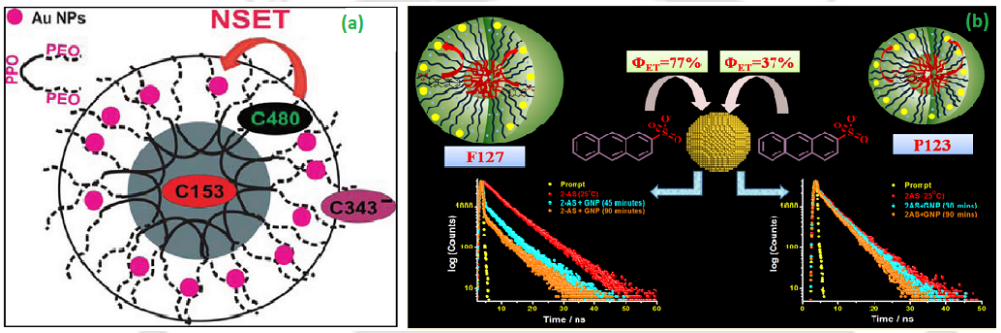

Figure 1.8: Schematic representations of (a) P123 micelles loaded with AuNPs and probe molecules residing at different locations inside the micelles and its implication.[69] (b) location dependent interaction between 2-AS (fluorophore) and AuNPs in micelles of triblock copolymers of F127 and P123 (reproduced with permission).[70]

Recent studies indicates that a number of block copolymers can be used effectively to study PF interaction. The main advantages of block copolymer is that distance between fluorophore and MNPs can be easily controlled without external coating agent. For example, Sarkar and co-worker have performed controlled synthesis AuNPs inside triblock co-polymer P123 micelles and investigated PF interaction using three coumarin probes (C153, C480 and C343). The probes are located in three distinct regions of P123 micelles depending on their hydrophobicity (**Figure 1.8a**).[69] They shown that the probes (C343 and C480) that reside in the hydrophilic corona region of P123 micelles loaded with AuNP (close proximity to the AuNPs) is a perfect place for nanomaterial surface energy transfer (NSET). Whereas probe (C153) that resides inside the hydrophobic core region (far apart from AuNPs) is reluctant to NSET, despite significant spectral overlap between the probe fluorescence and AuNP SPR band. They

also showed that microenvironment of P123 micelles substantially modifies after nanoparticle formation. Bhattacharya and co-workers shown that size variation of the hydrophilic corona region of block copolymers made with P123 and F127 surfactants is the prime factor for NSET between the fluorophore (2-anthracene sulfonate, 2-AS) and AuNPs.[70] By using temperature dependent time resolved measurements they showed that the probe 2-AS resides in a more compact corona region in P123 micelles, whereas in F127 micelles, 2-AS resides in less compact region away from the core of the micelles. They concluded that different location of probe is directly correlated with NSET efficiency (**Figure 1.8b**).[70] Antonisamy et al. further extended the work on F127 micelles and probed NSET between rhodamine B and pluronic F127-Au hybrid, they shown that strong binding ability (~3.5×10^3 $Lmol^{-1}$) of rhodamine B with F127-Au nanohybrid plays significant role in NSET process.[71]

1.2.5.3 Plasmon fluorophore interaction in reverses micelles.

Reverse micelles (RMs) are nanoscopic droplets of spherical self-assembly structures of surfactants dispersed in a non-polar solvent. The nanoscopic droplets are used extensively in synthesis of various nanostructures. Another important aspect is preferential partitioning property of RMs; when a charged fluorophore is added into the reverse micellar solution, the fluorophores are partitioned preferably inside the RMs rather than in continuous non-polar solvent. As both nanostructure and fluorophore tends to resides inside polar droplet RMs which results a close contact among them and thus provides a robust system to explore PF interaction.

Although, RM provides suitable medium to study PF interaction however only a handful of reports are available in literature. Wang et al. probed interaction of fluorescein with TiO_2 NPs inside AOT reverse micellar system.[72] They showed that the presence of TiO_2 nanoparticle results in intense quenching of fluorescein emission. They attributed the quenching on the basis of electron transfer from excited singlet state of fluorescein to the conduction band of TiO_2 nanoparticles. Pramanik et al. used fluorophore safranine T (SAF-T) to probe PF interaction with AgCl nanoparticles synthesized inside AOT RMs.[45] They showed that SAF-T undergoes emission quenching when interacts with AgCl nanoparticles and the quenching process is collisional in nature. Furthermore, they also found that quenching process is correlated with both concentration and size of the AgCl nanoparticles. In an another study binding

capacity of fluorescein was effectively used in synthesis of fluorescent nanoparticles inside Brij35 reverse micellar solution.[73] Jana and co-workers have shown that polyacrylate coated Ag/Au nanostructures with incorporated fluorescein can be used for cell imaging and protein detection.[42, 74]

1.3. MICROEMULSION AND REVERSE MICELLES

The term microemulsion is proposed by Schulman et al. in 1959,[75] microemulsion consists of four (or at least three) components; a surfactant, a co-surfactant (usually long chain aliphatic alcohols), continuous hydrocarbon phase (*oil* phase) and aqueous phase. When oil is dispersed over continuous water phase, oil in water (o/w) microemulsion is formed and conversely when water is dispersed over oil phase water in oil (w/o) microemulsion is formed. Reverse micelles or inverted micelles are subset of water-in-oil (w/o) microemulsions. RMs are w/o microemulsion but not all w/o microemulsion are considered as RMs.[76-77] Levinger and co-workers in their excellent review paper listed various criteria for a w/o microemulsion to be considers as a RMs.[77] Some of these criteria are overall similar viscosity of the dispersion, diffusion of individual polar droplets in the dispersion, three phase system, a polar phase and non-polar phase and interface in between them etc. Most notable parameter is that the size of RMs droplet. The size of the droplet must depend on the amount of polar phase.[77-78]

Based on the nature of polar phase used, RMs are broadly classified into two types- aqueous and non-aqueous. Beside water, various other polar phase such as formamide,[79-80] DMF,[81] glycerol,[82-83] glycols,[82-84] DMSO,[85] acetonitrile,[81, 86-89] methanol[86, 88-94] etc. are tested for RMs forming ability. RMs are used in various applications, such as, template for nanostructures synthesis,[95-99] nanoreactor for organic synthesis,[100-102] altering chemical reaction rates,[103] model for biological systems [78] and so on. Numerous surfactants such as CTAB,[104] Triton X,[105] Brij30 [106] etc. can form RMs, however most of the studies are predominantly based on aerosol OT or AOT (bis (2-ethylhexyl) sulfosuccinate sodium salt). Surfactant AOT provides several advantages over others, for example, RMs without aid of co-surfactant, RMs with water and other polar compound, sequestered large amount of water etc.[107-110]

1.4. AOT REVERSE MICELLE

1.4.1. Structure and properties AOT reverse micelles

Numerous studies (both theoretical and experimental) have shown that AOT reverse micellar structure is comprising at least of four regions- a polar core (water pool), an interfacial layer, surfactants assemblies and the exterior non-polar solvent or bulk continuous phase (**Scheme 1.2**).[81, 90, 107, 111-115] In 1989, Maitra and co-worker by using FTIR measurements reveals presence of various types of water molecule inside water/AOT/*isooctane* RMs.[116]

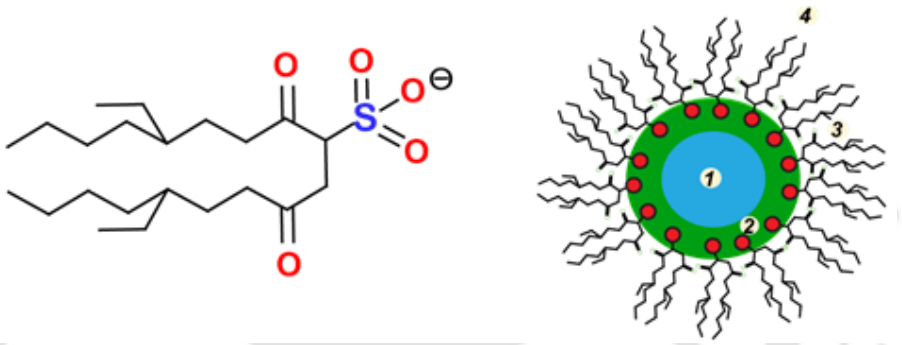

Scheme 1.2: Schematic representation of AOT molecule and AOT reverse micelle. Reverse micelles composed of at least four regions, (1) central water pool, (2) interfacial regions with trapped water molecule, (3) layer of surfactant and (4) bulk continuous phase (reproduced with permission).[117]

The interfacial layer is composed of self-assemblies surfactant molecules attached by non-covalent interaction and hence interfacial layer is microscopically labile. The labile nature of interfacial layer is reported for both aqueous and non-aqueous reverse micelles.[81, 118-119] The confined water of RMs shows very different properties than bulk water. [120] The water pool of AOT RMs displays a unique pH independent behaviour. The pH of the internal water pool is relatively less sensitive with respect to externally added acid or base.[121] A number of studies have shown that water pool of AOT reverse micelles behaves as a buffer for a wide range of bulk pH (2-12).[113, 122] Moreover, it is also possible to control the size of the water pool by changing w_0 values, the ratio of aqueous to surfactant concentration (w_0 = [water]/[surfactant]).[81,

[123] For AOT reverse micelles, hydrodynamic radius of reverse micelle (r_h) is correlated to w_0 ([water]/[AOT) as follows [124]

$$r_h = 0.5\, w_0 + 1.0 \qquad (\mathbf{1.6})$$

As seen from above equation hydrodynamic diameter of RMs can be tuned easily by varying w_0 value of the dispersion.

1.4.2. Transition of reverse micelles to bi-continuous microemulsion

RMs are dynamic assemblies of surfactant molecules that undergo frequent collision with one another due to Brownian motion. The collision leads to the formation of various soft dimer of RMs that subsequently breaks aparts.[77, 125] Dynamic nature of RMs facilitates numerous processes, which take place in different time scales (from picoseconds to milliseconds time domain). Fast processes such as alkyl chain motions in the aggregates, tumbling of the whole droplet, exchange of co-surfactant between aggregates and bulk, exchange of surfactant between aggregates and bulk water etc., take place in a timescale from a few ps to 100 ns.[126] On the other hand, slow processes such as droplet coalescence, aggregates clustering, change of film curvature etc., occur within μs to ms time domain.[126]

Although numerous processes are responsible for regulating the structure of RMs aggregates, however droplet percolation and droplet coalescence/de-coalescence are assumed to be two major processes by which structural transitions may takes place. When an organized RMs aggregates are converted into continuous aggregates, a sharp increase in the conductivity of the solution is noticed. The increase in conductivity implies that charge transport properties of the solution drastically modifies. Such enormous jump in the conductivities are explained by assuming two possibilities. First possibility is formation of at least one continuous path type structure (called as bi-continuous structure) inside microemulsion that facilitate charge transport and the second possibility is attractive interaction of between the droplets inside microemulsion that results in generation of hopping charge across the surfactant layer.[61, 99]

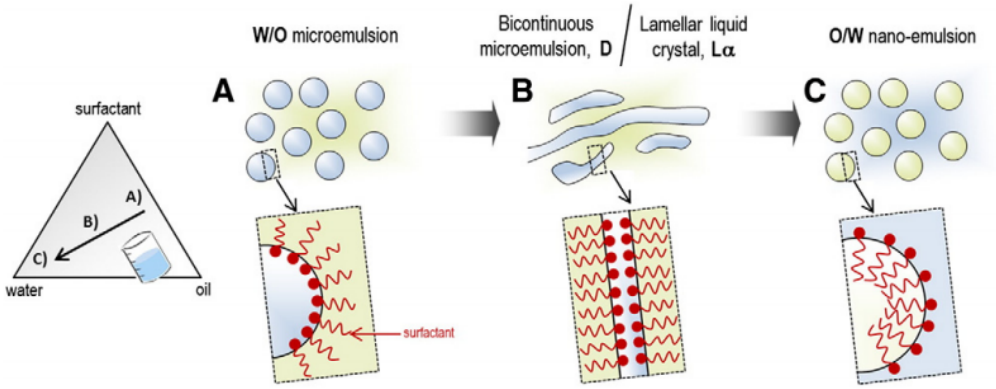

Figure 1.9: Schematic representation modification of microemulsion structures from w/o droplets to o/w droplets with increase in the amount of water content (w_0). Note that there is an intermediate phase where oil and water together known as bi-continuous phase (reproduced with permission). [127]

A number of reports suggest that RMs type structures can be transformed into bi-continuous microemulsion (BMC) type structures by varying a variety of parameters of microemulsion. Some of the parameters are molar ratio of polar component to surfactant (w_s),[128-130] temperature,[131] salinity,[132] external additives,[133] etc. For example, Solans et al. have shown that with gradual increment in the aqueous component promotes structural change in w/o microemulsion as shown in **Figure 1.9**. [127] The spherical w/o droplets are gradually converted into o/w droplets and the intermediate is a continuous phase where both the oil and water are in equilibrium called as bi-continuous phase.

Scriven et al.[134] have introduced the concept of bi-continuous structure (oil or water channels inside microemulsion) in 1976, thereafter numerous studies are performed on these structural assemblies. As the name bi-continuous, it suggests that both the oil and water is in continuous phase. BMC is also called as "sponge" type structure as it exhibits similar properties like the material sponge (by assuming a continuous phase of liquid that remains trapped within the material sponge). Lindaman et al. demonstrated existence of bi-continuous structure inside microemulsion by using NMR.[135] In order to visualize the BMC structure several structural models such as layered structures, disordered open connected structure, voronoi polyhedron, extended structure fluctuation etc. has been proposed.[136]

A number of studies indicated that spherical RM structure are transformed into BMC type structure by varying molar ratio of surfactant and polar component (w_0 or w_s). For example, Liu et al. have investigated the structure of water/AOT/*n*-heptane microemulsion by using conductivity measurements a function of w_0 value.[128] They have shown that conductivity of the solution increase rapidly up to w_0 ~15; thereafter, with further increase in the w_0 value the conductivity of the solution becomes steady. The interaction between the droplet results in the increase of conductivity of the solution (below w_0 ~ 15). Thereafter, with further increase in the w_0 value droplets reaches to a threshold limit and aggregates among themselves. Droplet aggregation results in formations of a continuous path (BMC structure) which results in the steady alteration in the solution conductivity. Yu et al. studied the structural transition behaviour of AOT analogues surfactant bis-(2-ethylhexyl) phosphate (NaDEHP) by using various scattering and spectroscopic methods.[136] They have shown that transition point for water/NaDEHP/*n*-heptane RMs is located at w_0 ~ 4.

However, for non-aqueous microemulsions only handful of studies are available in literature. For example, Moore et al. studied a number of non-aqueous microemulsion by using solvatochromic probe auramin O. They suggested that most of the non-aqueous microemulsion displayed a structural transformation from RM to BMC after a specific w_s.[137] They also shown that the nature of the non-polar continuous phase also plays a prominent role in RM to BMC transition. A number of reports suggested MeOH,[91-93] formamide[80] and ethylene glycol[137] microemulsion exhibits transitional w_s values ~6, 2 and 1.2, respectively.

1.5. AOT REVERSE MICELLES AS NANOREACTORS

A number of physical and chemical methods are used in synthesis of metal nanostructures.[138] However, majority of synthesis methods are unable to fulfil two essential requirements, smaller size and narrow size distribution. RM mediated synthesis is a very specific method that produces precise size and narrow size distribution. In order to illustrate different aspects of the reverse micellar mediated synthesis, a number of review articles are written and thus a brief overview is only presented.[77, 139-142]

The hydrophilic cavity of RMs has been known since 1960s, however novel application of these cavities as a scaffold for nanomaterial synthesis emerges very

lately. Boutonnet et al. in the year 1982 has demonstrated the application of these cavities as a template by synthesising Pt, Pd and Ir nanoparticles. [143] Thereafter varieties of MNPs (Ag,[109, 144-147] Au,[74, 148] Cu, [149-151], Pt,[152-153] Ni[154-155], Pd, [143, 153]Co[155] etc.), bi-metallic NPs (Ag-Au,[156] Ag-Cu,[157] Au-Pt,[158] Pd-Au,[159] Pd-Ir,[159] Pd-Ru,[159] Pd-Pt,[159] Pt-Ru,[159-160] etc.), metal oxide NPs (ZrO_2,[161] TiO_2,[161], $NiMnO_3$,[162] GeO_2,[163] SiO_2,[164] Fe_2O_3[165] etc.) are synthesized. To the best of our knowledge, Barnicke et al. for the first time in the year 1989 reported AgNPs synthesis via reverse micellar route.[76]

AOT reverse micellar method offered several advantages over other methods such as it is very simple, varieties of materials can be produced, reactions can be performed in room temperature, no sophisticated instrumentations is required, high degree of crystallinity of synthesized nanoparticle and so on. Moreover, control over particle size, aniosotropy, shape, uniformity, reproducibility are additional advantages compared to other chemical methods of synthesis and hence termed as tailor made synthetic method of nanoparticle. The most important aspect of RMs mediated route is that size of the MNPs can be easily tuned by changing w_0 value of the reverse micellar solution (see **Equation 1.6)**. Moreover, a significant correlation exist in between size and shape of initial reverse micellar droplets with the synthesized nanostructures. Ganguli and co-workers have studied shape transformation of reverse micellar droplets and its templating effect on nanoparticle growth.[130, 166] They used a range of characterization techniques to monitor the nanostructure growth at (near) the single-droplet level and in an ensemble. They have shown that droplet fusion rate plays a distinctive role and directly control the nanorod growth in microemulsion solution.

1.5.1 General synthetic procedure

The synthetic procedure for nanoparticle formation inside reverse micelles follows two distinct routes, single and double microemulsion as shown in **Scheme 1.3**. [133-136] Single microemsulion method is further divided into energy triggering and single microemulsion plus reactant methods. In energy triggering, external pulse or stimuli is used to initiate nucleation whereas single microemulsion plus reactant method nucleation is initiated by adding reducing agent. Single microemulsion method is diffusion controlled process as reactants has to diffuse through reverse micellar interface for recation.[138] In the double microemulsion method, one microemulsion containing soluble metal precursor is mixed with another microemulsion containing

reducing agents. Upon mixing, both metal precursor and reducing agent reacts and tigers the nucleation followed by growth. During the growth process, surfactant layer is attached to MNPs surface.[133-136] This attachment provides stabilization and hinders further growth. Moreover, steric barrier of surfactant over-layer provides additional stabilization and thereby prevents nanoparticle coagulation.[167]

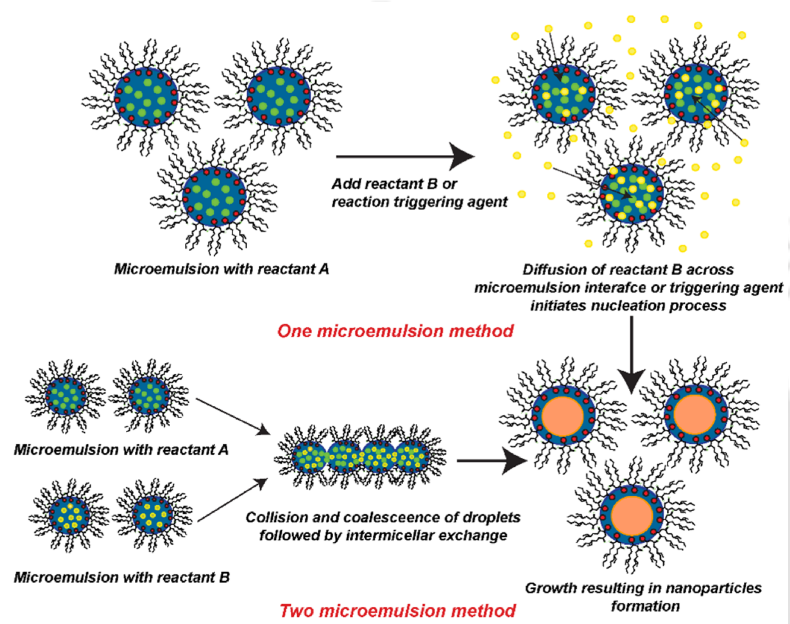

Scheme 1.3: Schematic representations of various steps involve in the synthesis of nanoparticles via (a) one microemuslion method and (b) two microemuslion method.

1.5.2 Optical properties of AgNPs synthesized by AOT microemulsion route

As discussed in the **Section 1.2.5.3**, reverse micellar system provides several advantages for PF interaction. However, the main hurdle associated with AOT reverse micellar based approach is the poor optical quality of SPR band of the MNPs, especially for AgNPs. By "optical quality", we imply the strength and sharpness of the SPR band. A large bandwidth may limit its spectroscopic application, especially, when another absorbing species is present in the dispersion.[147, 168] The optical qualities of AgNPs synthesized via various AOT microemulsions routes is summarized in **Table A.1.1** in *Appendix*. Here I also try to tabulate the effects of various parameters and reaction conditions in generation of AgNPs SPR. As seen from **Table A.1.1,** most of the reported methods demonstrated weak and broad SPR band having a maximum ~400

nm. Moreover, **Table A.1.1** is also suggested that FWHM (full width at half maxima) of SPR depends on several factors such as concentration of metal precursors, [169-170] concentration of reducing agent, [109, 168, 171-173] reaction time, [109, 173-174] type of reducing agent used, [109, 168] w_0 value,[169-170, 175] type of continuous phase,[109, 172] types of RMs (aqueous or non-aqueous), [174, 176]AOT concentration,[177] pressure. [171]

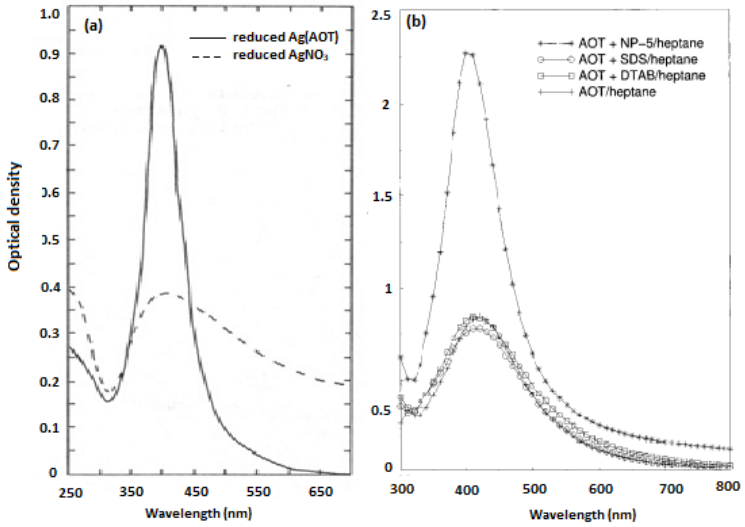

Figure 1.10: Comparison of optical quality of the AgNPs SPR band at $w_0 = 10$ by the work of (a) Petit et al. [109] with (b) Bagwe et al.[172] work. Petit et al. used $NaBH_4$ reduction in NaAOT by using(– – –) silver nitrate and (–) silver sulfosuccinate as silver precursor, $[AOT]_{total} = 0.1$ M; $[AgNO_3] = [AgAOT] = 10^{-3}$ M, $[NaBH_4] = 10^{-4}$ M. Bagwe et al. used $NaBH_4$ reduction in NaAOT by using silver nitrate as a precurssor, $[AgNO_3] = 1.8\times10^{-3}$ M, $[NaBH_4] = 9\times10^{-4}$ M in presence of different surfactant additives (reproduced with permission).

From **Table A.1.1**, it is apparent that the optical quality of AgNPs reported by Petit et al. is the best among the AOT-based methods till date, as shown in the **Figure 1.10**.[109] However, they used functionalized surfactant, Ag-AOT instead of commonly available Na-AOT. They used a mixture of 30% Ag-AOT and 70% Na-AOT for RM formation. Ag-AOT also served as source of Ag^+ precursor apart from its role in formation of reverse micellar interface. They suggested that solubility of the metal precursor plays a decisive role in overall optical quality. As $AgNO_3$ is poorly soluble in the reverse micellar media than Ag-AOT and therefore the optical quality is inferior

when $AgNO_3$ is used as a precursor. On other hand, Bagwe et al. have shown that it is possible to synthesis high optical quality AgNPs by using $AgNO_3$ (without functionalized Ag-AOT) as a precursor.[172] They achieved high optical quality simply by adding a co-surfactant (NP-5 surfactant) to water/AOT/*n*-heptane RMs. They suggested that the NP-5 molecule which acts as a co-surfactant brings the fluidity of reverse micellar interface and results in increase of collusions between the RMs droplets. Increase in the collusions results in the formation monodisperse AgNPs and hence sharper SPR.[172] Another interesting aspect of these two studies is that both of them used same reducing agent ($NaBH_4$) and same w_0 value (w_0 = 10) for AgNPs synthesis.

1.5.3 Correlation of SPR band with particle size in AOT microemulsion system

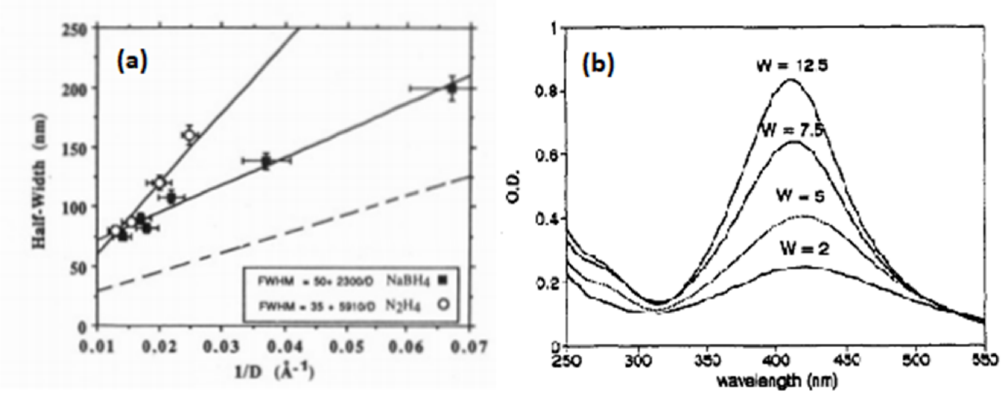

Figure 1.11: Spectra showing (a) a relation between of SPR bandwidth with particle diameters synthesized by AOT microemuslion route using $NaBH_4$ and N_2H_4 (hollow circle) as reducing agents. The dash line represents Mie simulation curve. (b) Variation of SPR peak with w_0 values of AOT microemulsion. [109] Note that a blue shift in SPR maxima is noticed with increase in w_0 values (reproduced with permission).

There is a nice correlation exists between the size of the nanoparticle and corresponding SPR bandwidth. Moreover, from SPR band and it is possible to gets a rough estimate of nanoparticle size. For example, Petit et al. have estimated the size of AgNPs from the width of the AgNPs SPR spectrum.[109] In fact, they showed that a direct relation is exists between the full width at half maximum (FWHM) with AgNP diameters. In order to establish this, they first simulated AgNPs SPR band with the help of Mie theory (see **Section 1.1.3)** and then correlate it with the nanoparticle size (from

TEM measurements). The AgNPs synthesized by various reducing agents ($NaBH_4$ or N_2H_4) are taken in the calculation (**Figure 1.11a)**. The AgNPs synthesized by N_2H_4 reduction shows crystal defects, which in turn result in the significant interaction with the surrounding medium and results in inferior optical quality compared to $NaBH_4$ reduction.

Usually, it is assumed that progressive increase in size of nanoparticles should lead to a continuous red shift in AgNPs SPR (**Section 1.1.4** and **Figure 1.2)**. However, exceptional behaviours of SPR (blue shifting of SPR peak with increase in size) is well reported in literature. For example, Petit et al. have shown that with increasing size of AgNPs, instead of expected red shift a clear blue shift in SPR is noticed (**Figure 1.11b**).[109] They explain this unusual behaviour based on interaction surfactant with nanoparticles; strong interaction leads to blue shift whereas weaker interaction leads to red shift. On the other hand, Henglein et al. have shown that change of electron density around AgNPs can also influence the SPR maximum.[178] When excess electron density accumulation occurs around nanoparticle, Fermi level shifts to more negative side which results in the blue shifts. Below 20 nm size, extinction spectra of AgNPs depends on total nanoparticles concentrations but not entirely on the particles size.[179]

1.6. PROBING OF AOT REVERSE MICELLAR INTERFACIAL LAYER BEFORE AND AFTER NANOPARTICLE FORMATION

As discussed in **Section 1.5,** due to elegant structural organization RMs act as nanoreactor for synthesis of varieties of MNPs. However, reverse micellar assemblies are hold merely by non-covalent interactions and hence termed as “soft template”. Therefore, formation of nanoparticles inside the soft template may induce significant changes in their structural organizations. However, the details of the structural change of interfacial layer associated with the nanoparticle formation are not clearly understood until date. Techniques such as DLS and TEM usually estimate the size and the morphology of the nanoparticles but extracting information regarding the interfacial layer is not straightforward. In fact, the physical properties inside a surfactant assembly itself are much different from bulk properties. Do the physical properties of the surfactant assemblies alter upon nanoparticle formation? Such information is valuable for understanding the growth process, extraction methodology and more importantly, for synthetic developments and technological applications of the nanoparticles.

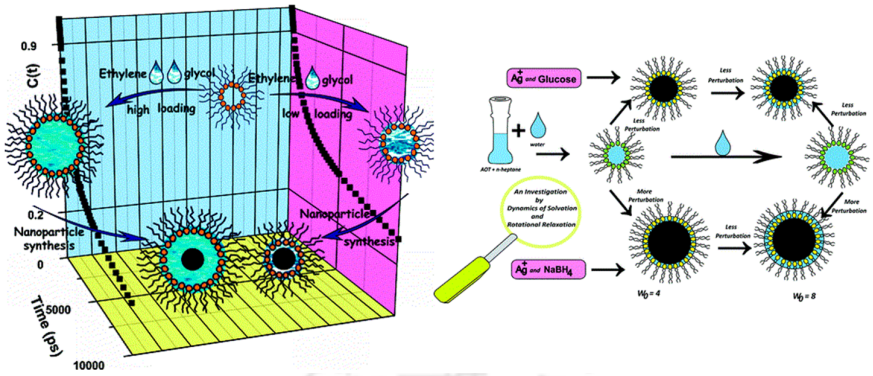

Figure 1.12: Schematic representation of probing of AOT reverse micellar interface before and after AgNPs formation inside (a) non-aqueous ethylene glycol and (b) aqueous reverse micelles (reproduced with permission).[143, 163]

Very recently, Sarkar and co-workers have initiated some interesting works regarding this topic (**Figure 1.13**).[147, 168] They have used solvatochromic fluorophores, coumarin 153 (C153) and coumarin 480 (C480) in probing reverse micellar interfacial layer before and after nanoparticle formation. One of their first study, AgNPs were synthesized using glucose reduction method inside water/AOT/*n*-hepatne RMs at w_0 = 4 and probed the system with fluorophore C153.[147] They found that both the average fluorescence anisotropy ($\langle\tau_r\rangle$) and average solvation dynamics ($\langle\tau\rangle$) become slower after nanoparticle formation. They suggested that probe C153 experiences more restricted environment inside the AgNP-perturbed RMs compared to the unperturbed RMs. In a subsequent study, AgNPs were synthesized inside non-aqueous ethylene glycol/AOT/isooctane RMs at w_0 = 1 and 2 and used C480 as a solvatochromic fluorophore.[176] Unlike their previous study, $\langle\tau_r\rangle$ and $\langle\tau\rangle$ follows anomalous trend, $\langle\tau_r\rangle$ becomes faster and $\langle\tau\rangle$ becomes slower when the system changes from RMs to AgNP-RMs. They attributed this unusual trend to differential perturbation of ethylene glycol RMs compared to aqueous RMs. In another work water/AOT/n-heptane RMs synthesized AgNPs inside at two different w_0 values (4 and 8) using mild (glucose) and strong ($NaBH_4$) reducing agents and probed the system with C480.[168] They found that reverse micellar aggregated structures were present after the nanoparticles formation in a perturbed state. Nanoparticles inside the reverse micellar core were responsible for this perturbation. Larger size nanoparticles produce by stronger reducing agent ($NaBH_4$) triggering larger perturbation than the smaller size produce by weaker reducing agent (glucose) at same w_0 value.

1.7. OBJECTIVES OF THE THESIS

Synthesis of superior optical quality AgNPs is desirable for both fundamental and application point of views. Reverse micellar type microemulsions are advantageous in synthesis of MNPs and also provide suitable environment for effective plasmon-fluorophore interaction. However, the main drawback of reverse micellar approach was the poor optical quality of the MNPs, especially for AgNPs. In this thesis, AOT microemulsion based synthesis routes has been explored for generation of AgNPs with high optical qualities. Several reducing agents were tested and it was found that mild reducing agent ascorbic acid has the ability to produce high optical quality AgNPs in room temperature. Effects of reducing agents, water to surfactant ratio (w_0), concentration of reducing agents etc. were explored thoroughly. The applications of superior optical quality AgNPs were tested in probing modifications in the reverse micellar interface after nanoparticle formation and in designing a facile system to study plasmon-fluorophore interaction. Thereafter, usefulness of this method was extended for generation of AgNPs inside non-aqueous medium. It is observed that acetonitrile microemulsion provides suitable template. However, the structure of template itself debated in literature. Hence, first the structure of template was studied using a fluorophore and then AgNPs are synthesized within it. The non-aqueous AgNPs exhibits several interesting properties that were thoroughly investigated in the thesis.

Chapter-2

Materials, Methods and Instrumentation

CHAPTER 2: MATERIALS, METHODS AND INSTRUMENTATION

This *Chapter* presents an outline of the material used and the procedures that are followed in sample preparation and specification of various instruments such as UV-visible spectrophotometer, steady-state spectrofluorometer, time correlated single photon counting, dynamic light scattering, transmission electron microscope etc. are used in the experiment. Tricky synthetic protocol will be presented in the respective *Chapters*.

2.1. MATERIAL

2.1.1. Fluorescence probes

Throughout the work a number of fluorescent probes such as coumarin 343 (C343), coumarin 480 (C480), fluorescein (FL), safranin O (SAF) and 4-aminophthalimide (4-AP) were used. All probes were purchased from Sigma-Aldrich Chemicals and used as received.

2.1.2. Surfactant and chemicals

Bis(2-ethylhexyl) sulfosuccinate sodium salt (Aerosol OT or AOT) was purchased from Sigma-Aldrich Chemicals. AOT was dried overnight at 80 °C in an oven before performing each experiment to remove any adsorbed moisture. Sodium hydroxide and hydrochloric acid was purchased form Merck chemicals and used in pH adjustment.

2.1.3. Solvents

Throughout the work, *n*-heptane was used as a bulk solvent in RMs formation and purchased from Merck (UV spectroscopic grade). Aqueous RMs were generated using ultra-pure millipore water with resistivity (~18.2 MΩ cm). Non-aqueous acetonitrile RMs were prepared by using specially dried acetonitrile obtained from Merck chemicals.

2.1.4. Metal precursor and reducing agents

High quality (99.9999%) silver nitrate ($AgNO_3$) were purchased from Sigma-Aldrich. Throughout the studies, $AgNO_3$ was used as a metal precursor. Reducing

agents such as L-ascorbic acid (AA), sodium borohydride ($NaBH_4$), hydrazine hydrate ($N_2H_4.H_2O$, 99-100%) were obtained from Sigma-Aldrich.

2.2. METHODS

2.2.1. Preparation of aqueous reverse micelles

AOT stock solution with concentration ~90 mM was prepared by weighing the solid AOT and dissolving in the bulk solvent (*n*-heptane). In order to dissolve AOT completely and to get a clear solution, the AOT/heptane mixture was vortexed for 10 minutes followed by shaking. Reverse micellar solution in absence of any polar component is termed as dry RMs (or $w_0 = 0$).[112, 180] RMs with various w_0 was prepared by injecting requisite amount of water in the AOT/heptane solution using a calibrated micro syringe. After addition of water, the RM solution was vortexed for 5 minutes. Amount aqueous part present in the solution was expressed as the molar ratio of aqueous to AOT concentration and designated as w_0; where w_0 = [water]/[AOT].

2.2.2. Preparation of acetonitrile reverses micelles

Above procedure was repeated in order to generate acetonitrile/AOT/*n*-heptane RMs. Except in place of water, acetonitrile was added to the AOT/heptane mixture. Amount acetonitrile present in the solution expressed as the molar ratio acetonitrile to AOT concentration and designated as w_s, where w_s = [acetonitrile]/[AOT].

2.2.3. Preparation of reverse micellar solution containing various fluorophores

For *Chapter 4,* reverse micellar solutions at w_0 = 2, 6, 10 were prepared by adding requisite amount of water into 0.09 M AOT/*n*-heptane mixture. To incorporate the probe into the reverse micellar solution, a stock solution of either C343 or C480 in ethanol was prepared and spread in a 5 ml glass vial and is allowed to evaporate completely. Then, the residual C343 or C480 was re-dispersed in 3 ml of the pure RM solution. In all experiments, the concentration of the C343 was kept at ~10 μM. For *Chapter 5*, RM solution was prepared at w_0 = 6. To incorporate the charged fluorophores, fluorescein (FL) and safranin O (SAF) into RM system similar process was followed. The concentration of fluorophores was kept at ~1 μM. For *Chapter 6*, acetonitrile RM solutions were prepared by adding requisite amount of acetonitrile into 0.09 M AOT/*n*-heptane mixture. To incorporate probe 4-AP above process repeated, concentration of the 4-AP was kept at ~5 μM. AgNP containing reverse micellar solution having probe were prepared just by replacing RM with AgNP RM.

2.2.4. Synthesis of silver nanoparticles in AOT reverses micelles

For synthesis AgNPs, a stock solution of silver precursor and reducing agents were prepared. Both the precursor and reducing agent concentrations were adjusted in such a way that they become fully soluble in their respective polar content as well as after reverse micellar incorporation. The final concentrations were calculated by considering the total volume of the solution. Precursor and reducing agents were mixed together in different proportion for synthesis. The synthesis protocol is specific and diverse for different reverse micellar solution and will be discussed in respective position of studies.

2.3. INSTRUMENTATION

2.3.1. Steady state absorption spectroscopy

Steady state absorption spectroscopy is one of the most widely used spectroscopic measurements technique which gives valuable information about transition wavelength and consequent molar extinction coefficient of a chromophore.[19, 181] The absorption spectroscopy is represented in a simplified manner as

$$A = \varepsilon C l = log \frac{I_0}{I} \qquad (2.1)$$

Where A is absorbance (or optical density), ε absorptivity or molar extinction coefficient, C concentration of the chromophore and l path length of the medium, I_0 and I are intensity of incident and transmitted radiation, respectively.

All the experiments were performed with Perkin-Elmer Lamda-750 spectrophotometers comprising of double holographic grating monochromator, a deuterium tungsten and halogen light source and a very sensitivity R928 PMT detector.

2.3.2. Steady state emission spectroscopy

Emission spectroscopy is broadly divided into two sections, steady state emission spectroscopy and time resolved emission spectroscopy. In steady state measurements, samples is illuminated with a continuous light source (xenon arc lamp) and respective emission profile is recorded with diffraction grating monochromator.[19, 182] Steady state spectrum represents an ensemble average after completion of most of the excited state dynamics.[19, 181] Whereas in time resolved measurement, a pulsed light

source (laser diodes) is used to monitor the decay profile of an emission with very fast detecting systems. In all the experiments, steady state emission and excitation spectra were recorded by using Jobin-Yvon Fluoromax4 spectrofluorometer comprising of 150 W xenon arc lamp. Both emission and excitation spectra's were recorded with quartz cuvette having 10 mm path length. In order to minimize the inner filter effect in *Chapter 4*, both emission and excitation spectra's were also taken in a glass capillary (Hirschmann® melting point determination tubes, Aldrich) of 0.8 mm internal diameter. Emission spectra were recorded at right angle geometry i.e. an angle of 90^0 with respect to the path length of incident light while emitted photons are detected by R928P PMT.

2.3.3. Time resolved spectroscopy

The time resolved spectroscopy is used to resolve various component present the entire steady state emission spectrum. The minute details of any excited state processes can be identified by measuring the intensity decay profile by using time correlated single photon counting (TCSPC) technique.[19, 77] TCSPC is a standardised system for fluorescence lifetime measurements having resolution from picoseconds to millisecond domain. Depending on light source and sensors present in the instrument, lifetime of various probe can be easily determined. Throughout the work, TCSPC measurements were performed on two different TCSPC instruments; LifeSpec II from Edinburgh Instruments and Ultrafast-01-DD from Horiba instruments. Several pulsed laser light source such as LDH-P-C-405 (picoQuant), DeltaDiode-375L, 405L and 510L etc. were used in the studies. The full width at half maximum (FWHM) were adjusted ~100 ps for the both the instruments.

2.3.3.1. Deconvolution of decays

After an excitation laser pulse an emission pulse is generated, however majority of fluorophores exhibits comparable lifetime with laser source. Consequently, the generated pulse become convoluted, in spite of only emission pulse, the decay contain mixture of both excitation and emission pulses. Hence, deconvolution procedure is performed in order to extract the lifetime from convoluted decay and integral of convolution represented as

$$N(t) = \int_0^{t'} L(t)I(t' - t)dt \qquad (2.2)$$

Where $L(t)$ instrument response time (prompt), $I(t)$ convoluted intensity decay, $N(t)$ the observed decay, t is denoted as changeable time delay (number of channels) and channel width denoted as dt.

Various deconvolution procedures[183-188] are followed to extract $I(t)$ from $L(t)$, however least square method still retains the popularity.[184] In least square method, first excitation pulse (lamp profile) is taken followed by mixing with generated decay profile to form a new re-convoluted data set. Now with experimentally observed data set this new data is compared and the difference in between them is summarized and thereafter χ^2 is generated. The whole process is repeated numerous times until infinitesimal change in χ^2 is noticed in between successive iteration. The goodness of fit is denoted by χ^2 value, usually $\chi^2 < 2$ denotes a good fit. Decay deconvolutions were performed with a software programme that is provided with the instrument. FAST and DAS6 programmes were used for deconvolution analysis.

2.3.4. Fluorescence anisotropy

Fluorescence emission with dissimilar intensity depending on axes of polarisation is defined as fluorescence polarisation or fluorescence anisotropy.[19] Anisotropy measurements are extensively used in biomedical research, protein dynamics, diagnostic purposes, probing micro heterogeneous media such as micelles and RMs etc.[18-19, 57, 97, 182] The fluorescence anisotropy are broadly categorized into two section; steady state anisotropy and time resolved anisotropy.

Under continuous light irradiation, steady state anisotropy ($\hat{r}$) is denoted as[19, 182, 189]

$$\hat{r} = \frac{I_{\parallel} - I_{\perp}}{I_{\parallel} + 2I_{\perp}} \qquad (2.3)$$

Where $I_{\parallel}$ and $I_{\perp}$ is intensity of polarized emission in parallel and perpendicular direction with respect to the electric field vector of a polarized light. $I_{\parallel}$ and $I_{\perp}$ is alternatively represented as I_{VV} and I_{VH} , where V and H represented as vertical and horizontal orientation of polariser and total fluorescence intensity is represented as $I_{\parallel} + 2I_{\perp}$.

Steady state fluorescence anisotropy were recorded with Horiba Fluorolog and Jobin-Yvon Fluoromax4 spectrofluorometer.

The instantaneous or time resolved anisotropy denoted as

$$r(t) = \frac{i_{\parallel}(t) - i_{\perp}(t)}{i_{\parallel}(t) + 2i_{\perp}(t)} \qquad (2.4)$$

Where $i_{\parallel}(t) + 2i(t)$ is total time resolved emission intensity. Based on the instrument parameters and sensitivity of PMT, the detector channels are corrected by a correction factor called G factor and denoted as

$$r(t) = \frac{i_{\parallel}(t) - Gi_{\perp}(t)}{i_{\parallel}(t) + G2i_{\perp}(t)} \qquad (2.5)$$

G factor is the ratio of detector sensitivity in horizontal and vertical direction.[190]

For an isotropic single emitting species, anisotropy r(t) follows single exponential kinetics with rotational correlation time (τ_r) as

$$r(t) = r_0 \exp(-t/\tau_r) \qquad (2.6)$$

For a mixture of emitting species, r(t) becomes multi exponential as

$$r(t) = r_0 \sum B_i \exp(-t/\tau_{r_i}) \qquad (2.7)$$

Where B_i and r_i is associated with total depolarisation and corresponding rotational correlation time, respectively.

2.3.4.1. Time resolved fluorescence anisotropy measurements and analysis

Anisotropy decays were taken LifeSpec II and Ultrafast-01-DD TCSPC instruments with various laser light sources. To measure r(t), the analyser were turned at regular intervals and parallel ($I_{\parallel}$) and perpendicular ($I_{\perp}$) components were collected separately and thereafter by using **Equation 2.5** anisotropic curve was constructed. Each time prior to the experiment G factor were calculated by dissolving the respective fluorophores in respective bulk solvents. The anisotropy decays were analysed with FAST and DAS6 programme.

2.3.5. Construction of time resolved emission spectra and solvation dynamics

Fluorescence transients of different fluorophores were recorded at 10 nm wavelength intervals across the entire steady state spectrum thorough our TCSPC setups. Decays were measured at magic angle (55°) with respect to the analyser. The spectral reconstruction protocol of Maroncelli and Fleming[191] were followed in construction of time resolved emission spectra (TRES) and spectral modification on TRES was performed to generate time resolved area normalized spectra (TRANES). Solvent correlation function C(t) was generated from TRES profile.

The solvent correlation function, C(t) were calculated by using equation

$$C(t) = \frac{\nu(t)-\nu(\infty)}{\nu(0)-\nu(\infty)} \quad (2.8)$$

Where ν(0), ν(t) and ν(∞) are the emission frequencies at time zero, t and infinity, respectively.

The generated C(t) data were fitted with exponential function

$$C(t) = \sum_i \alpha_i \exp(-t/\tau_{s_i}) \quad (2.9)$$

The average solvation time was calculated as

$$< \tau_s >= \sum_i \alpha_i \tau_i \quad (2.10)$$

Data fittings were performed with Igor pro and origin programme.

2.3.6. Quantum yield estimation

Followed by absorption of light, the excited molecules disperse the absorbed energies through numerous processes such as vibrational relaxation, solvent relaxation, internal conversion, intersystem crossing, emission or nonradiative de-excitation etc.[19, 77, 182] Quantum efficiency or quantum yield is the efficiencies of above processes. Quantum yield (ϕ_f) is defined as the number of photons emitted to the number of photons absorbed

$$\phi_f = \frac{\text{Number of photons emitted}}{\text{Number of photon absorbed}} \quad (2.11)$$

Quantum yields are calculated by taking a suitable reference with help of following equation as

$$Q = Q_R \frac{I}{I_R} \frac{A_R}{A} \frac{n^2}{n_R^2} \quad (2.12)$$

Where, Q is the quantum yield, I denotes to the integrated fluorescence intensity, A stands for absorbance and n is the refractive index of the solvent. The un-subscripted letters and the subscript "R" represent the sample and reference, respectively.

For *Chapter 5,* fluorescein in 0.1M NaOH (Q = 0.95) and safranin O in acetonitrile (Q = 0.24) was taken as reference.[192-193] For *Chapter 6,* 4-AP in acetonitrile (Q = 0.63) was taken as a reference.[112]

2.3.7. Dynamic light scattering

DLS measurements were performed in Malvern Nano ZS 90 instrument using 50 mW DPSS laser. The He-Ne Laser (λ = 632.8 nm) was used as excitation source. The scattering was collected at a fixed angle of 90°. The solutions were filtered with PTFE syringe filters having 0.2 μm pore size prior to DLS measurements. Around 1 ml of sample was taken on a thoroughly rinsed dust free quartz cuvette having 10 mm path length. Cumulant (or Z-average) size and peak size (or distribution size) were calculated by taking an average of 50 scans of the respective microemulsion sample. In DLS, diffusion coefficients of particles are first measured with autocorrelation function of the scattered light followed by estimation of hydrodynamic diameter through Stokes-Einstein equation. Usually two different algorithms were used in determination of average size and peak size. ISO 22412:2008 method was used in determination of Z-average by force fitting initial portion of the correlation function with single exponential decay (usually initial 10% of the intercept). On other hand distribution analysis was done by regulation techniques such as NNLS or CONTIN by fitting correlation function to longer time i.e. a large number of data has to be fit.

2.3.8. Transmission electron microscopy

TEM measurements were carried out in a JEOL JEM 2100 electron microscope operating at a maximum accelerating voltage of 200 kV. TEM samples were prepared by spreading a drop of the AgNP dispersions into a copper grid coated with carbon and allowed it dry. TEM images were analyzed by Image-J software with PSAr12 plugin; the mean and standard deviations were calculated by taking 500-600 particles.

Chapter-3

A Facile Synthesis of High Optical Quality Silver Nanoparticles by Ascorbic Acid Reduction inside AOT Reverse Micelles[#]

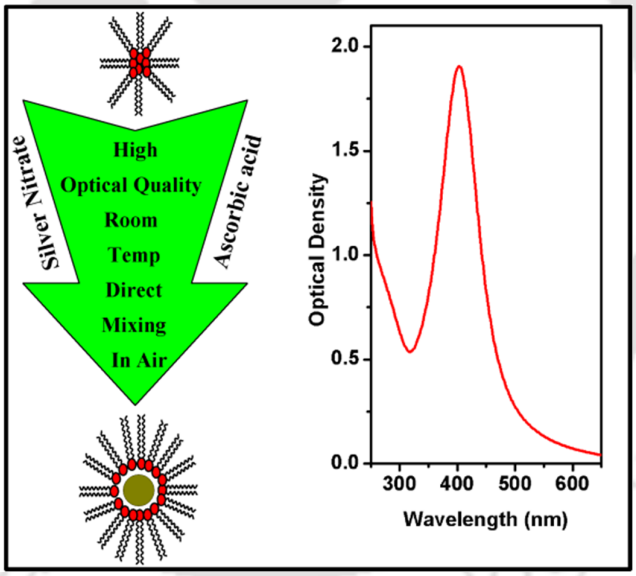

[#]This work has been published in *J. Colloid. Int. Sci.* **2014**, *413*, 37-42.

CHAPTER 3: A FACILE SYNTHESIS OF HIGH OPTICAL QUALITY SILVER NANOPARTICLES BY ASCORBIC ACID REDUCTION INSIDE AOT REVERSE MICELLES

3.1. INTRODUCTION

AOT microemulsion is used as a lucrative nano-reactor for synthesis various MNPs (**Section 1.5**). Although, extensive studies are performed about AgNPs synthesis inside AOT-microemulsion cavity, however the problem associated with poor optical quality is rarely addressed. In most of the recent studies, a weak and broad SPR bands is observed having a maximum ~400 nm (see **Table A.1.1** in *Appendix*).[144, 147, 168, 194-195] This *Chapter* is focused on developing a new facile synthesis route to produce high optical quality AgNPs.

Ascorbic acid (AA) is used as a reducing agent to reduce silver nitrate inside water/AOT/*n*-heptane RMs at room temperature. AA is a naturally occurring biological compound having mild reducing character and good solubility in water, but normally considered as too weak to reduce silver (or gold) salt at room temperature.[148, 196-197] However, AA becomes effective at elevated temperature,[198] or in the presence of a catalyst. Yang et al. demonstrated that silver nanoclusters (AgNCs) can catalyse the reduction of Ag^+ by AA at room temperature.[197] AA is used as a secondary reducing agent for gold or silver nanorod synthesis by "seed-mediated-growth" method, where the "seed" (preformed AgNPs produced by another reducing agent) catalyses the reduction of metal ions in the growth stage. [196, 199] There are very few reports on direct reduction of metal ions by AA,[148, 200-201] and to the best of our knowledge, this is the first synthesis of AgNPs using AA as a reducing agent in RMs.

Another important consideration for the microemulsion route is that the size and colloidal stability of RMs are often sensitive to external additives.[202] Sarkar and co-workers reported that precursor loading increases the size of RMs even before the formation of any nanoparticles.[147] Hence, methods that are effective at very low concentrations of precursors are desirable to ensure colloidal stability of AgNPs containing microemulsions. Here very low concentrations of both the silver salt (0.3 mM) and the reducing agent (≤0.1 mM) is used to circumvent this problem. Despite using very low concentration of the precursors still intense SPR is observed which makes this study unique and rather innovative. As discussed in the **Section 1.5.2**, the

optical quality of AgNPs reported by Pileni and co-workers may be the best among the AOT-based microemulsion methods till date however we will show that our method produces similar SPR band despite using ordinary AOT (sodium salt).[109]

3.2. SYNTHESIS OF SILVER NANOPARTICLES

A 90 mM AOT/n-heptane solution is prepared by dissolving required amount of AOT in 5 ml *n*-heptane. The aqueous solution necessary to sustain the requisite w_0 is added in two equal parts; one containing $AgNO_3$ solution and another containing AA solution. The silver nitrate and AA solutions are injected successively into the AOT/heptane mixture followed by shaking in a vortex mixer to form a homogeneous solution. The overall silver nitrate concentration is fixed at 0.3 mM, while the AA concentrations are varied at 0, 0.01, 0.05, 0.10, 0.20 mM. Upon addition of AA solution, bright yellow to reddish colour gradually develops thereby indicating the formation of AgNPs.

3.3. RESULTS AND DISCUSSION

3.3.1. Effect of ascorbic acid

Figure 3.1 represents the absorption spectra of the AgNPs formed at various concentrations of AA at w_0 = 2,6 and 10. It is evident from the **Figure 3.1** that with increase in the AA concentration, the SPR band becomes more intense and the colour of the solution gradually darkens light yellow to dark brown. Note that this synthetic protocol is effective even at the lowest concentration (0.01 mM) of AA, as seen by a prominent SPR band and the visible yellow coloration of the solution (insets of **Figure 3.1**). As seen from **Figure 3.1**, the optical quality of the sample is comparatively best for 0.10 mM AA. At this concentration, the SPR band is intense and sharp with negligible absorption at higher wavelength region. With further increment in the AA concentration, the optical density of SPR band increases, however the spectrum displays an additional tail up to 800 nm may be due to agglomeration of AgNPs into larger sized particles.

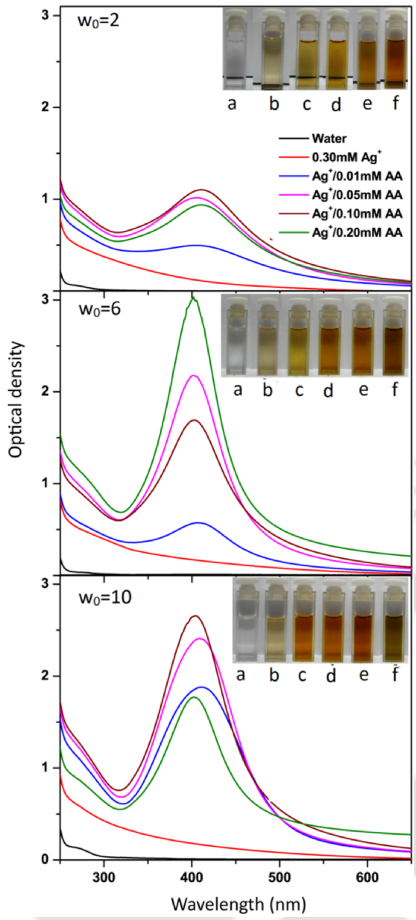

Figure 3.1: The UV-Vis spectra of water/AOT/n-heptane reverse micellar systems at w_0 = 2,6 and 10 containing different additives- (a) water, (b) 0.3 mM $AgNO_3$, (c) 0.3 mM $AgNO_3$ and 0.01 mM AA, (d) 0.3 mM $AgNO_3$ and 0.05 mM AA, (e) 0.3 mM $AgNO_3$ and 0.10 mM AA, and (f) 0.3 mM $AgNO_3$ and 0.20 mM AA. All concentrations represent the overall concentration. The inset represents snapshots of these solutions when viewed under ordinary light.

The reduction of silver ion by AA ($C_6H_8O_6$) has been proposed to occur according to the following reaction:

$$C_6H_8O_6 + 2Ag^+ \rightarrow 2Ag^0 + C_6H_6O_6 + 2H^+ \qquad (\mathbf{3.1})$$

The reaction stoichiometry indicates in order to complete reduction process of 0.3 mM $AgNO_3$, 0.15 mM AA is required. However, here amount of AA is gradually varied up to 0.2 mM to observe its effect on $AgNO_3$ reduction.

Interestingly, AgNPs solutions exhibit substantial optical density in the UV region below 400 nm. The light yellow colour of the solution is clearly visible in light. A number of studies reported that AgNCs (Ag_4^{2+} or homologues) have considerable absorptions in the UV region.[109, 144, 177] Thus, it is assumed that by photo-reduction process a number of AgNCs particles may generated in the core of RMs by even before the addition of any reducing agent. However, pure (water containing) RMs do not show any such absorption characteristics.

3.3.2. Effect of w_0 = [water]/[AOT] ratio

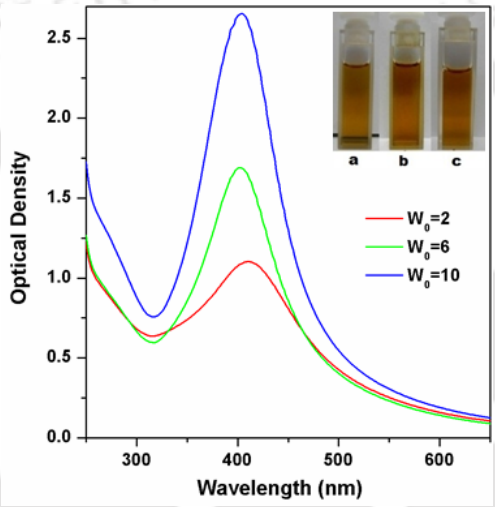

Figure 3.2: Comparison of the UV-Vis spectra of the AgNP formed in the water/AOT/n-heptane reverse micellar and AA systems at different w_0 values (a) w_0 = 2, (b) w_0 = 6, and w_0 = 10. The overall concentrations of AOT, $AgNO_3$ were 90, 0.30 and 0.10 mM, respectively. The inset represents snapshots of these solutions when viewed under ordinary light.

Figure 3.2 represents a detail comparison of SPR bands in various w_0 values with a fixed AA concentration (0.10 mM). Here utmost blue-shifted SPR band by 8 nm (from 410 nm at w_0 = 2 to 402 nm at w_0 = 6 and 10) is observed with increase in the w_0. Moreover, FWHM of the SPR band is larger at w_0 = 2 compared to that at w_0 = 6 or 10. The spectral position and width of SPR maximum significantly depend on the actual sizes of the AgNPs.

As discussed in **Section 1.5.3**, bandwidth of the SPR band is inversely proportional to the size of AgNPs. Thus it is assumed that a larger bandwidth at w_0 = 2

may be due to smaller size AgNPs compared to other w_0 values. Nonetheless, as the w_0 increases from 6 to 10, no significant change of bandwidth is noticed. This may be due to two reasons; either the size remains same at w_0 = 6 and 10, or the effect of the size change may be compensated by a concomitant change in dispersity. These possibilities can be checked by detailed structural characterizations later in this *Chapter*. Very recently, Peng et al. have demonstrated that within the small particle limit (diameter ≤ 12 nm), wavelength corresponding to the SPR maximum display a red-shift with the decrease in size.[179] They modelled their results by introducing a multilayer Mie theory,[179, 203] and assigning different dielectric constants to the core and the shell regions of the nanoparticles. The higher wavelength of the SPR maximum at w_0 = 2 may be due to smaller size of the AgNPs as compared to that for w_0 = 6 or 10. The details of the absorption maxima and FWHM (full width at half maxima) of the SPR bands at different w_0 values are given in *Appendix* **(Table A.3.1)**.

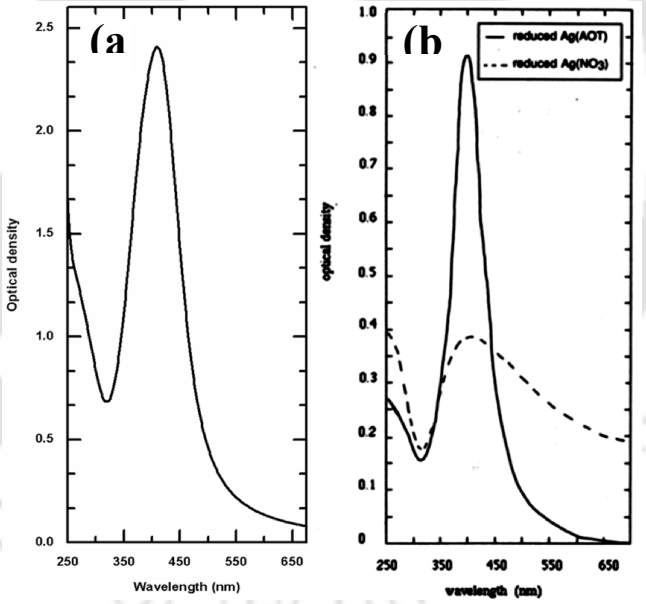

Figure 3.3: Comparison of optical quality of SPR band of AgNP at w_0 =10 obtained in this work with Petit et al.[109] (a) Present work by AA reduction using [AOT] = 0.09 M, [$AgNO_3$] = 0.3×10^{-3} M, [AA] = 0.5×10^{-4} M (b) By Petit et al. via $NaBH_4$ reduction in NaAOT by using (– – –) silver nitrate and (–) silver sulfosuccinate as silver precursor. $[AOT]_{total}$ = 0.1 M; [$AgNO_3$] = [AgAOT] =10^{-3} M, [$NaBH_4$] = 10^{-4} M.

Comparison of optical quality of SPR band of AgNPs at $w_0 = 10$ obtained in this work with Petit et al. is shown in **Figure 3.3.**[109] The SPR maxima in both works approximately match but the FWHM is slightly narrower for Petit et al. As seen in the **Figure 3.3,** Petit et al. use ordinary NaAOT, the plasmon resonance is very board and has significant absorbance in the higher wavelength region indicating heterogeneity in the particle distribution. In our case, in spite of using ordinary NaAOT we get good optical quality and sharp SPR. Above comparison shows that approximately similar quality of SPR is observed without functionalized AOT when ascorbic acid is used as reducing agent.

3.3.3. Comparison with frequently used reducing agents

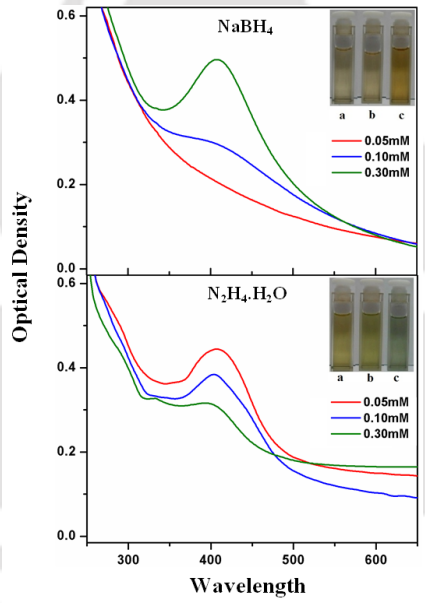

Figure 3.4: UV-Vis spectra of the AgNPs formed in the water/AOT/n-heptane reverse micellar systems at $w_0 = 6$ showing the effect of different reducing agents (top) $NaBH_4$ and (bottom) $N_2H_4.H_2O$ at different concentrations of the reducing agents; 0.05, 0.1, 0.3 mM. The overall concentrations of AOT and $AgNO_3$ were 90 and 0.30 mM, respectively. The inset represents snapshots of these solutions when viewed under ordinary light.

In order to know the role of various reducing agents more convincingly, AA is replaced with two frequently used reducing agents, namely $NaBH_4$ and hydrazine. As seen from **Figure 3.4**, SPR band of AgNPs is much stronger and narrower for AA compared to $NaBH_4$ or hydrazine reduction under similar condition. Note that the

absorption spectrum observed here are somewhat different from that reported in the literature,[109, 144, 177] which may be due to the simpler protocol used in this study. Contrary to our direct loading of precursors into the AOT/non-polar solvent mixture, separate micro-emulsions containing silver ion and reducing agent, respectively, are mixed drop-wise under continuous stirring condition in those studies.[109, 144, 177] This synthetic protocol may favour formation of larger aggregates for these reducing agents as indicated by significant absorption (or scattering) at long wavelengths (**Figure 3.4**). The colours of the solutions prepared by $NaBH_4$ or N_2H_4 reductions are also of much lighter intensity than obtained by the AA reduction method.

3.3.4. Dynamic light scattering measurements

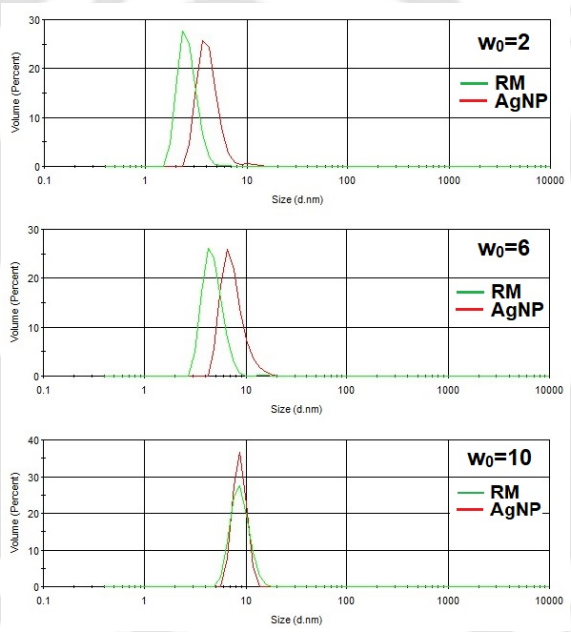

Figure 3.5: Size distributions obtained from dynamic light scattering (DLS) measurements at different w_0 values for pure reverse micelles, and reverse micelles containing the synthesized AgNPs.

DLS measurements are performed in order to estimate the size distribution of the pure RMs and the AgNP-RMs. **Figure 3.5** shows that the size of the RMs increases upon the formation of nanoparticles. The diameters of the pure micelles are found to be 4.8, 5.9 and 8.8 nm at w_0 = 2, 6 and 10, respectively (**Table A.3.2**). The size of the AgNP-RMs at various w_0 values also agree well with the reports of Pileni and coworkers.[109] The average diameter of the AgNP containing RMs are found as 5.3, 6.1 and 8.9 nm at w_0 = 2, 6, 10, respectively. Thus, the striking similarity of our results with

those of Pileni et al. not only supports the rational of our methodology but also highlights the efficiency of our simplistic approach in designing size-controlled AgNPs. Moreover, this method may be considered as a "green route" since we have used biocompatible AA instead of $NaBH_4$. Furthermore, no functionalized surfactants is required, as used elsewhere.

3.3.5. Transmission electron microscopy measurements

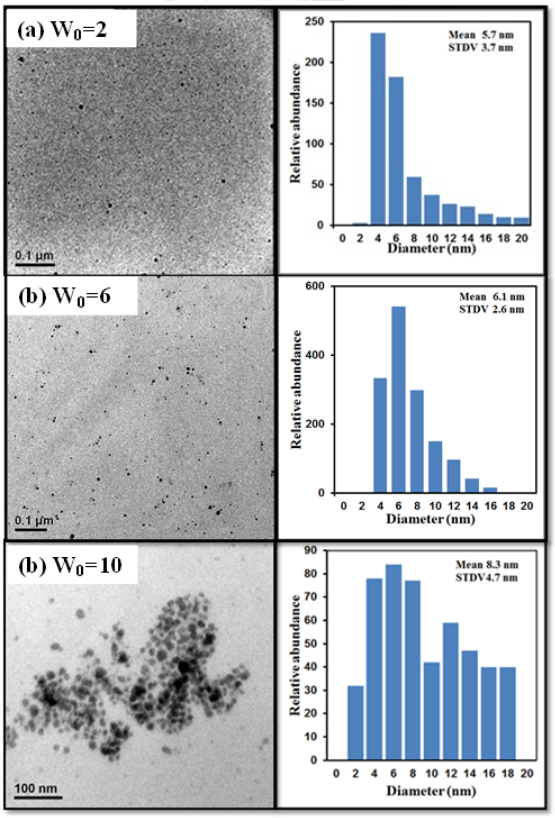

Figure 3.6: TEM images and size distribution histograms of AgNPs synthesized by AA reduction at (a) w_0 = 2, (b) w_0 = 6 and (c) w_0 = 10, respectively. The overall concentrations of $AgNO_3$ and AA were 0.30 and 0.10 mM, respectively.

TEM micrographs (**Figure 3.6**) clearly revels that spherical shape of the nanoparticle at all w_0 values (2, 6 and 10). The sizes of the AgNPs are found to be 5.7 ± 3.7, 6.1± 2.6 and 8.3 ± 4.7 nm at w_0 values of 2, 6 and 10, respectively. Both TEM and DLS results suggest that size of AgNPs increases with increase in the w_0 value, but TEM reports slightly larger values compared to the DLS measurements (see **Table A.3.2** in *Appendix*). This discrepancy may be due to possible change in size (and

sometimes morphology) during the drying process of the sample over TEM grid, which may result in an over-estimation of particle sizes. The TEM results also indicate that the size-distribution is much narrower for the nanoparticles prepared at the $w_0 = 6$ that for the nanoparticles obtained at $w_0 = 10$. Hence, the invariance of the SPR band position observed at $w_0 = 6$ and 10 is due to simultaneous change in size and dispersity.

3.4. MECHANISM OF THE SILVER NANOPARTICLE FORMATION PROCESS

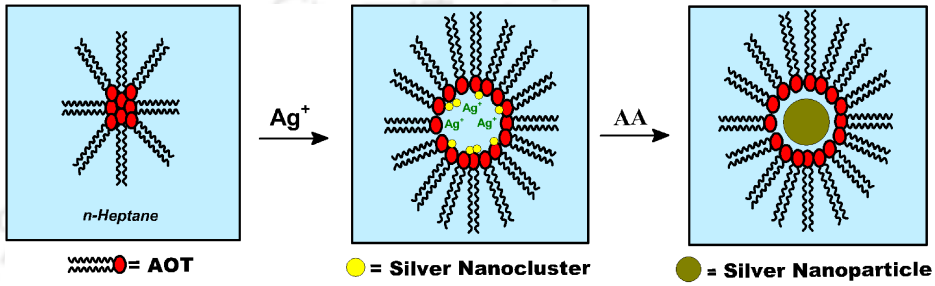

Scheme 3.1: A scheme representing the protocol of the AgNP formation via reverse micellar route. The reduction is proposed to occur via catalysis of intermediate silver nanoclusters (AgNCs) formed within the interfacial region.

AA is believed to be incapable to reduce silver salt in aqueous solution in the presence of micelle [148, 196] or protein.[197] How does AA reduce Ag^+ in reverse micelle? Many researchers have shown evidence for various silver nanoclusters (AgNCs) during AgNP formation in AOT RMs.[109, 144, 177] Here significant optical density is also observed for the $AgNO_3$ containing RMs indicating formation of AgNCs. Recently, Yang et al. demonstrated that AgNCs can catalyse the reduction of Ag^+ by AA at room temperature.[197] By combining these facts, following scheme (**Scheme 3.1**) may be proposed. First, on the addition of $AgNO_3$, Ag^+ binds to the negative sulfonate head-group of AOT. Photoreduction of few Ag^+ to Ag occurs under ordinary light, and subsequently, leads to intermediate formation of nanoclusters within the interfacial region. The nanoclusters may catalyse the reduction of more Ag^+, and ultimately transforms into AgNPs. The mild nature of the reducing agent may account for the monodispersity and high optical quality. Murthy and co-workers suggested that initial nucleation and growth processes should be slow for obtaining narrow size distribution.[204] Otherwise, collision, fusion and splitting of the microemulsion droplet may increase the size distribution.[204] Here, the first step in **Scheme 3.1** is slow as

required for narrow size distribution, while the second step is fast giving rise to high yield of AgNPs in a reasonable time (~ 45 minutes). It is interesting to note that AOT reverse micelles are not just acting as a "passive template" for size-directing the AgNPs, but also help to accelerate a chemical reduction, which is not effective in bulk water at room temperature.

3.5. SUMMARY AND CONCLUSION

In summary, in this *Chapter* an exceptionally easy, yet extremely efficient method to fabricate high optical quality AgNP is presented via microemulsion route using AA as a reducing agent. An advantage of this method is that the precursors (silver ion and AA) can be directly loaded into AOT/*n*-heptane mixtures without prolonged stirring. The UV-Vis studies reveals the high optical quality of the AgNPs, whereas TEM and DLS studies shows that the nanoparticles are spherical in shape, and are slightly larger in size than the pure RMs. We have also shown that AA is more preferable over the commonly used reducing agents $NaBH_4$ and N_2H_4 in AOT reverse micelles.

The spectral width of the SPR band is found to be much narrower than most of the reported methods via the microemulsion route.[144, 147, 168, 194-195] The high optical quality is successfully rationalized based on the mild character of the reducing agent and the catalytic action of the nascent AgNCs supported inside the interfacial region of the RMs. This new catalytic approach may be a valuable for obtaining monodispersed and high optical quality AgNPs via the reverse micellar route.

In conclusion, two important aspects are highlighted in synthesis of AgNPs through the reverse micellar route. First, RMs are hitherto considered as "passive templates" to control size of the nanoparticles; chemical reductions that usually take place in aqueous media have been merely performed in the water pool of the reverse micelles. [144, 147, 168, 194-195] Here, for the first time, RMs can support a chemical reduction that cannot proceed in an aqueous medium at room temperature is shown. Another important objective, a high "optical quality", is also successfully achieved. A good optical quality is particularly desirable, for studying interaction with other absorbing species (e.g. Plasmon-fluorophore interaction[51, 205-206]). In the proceeding *Chapters* using high optical quality AgNPs, delicate photophysical studies are performed.

Chapter-4

Selective probing of the Interfacial Region of AOT Reverse Micelle upon nanoparticle Formation Using Dynamic Stokes Shift Measurements[#]

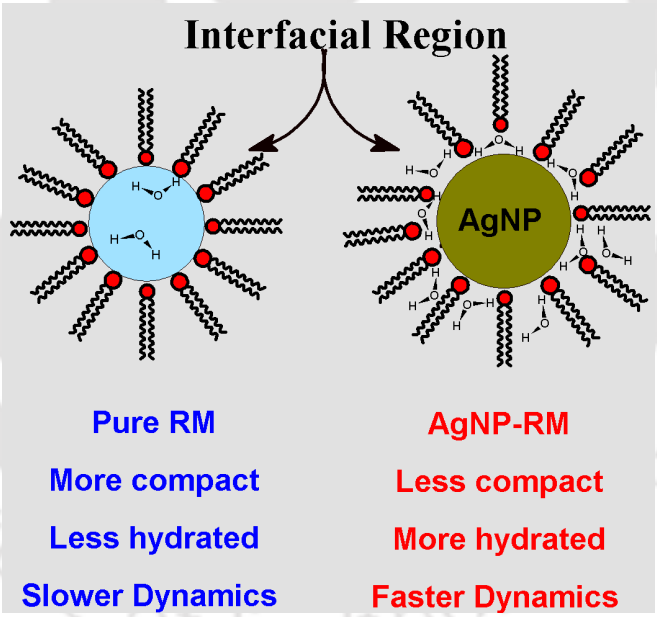

[#] This work has been published in. *J. Phys. Chem. C* **2014**, *118*, 10366-10374.

CHAPTER 4: SELECTIVE PROBING OF THE INTERFACIAL REGION OF AOT REVERSE MICELLE UPON NANOPARTICLE FORMATION USING DYNAMIC STOKES SHIFT MEASUREMENTS

4.1. INTRODUCTION

As discussed in the **Section 1.6**, probing of reverse micellar interfacial layer upon nanoparticle formation provides valuable information. However, best of our knowledge only Sarkar group have initiated some interesting works in probing reverse micellar interfacial layer upon AgNPs formation.[147, 168, 176] Although these results are quite informative, however, several improvements may be incorporated in those studies for getting even finer results. *Firstly,* the SPR band of nanoparticles derived from $NaBH_4$ or glucose reduction are board in nature. Due to very large spectral width of the SPR, the spectral modifications of the fluorophore can be hard to anticipate. *Secondly,* due moderate hydrophobicity and solubility both polar and nonpolar regions, the fluorophores C153 and C480 may partition into a broad regions of the reverse micellar system. As dominant changes are expected to occur inside the water pool or at the interfacial layer upon nanoparticle formation, a minor fraction of fluorophores residing only in those regions are responsible for their observed changes, thus, lowering the chance of monitoring delicate changes. Thus, a more specific probe that preferentially partitioned inside the water pool will certainly provide valuable information.

To restrict the location of the probe over the interfacial and water-pool region, hydrophilic probe fluorophore coumarin 343 (C343) is chosen, which exhibits negligible solubility in nonpolar solvent and hence, one may expect partitioning of the probe only into the water pool and inside the interfacial region (**Scheme 4.1**).[118] Note that these two regions are directly involved in the nanoparticle formation process, thus justifying our selection. Levinger and co-workers have already demonstrated the utility of C343 in probing site-selective solvation dynamics in aqueous and non-aqueous RMs.[81, 118-119] To improve the optical quality of the AgNPs, a facile method is suggested in *Chapter 3*.[18] Presence of weaker reducing agent and due to catalytic nature of the reduction, the method produces nanoparticles with highly improved optical quality (sharp SPR band).

With these essential modifications, it will be shown that our results provide new insights regarding the state of the RMs after nanoparticle synthesis in their core. For example, we will show that the final state is surprisingly simple, comprising of the

nanoparticle containing RMs only, not a combination of nanoparticle containing RMs and empty (without a nanoparticle) RMs. Our results also indicate that the interfacial region of the RMs becomes more hydrated, less packed upon nanoparticle formation particularly at low w_0 value.

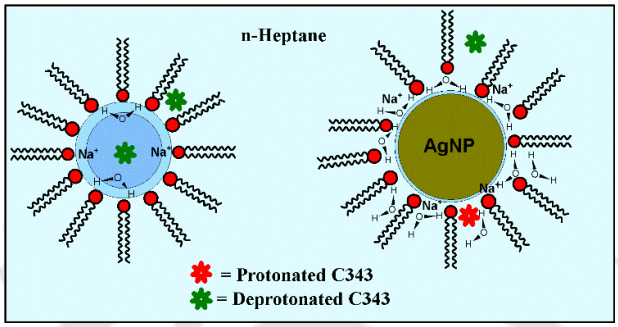

Scheme 4.1: A scheme representing the distribution of the fluorophore coumarin 343 (C343) before and after formation of silver nanoparticles in the RMs. The probe may exist as protonated and de-protonated form in AgNP containing reverse micelle but only as de-protonated form in aqueous reverse micelle.

4.2. RESULTS

4.2.1. Steady state measurements

4.2.1.1. UV-Vis spectra

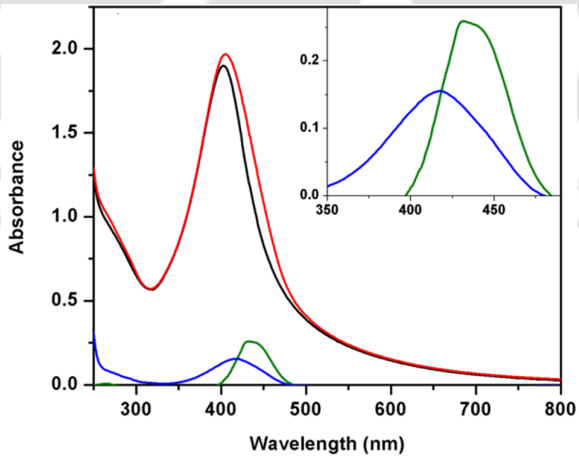

Figure 4.1: The UV-visible spectra of water/AOT/n-heptane reverse micellar system at $w_0 = 6$ comprising (a) AgNPs only (black), (b) C343 and AgNPs (red), (c) C343 only (blue). The green curve represents the difference spectrum [(b)-(c)]. The absorption

spectrum of C343 in the pure reverse micelle and the difference spectrum are compared in a magnified scale in the inset.

In the *Chapter* 3, synthesis of superior optical quality AgNP inside the RMs (AgNP-RM) is demostrated.[18] **Figure 4.1** shows the SPR band at 402 nm for $w_0 = 6$. Addition of ~10 μM C343 to the AgNP-RM system, changes the absorption spectrum very slightly in the wavelength range ~400-470 nm. When same amount of C343 is added into the pure RM, an absorption band with a maximum at 417 nm appears and the maximum optical density is much (~10 times) lower than the SPR band of the nanoparticles. Since, the SPR band of AgNPs has not altered much; it is inferred that the size or morphology of the nanoparticles have not changed much. To find out the absorption contribution of C343, SPR band is subtracted from the fluorophore containing nanoparticle system. The difference spectrum shows a significant red-shift of ~17 nm from the absorption spectrum of C343 in pure RMs. However, such subtraction (isolating individual contribution of nanoparticle and the fluorophore) is only valid if nanoparticle and the fluorophore are non-interacting which may not be true because of strongly overlapped absorption of the fluorophore and the nanoparticle. Similar observations are also noticed for other w_0 values, the spectra and the summary of the absorption maxima are given in the *Appendix* (**Figure A.4.1** and **Table A.4.1).**

4.2.1.2. Fluorescence Spectra

The emission maximum of C343 inside RMs depends markedly on the w_0 value as reported earlier by Levinger and co-workers.[118] With increase in the w_0, the emission maximum gradually shifts to higher wavelength. In a homogenous bulk solvent, emission maximum of a fluorophore is generally independent of excitation wavelength. But, in a heterogeneous medium, the emission spectrum often displays a marked dependence on the excitation energy especially when excited at the higher wavelength (red) side of the absorption spectrum, a phenomena known as the red-edge excitation shift (REES).[207] REES has been reported in a variety of organized assemblies like RMs,[208] lipid vesicle,[209] and polymer micelle[210] and therefore, the magnitude of REES may be taken as an indicator of heterogeneity.

Figure 4.2 shows the emission spectra at various excitation wavelengths for both the pure RMs and nanoparticle containing RMs at $w_0 = 2$. A plot of variation of the emission maxima with the excitation wavelengths at all w_0s is given in the *Appendix*

(**Figure A.4.2**). The observation of the REES in the RMs may be justified by distribution of the probe C343 into the water pool and inside the interfacial layer and considering different absorption and emission characteristics of C343 in each region. From **Figure 4.2**, it is also clear that the amount of REES observed for the nanoparticle containing RMs is much less than that for the pure RMs. Similar reduction in REES is also noticed for other w_0 values and they are tabulated in **Table A.4.2** in *Appendix***.** For example, at $w_0 = 2$, the magnitude of REES is found to be 570 cm^{-1} for the pure RMs but only 300 cm^{-1} for the AgNP containing RMs. Hence, it is inferred that in the AgNP containing RMs, the probe is experiencing less heterogeneous distribution of environments compared to the pure RMs. I will correlate this with other results later in the chapter.

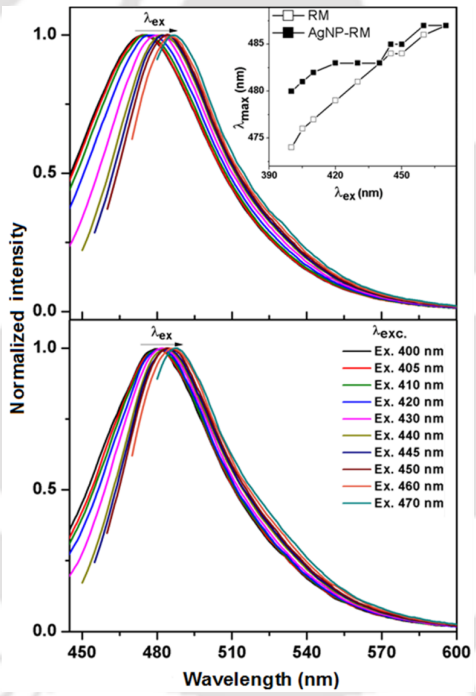

Figure 4.2: Emission spectra of coumarin 343 (C343) at various excitation wavelengths (λ_{ex}) for the pure and the AgNP containing RMs at $w_0 = 2$. The plot of the emission maxima against λ_{ex} for the two cases are shown in the inset.

4.2.1.3. Excitation Spectra

Excitation spectra of the nanoparticle-fluorophore system are measured with the expectation that it could reflect the actual pattern of the absorption spectrum of the fluorophore in the coupled nanoparticle-fluorophore system. The excitation spectrum

is conceptually similar to the absorption spectrum but recorded in different modes. While the absorption spectrum detects the quantity of light absorbed, the excitation spectrum records the quantity of fluorescence generated because of absorption.[211] Note that nanoparticles absorb strongly in the similar wavelength range, where C343 absorbs, but practically do not emit. Hence, nanoparticles, in principle, cannot contribute to the excitation spectrum. However, spectral distortion may take place due to inner filter effect by the highly absorbing nanoparticle SPR. To minimize the effect, the samples are placed in a capillary tube having a very short effective optical path length.

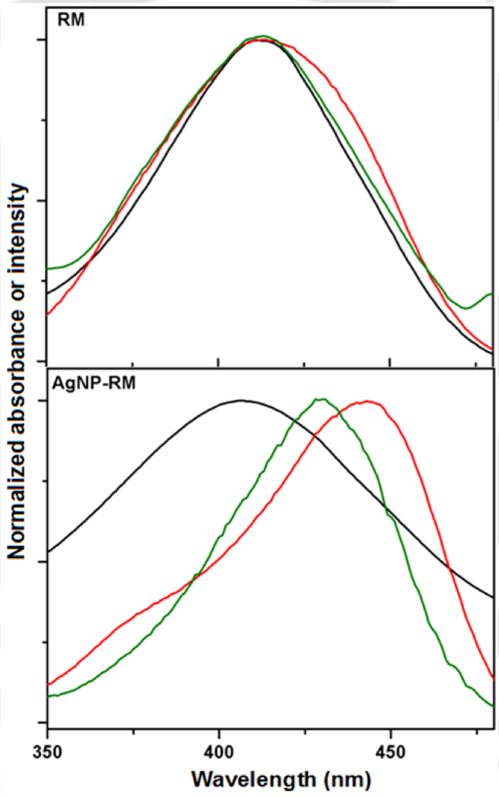

Figure 4.3: Absorption spectrum (black), excitation spectra using a standard 10 mm cuvette (red) and in a glass capillary tube (0.8 mm internal diameter) (green) of C343 in pure RMs (top panel) and in AgNP containing RMs at $w_0 = 2$ (bottom panel). The excitation spectra are recorded at an emission wavelength of 490 nm.

Figure 4.3 reveals that excitation spectrum of C343 in RMs (taken either in an ordinary 10 mm cuvette or in a glass capillary) nicely correlates to the corresponding absorption spectrum as expected. The C343 peak positions for different systems at

different w_0 values are listed in the *Appendix* (**Table A.4.1)**. The similarity is obvious because C343 solely accounts for the both the absorption and the emission (in the excitation mode) and the inner filter effect is negligible. On contrary, the excitation spectra of the nanoparticle-C343 system taken using standard cuvette and by the glass capillary have different shapes compared to the corresponding absorption spectra of C343-nanoparticle system (**Figure 4.3**). The excitation spectrum recorded by the glass capillary has qualitatively similar appearance of C343 absorption spectrum in pure RM. Actually, the excitation spectrum is narrower and red-shifted from the absorption spectrum and SPR contribution is eliminated because of its non-fluorescent nature. In 10 mm path length cuvette, the blue wavelength side of the excitation spectrum may be re-absorbed due to inner filter effect. It is inferred that the excitation spectrum recorded using a glass capillary (free from inner filter effect) effectively represents the absorption spectrum of C343 in the coupled C343-nanoparticle system.

It is also obvious that the maximum of the excitation spectrum of C343 in AgNPs system is markedly red-shifted compared to the absorption or excitation maximum in the pure RMs. Similar red-shifted absorption is also reported for C343 absorbed on the surface of oxide nanoparticles.[123, 212] It is ascribed to the neutral form of the dye which shows absorption at much higher wavelength compared to the anionic form.[213] Hence, it is assumed that a significant fraction of the dye may present in the neutral (protonated) form near the AgNP surface while C343 remains mostly in the anionic (de-protonated) form in the pure RMs. Comparison of excitation and absorption spectra for other two w_0 values are given in the *Appendix* (**Figure A.4.3**).

4.2.2. Transmission electron microscopy measurements

To check any morphological changes after fluorophore addition, TEM images of the nanoparticle are taken in the presence and in the absence of the fluorophore C343 at a particular w_0 value ($w_0 = 6$). The TEM images show that the added C343 has almost no effect on the mean size and the distribution (**Figure 4.4**). The average diameter of the AgNPs was found be 6.0 ± 2.9 nm and 6.1 ± 2.6 nm, respectively, in the presence and in the absence of C343 at $w_0 = 6$.

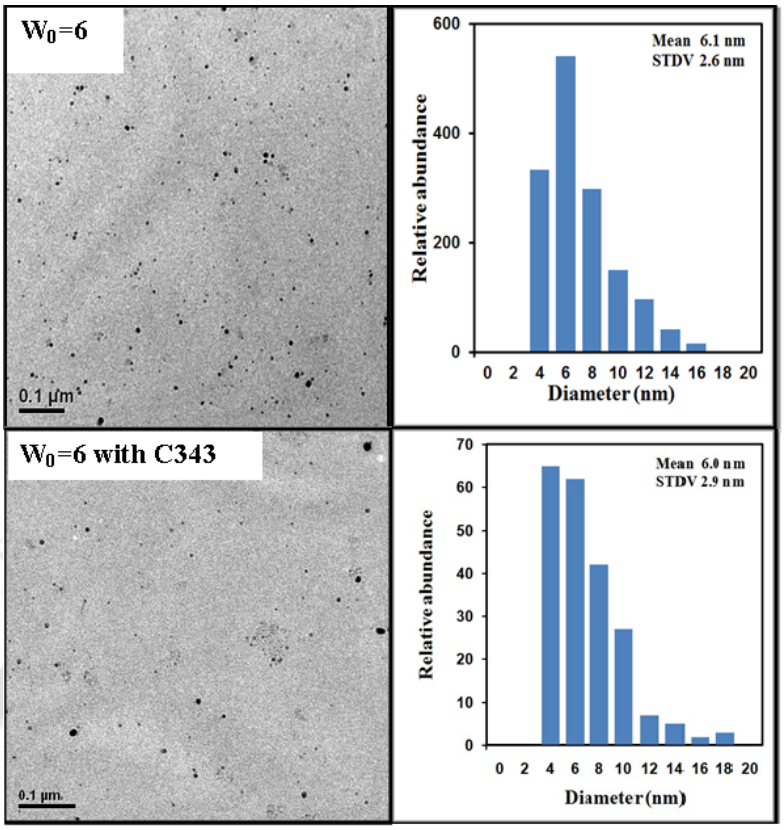

Figure 4.4: TEM images and size distribution histograms of the AgNPs in RMs at w_0 = 6 in (a) the absence of C343 (top) (b) in the presence of 10 µM C343 (bottom).

4.2.3. Time Resolved Studies

4.2.3.1. Fluorescence anisotropy decay

In order to check any morphological fluorescence anisotropy decay. The decay of fluorescence anisotropy provides important information regarding the location of the molecular probe as the rotational time depends strongly on the rigidity (or viscosity) of the environment. **Figure 4.5** shows rotational anisotropy decay of C343 in pure RMs and AgNP containing RMs. The anisotropy decays are found to be bi-exponential for both the RMs and AgNP containing RMs at all the w_0 values (**Table 4.1**). For aqueous RMs the two components may be ascribed to the rotational dynamics of the probe in two different locations- inside the interfacial layer and in the water pool. The slower component (1.8-2.4 ns) may be assigned to the C343 located in the interfacial layer while the faster component (0.33 ns) may be due to the probe rotation in the water pool (**Table 4.1**). Note, as the value of w_0 increases, the both the components decreases

indicating that effective mobility sensed by the C343 decreases for both the water pool and inside the interfacial layer at higher water contents. Note that for $w_0 = 2$, the average rotational correlation time of C343 in the AgNP containing system ($<\tau_r> = 1440$ ps) is significantly faster than in the aqueous RMs ($<\tau_r> = 1760$ ps). However, the anisotropy decays of the two systems progressively merge as the w_0 value increases (**Figure 4.5** and **Table 4.1**).

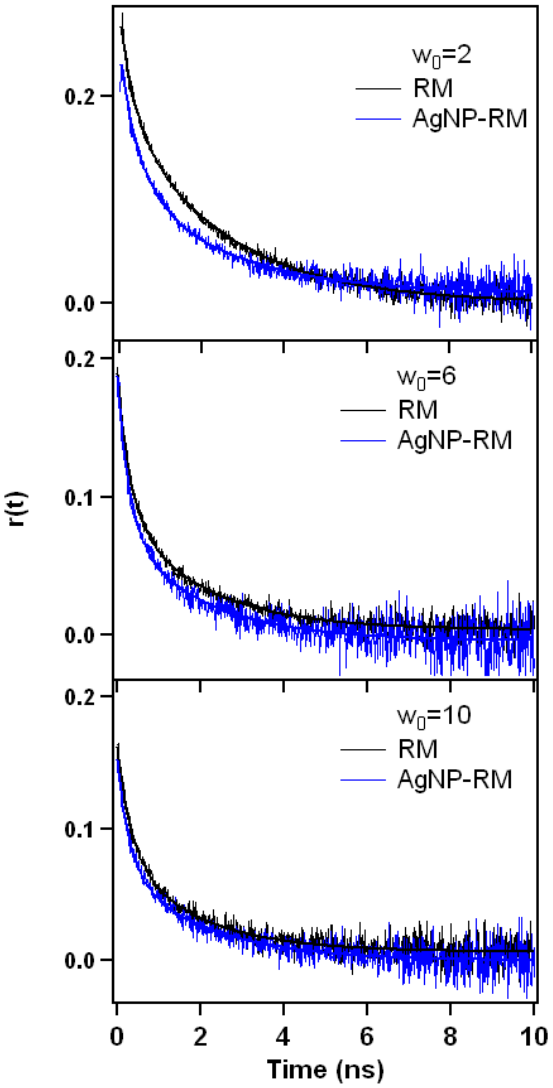

Figure 4.5: Fluorescence anisotropy decays, r(t) of C343 recorded at 470 nm and excited at 405 nm in the pure RMs (RM, black) and in the silver nanoparticle containing RMs (AgNP-RM, blue) at different w_0 values.

Table 4.1. Decay parameters of fluorescence anisotropy, r(t) of C343 in pure and in silver nanoparticle containing RMs at w_0 values of 2, 6 and 10.

System	w_0	r_0	a_1	τ_{r1} (ps)	a_2	τ_{r2} (ps)	$^{\S}\langle\tau_r\rangle$ (ps)
RM	2	0.28	0.33	332	0.67	2460	1760
	6	0.18	0.53	330	0.47	1980	1100
	10	0.15	0.50	335	0.50	1825	1080
AgNP-RM	2	0.23	0.49	450	0.51	2395	1440
	6	0.19	0.57	285	0.43	1975	1010
	10	0.15	0.53	295	0.47	2045	1115

$^{\S}\langle\tau_r\rangle = a_1\,\tau_{r1} + a_2\,\tau_{r2}$

4.2.3.2. Solvation dynamics

The fluorescence transients are recorded at several wavelengths spanning the steady-state emission spectrum, shows significant wavelength dependence for both the pure RMs and AgNP containing RMs (**Figure A.4.4).** As discussed in *Chapter 2***,** TRES are constructed by following reconstruction protocol of Maroncelli and Fleming[191] and solvent correlation function, C(t) is calculated. The decay of C(t) in pure RMs is fitted well with a bi-exponential function and the parameters are summarized in **Table 4.2.** The slow component may be attributed to the hydration dynamics in the interfacial layer where the motion of water molecules is drastically reduced. The relatively faster component may be ascribed to the solvation dynamics in the water pool. Note that both components are much slower compared to the sub-picosecond solvation dynamics in bulk water.[214-215] Interestingly, solvation dynamics in the nanoparticle containing RMs is found to be faster than in aqueous RMs particularly at low w_0 (**Figure 4.6**). At higher w_0 values, average solvation dynamics of the AgNP containing RMs and the pure RMs are very close to each other.

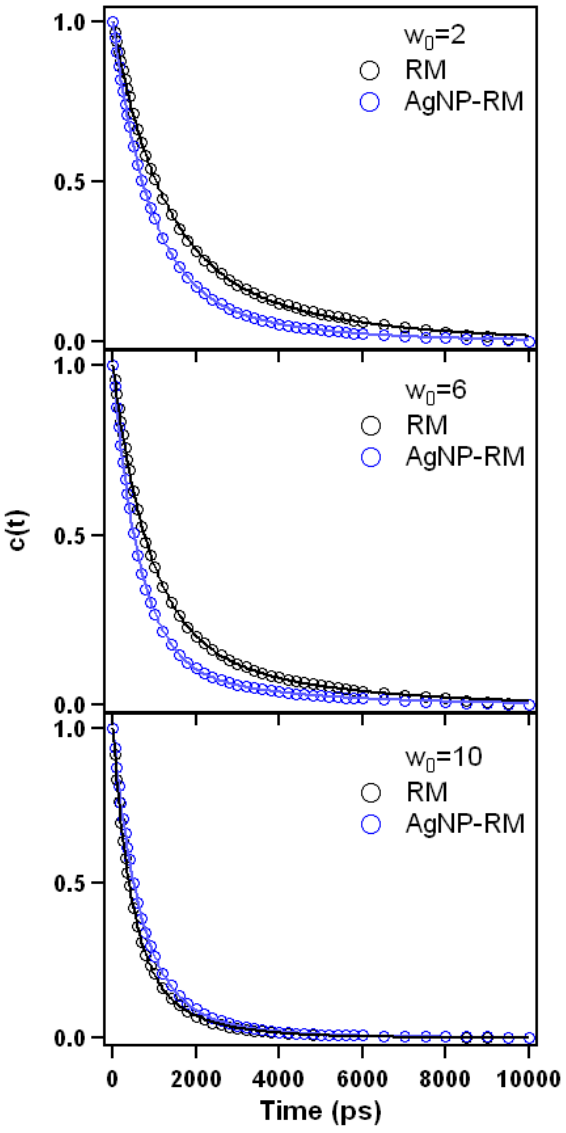

Figure 4.6: Decay of the solvent response function, C(t) of C343 in pure (o) and silver nanoparticle containing (o) RMs at w_0 values of 2, 6 and 10. The points represent the actual values while the solid lines denote the best fit to bi-exponential decay.

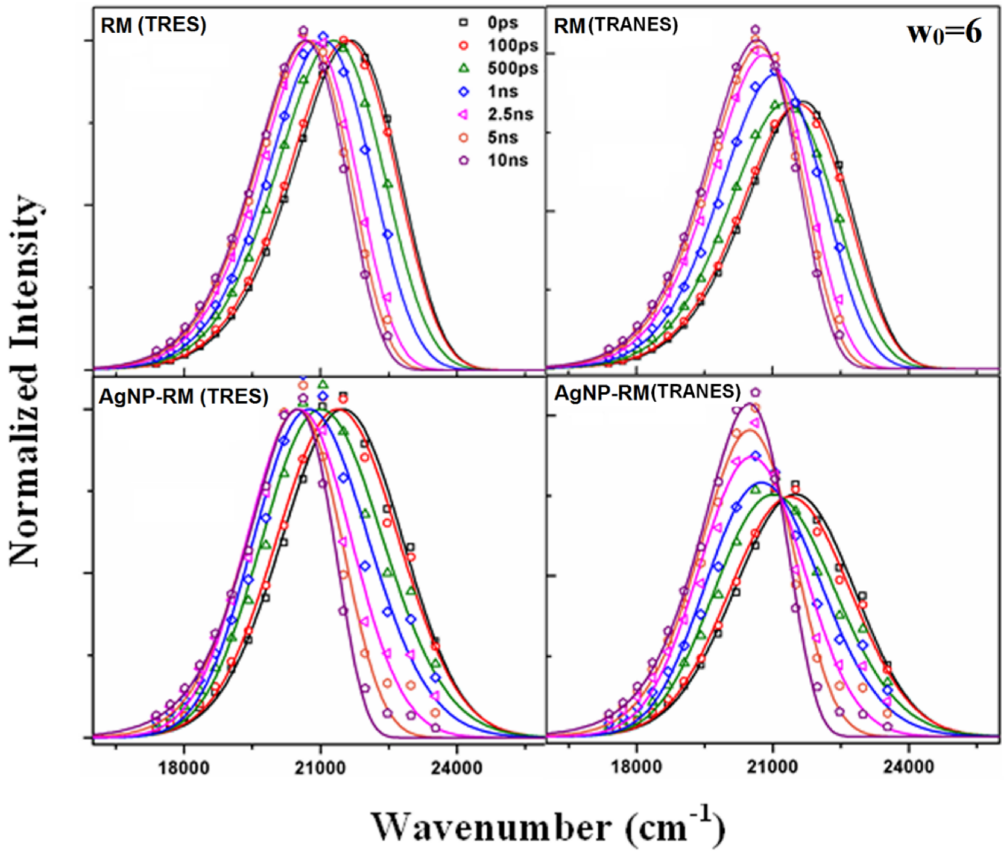

Figure 4.7: Time resolved emission spectra (TRES) and time resolved area-normalised emission spectra (TRANES) spectra of the C343 at different time in pure (RM) and silver nanoparticle containing (AgNP-RM) reverse micellar system at $w_0 = 6$.

Time resolved area-normalized emission spectra (TRANES) are constructed by normalizing the area of each spectrum in TRES. Although, TRANES are just a modified representation of TRES, sometimes provide important information regarding the number of emissive species in the excited state.[216-217] According to Periasamy and co-workers, an isoemissive point in TRANES implies the presence of two distinct emissive species in the excited state.[216-217] **Figure 4.7** shows the normalized TRES and TRANES for both the pure RMs and the nanoparticle containing RMs at $w_0 = 6$. A clear isoemissive point is observed in the TRANES for the nanoparticle containing RMs but not in the pure RMs. TRES and TRANES at $w_0 = 2$ and 10 for both the pure RM and AgNP-RM are included in the *Appendix* (**Figure A.4.5**). The isoemissive point may be due to two forms of the fluorophore in the system. Earlier, from the red shifting of the C343 excitation spectrum of AgNP-RM compared to pure RM, it is commented that a

part of the probe may present in the neutral (protonated) form. Hence, the TRANES implies that the two forms (protonated and de-protonated) may coexist in the nanoparticle containing system. Note that even if the probe stays in multiple forms, in principle, it would not affect the measurement because solvation dynamics depends mainly on the dipole change upon excitation.[123]

Table 4.2: Decay parameters of solvent response function, C(t) of C343 in pure and in silver nanoparticle containing RMs at w_0 values of 2, 6 and 10.

System	w_0	$\Delta\upsilon(cm^{-1})$	a_1	τ_1 (ps)	a_2	τ_2 (ps)	§<τ> (ps)	% obs.
RM	2	1220	0.68	1100	0.32	3490	1860	60
	6	1005	0.75	840	0.25	3220	1430	50
	10	915	0.73	440	0.27	1400	700	50
AgNP-RM	2	745	0.80	840	0.20	2780	1230	56
	6	1010	0.86	630	0.14	3000	960	84
	10	780	0.83	630	0.17	1810	830	65

§$\langle\tau\rangle = a_1\tau_1 + a_2\tau_2$

4.3. DISCUSSION

It is worthy to mention first that solvation dynamics in RMs may occur on a wide time range,[118, 218] Hence, a set up with limited time resolution and observation time window, detects only a part of the total dynamics. In our setup of ~100 ps resolution, sub-picosecond components, if any, will obviously be remained undetected. However, one can estimate the percentage of total dynamics Stokes shift observed in a set up by a method prescribed by Fee and Maroncelli.[219] According to the method, the true time-zero emission frequency in a polar medium, $\nu_{em}^{p}(0)$ can be calculated as

$$\nu_{em}^{p}(0) = \nu_{abs}^{p} - [\nu_{abs}^{np} - \nu_{em}^{np}] \qquad (4.1)$$

where, ν_{abs}^{p}, ν_{em}^{np} and ν_{abs}^{np} respectively, denotes the steady state frequencies of absorption of the fluorophore in the polar medium, emission and absorption maxima of the fluorophore in a nonpolar solvent. For nonpolar solvent, reported absorption and emission maxima of C343 in n-heptane is used as 407.5 nm and 434.3 nm, respectively.[220] One can easily estimate the percentage of total dynamics observed by taking the ratio of the observed dynamics Stokes shift to the calculated total Stokes shift found with the aid of **Equation 4.1**.

For pure RM, calculation shows that 40-50% of the total Stokes shift is missed in our measurement. Earlier, Levinger and co-workers[118] demonstrated that in RMs a considerable amount of solvation dynamics occurs in sub-picosecond time range and obviously cannot be detected in our set up. To estimate the true time zero, the required absorption frequency of C343 within the nanoparticle system, is taken from the maxima of the excitation spectrum. Note that the calculation is not possible using the UV-Vis absorption spectrum because both C343 and the AgNPs strongly overlap with each other. As mentioned earlier, the excitation spectrum may be free from the contribution of AgNPs as the later do not emit. Unfortunately, the very broad nature of the absorption spectrum dominated by the surface plasmon resonance of the nanoparticle may restrict Sarkar and co-workers to estimate the percentage of solvation dynamics.[147, 168]

The most interesting point is that solvation dynamics and the fluorescence anisotropy decays become faster in the AgNP containing RMs than in pure RMs particularly at very low water content. As the value of w_0 increases both the dynamics become gradually similar. Also note that solvation dynamics and rotational dynamics are bi-exponential in both the aqueous and AgNP containing RMs. Several groups have reported the non-exponential nature of solvation dynamics in pure RMs earlier.[118, 208, 218] The non-exponential nature can be explained based on the distribution of the probe into the interfacial region and in the water pool. Levinger and coworkers found that for very low water content (w_0 = 1.1), the solvation dynamics do not have any ultrafast component, hence, the slow component can be ascribed to the interfacial region.[118] Bhattacharyya and coworkers also found bi-exponential solvation dynamics for C343 in AOT RMs which they ascribe to the solvation dynamics of the interfacial layer. The solvation dynamics of C343 residing in water pool may be ultrafast (sub-picosecond) which cannot be detected in our set up. Similarly, for the AgNP containing RMs the bi-

exponential solvation dynamics may be due to the C343 residing in the interfacial layer. The faster solvation dynamics compared to the aqueous RMs may imply that AgNP formation may perturb the interfacial layer and the perturbation is large for the smaller sized RMs.

It may be noted that the fluorophore C343 containing a carboxylic acid group may exist in two different (protonated and de-protonated) forms (**Scheme 4.1**). One may argue that the two forms may complicate the analysis of the steady state and time resolved results and hence needs a critical consideration. The pK_a of C343 is 4.65 and thus, it may remain mostly in the de-protonated form in the aqueous RMs.[221] Hence, the observed REES may solely due to heterogeneous distribution of the anionic C343 into the water pool and in the interface. However, in the nanoparticle grown RMs C343 may remain as a mixture of forms because of slight acidic nature of the medium (as ascorbic acid is used in the synthesis). Hence, observed REES may be due to the two forms of the fluorophore. The observation of isoemissive point in the TRANES further supports simultaneous existence of the two forms. The protonated form absorbs and emits at higher wavelength compared to the de-protonated form.[213] The two forms differ considerably in their absorption maxima but marginally in their emission maxima.[213] As C343 absorption generally shows a red shift when absorbed to a nanoparticle surface,[123] it may be assumed that the protonated form stays close to the AgNP surface while the de-protonated form may reside away from the interface (**Scheme 4.1**).

It important to check whether the difference in dynamics for the two systems (aqueous and AgNP containing RMs) arise merely due to two different forms of the probe (C343). Earlier, Pant and Levinger reported that the solvation dynamics should be independent of the form of C343 as the pK_a of the dye is same in both ground state and the excited state.[123] To confirm further, we have also measured solvation dynamics and anisotropy decay in RMs containing same concentration (0.1 mM) ascorbic acid at all the w_0 values. Solvation dynamics inside the ascorbic acid containing RMs is rather slightly slower compared to the aqueous RMs (see **Figure A.4.6** in *Appendix*). The slowing down of the solvation dynamics may be due to increased confinement for the presence of ascorbic acid inside RM. Hence, the faster solvation dynamics observed inside the AgNP containing RMs may not be due to different chemical form of C343 but due to structural reorganization of the interfacial layer upon nanoparticle formation. We have also checked that the anisotropy decays of C343 in both aqueous and ascorbic

acid containing RMs and found they are similar in both the cases (see **Figure A.4.6** in *Appendix)* Hence, we may conclude that the two forms of C343 nearly follow similar solvation and rotational relaxation.

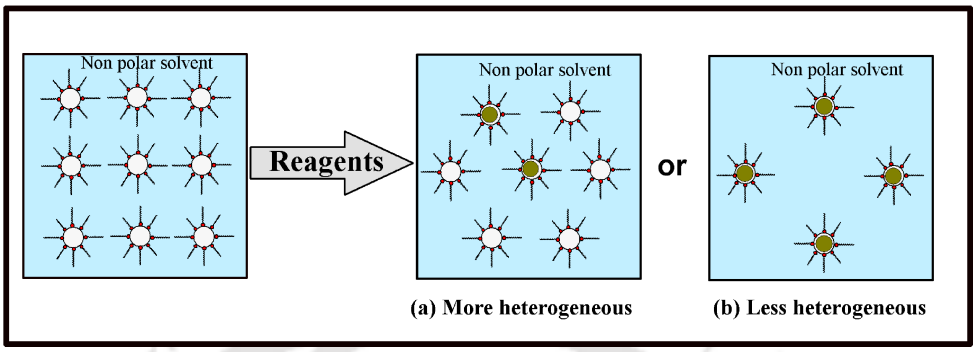

Scheme 4.2: Possible fates of the reverse micellar system after nanoparticle formation- (a) mixture of empty and nanoparticle containing RMs (i.e. more heterogeneous) or (b) only nanoparticle containing RMs (i.e. less heterogeneous).

The mechanistic understanding of the nanoparticle synthesis inside RM is far from complete despite of many proposals.[222-224] For example, can we predict the final state after nanoparticle formation? Simple calculations show that the number of RMs at the beginning is much (2-4 orders of magnitude) greater than the number of nanoparticle formed at the end. Hence, the final state is either a mixture of nanoparticle containing RMs and large fraction of empty (without a nanoparticle) RMs or just the nanoparticle containing RMs where most of the surfactants get adsorbed onto the surface of the nanoparticle (**Scheme 4.2**). In the first case, it would lead to more heterogeneous distribution of the probe while in the second case probe only stays in the surfactant layer around the nanoparticle. Lower REES is found in nanoparticle containing RMs compared to pure RMs. Hence, our results suggest lesser distribution of C343 and thus favor the second possibility.

We may shed light on the reorganization of interfacial surfactant layer of the RMs upon nanoparticle formation. For this we first need to know the sizes of the RMs before and after nanoparticle formation. From *Chapter 3*, it is found that upon nanoparticle formation the hydrodynamic diameter of the RM increase from 4.8, 5.9, 8.8 nm at w_0 = 2, 6 and 10 to 5.3, 6.1, 8.9 nm respectively (**Section 3.3.4**). Note that size increment upon nanoparticle formation is most significant (~10%) at w_0=2 but is negligible at higher w_0 values. Thus, it is expected that AgNP has a greater influence

on the structural reorganization of the interfacial layer at low value for its accommodation inside the very small core, while at large w_0 values, reorganization of the interfacial layer is insignificant. This nicely correlates to the observed dynamics, most change at low w_0 but nearly identical at higher w_0.

4.4. CONCLUSION

Steady state and time resolved optical measurements are applied to investigate the change in the microenvironment of the reverse micellar template, before and after formation of nanoparticle. It is found that both the solvation dynamics and fluorescence anisotropy of the molecular probe, C343 become faster in the nanoparticle containing RMs compared to the aqueous RMs at low w_0 values but the difference becomes negligible at higher w_0 values. The observed change in dynamics is nicely correlated to the structural change of the RMs during nanoparticle formation. At low w_0, size of the RMs increases most upon nanoparticle formation than at higher w_0 values. Hence, the relatively faster dynamics at low water content may be attributed to the more perturbed or less organized interfacial layer.

Chapter-5

Interaction of Molecular Transition with Surface Plasmon Resonance of Silver Nanoparticle inside Restricted Environment of AOT Reverse Micelles[#]

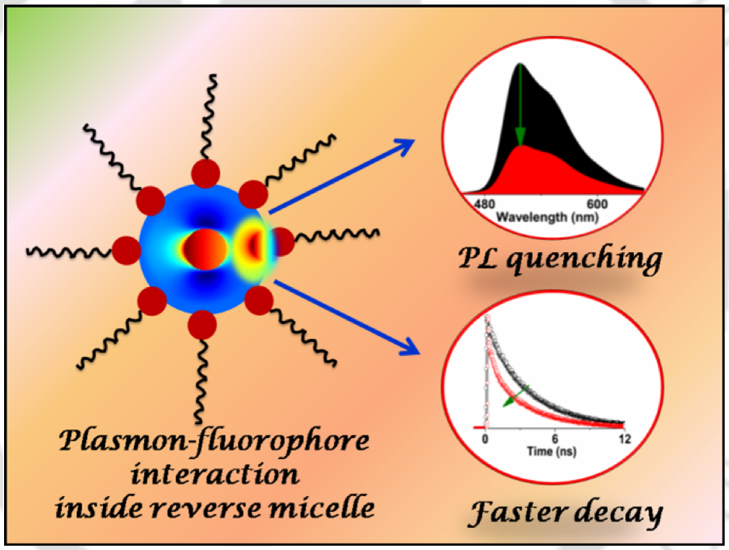

[#]This work has been published in *ACS Omega* **2017**, *2*, 5494-5503.

CHAPTER 5: INTERACTION OF MOLECULAR TRANSITION WITH SURFACE PLASMON RESONANCE OF SILVER NANOPARTICLE INSIDE RESTRICTED ENVIRONMENT OF AOT REVERSE MICELLES

5.1. INTRODUCTION

In this chapter, application of superior optical quality AgNPs in plasmon-fluorophore (PF) interaction is demonstrated. The concept of PF interaction is discussed in the **Section 1.2**. Two charged fluorophores- fluorescein (FL) and safranin O (SAF) are chosen for identifying the PF interactions inside water pool of AOT RMs. The charged fluorophores are partitioned preferentially inside the RM rather than in the continuous non-polar phase (*n*-heptane) and exhibit a significant overlap of the AgNPs SPR (**Scheme 5.1**) and hence provide a suitable system to study PF interaction (see **Section 1.2**). These two fluorophores are extensively used in cellular imaging and detection and in a number of studies involving PF interactions for details see **Section 1.2.**

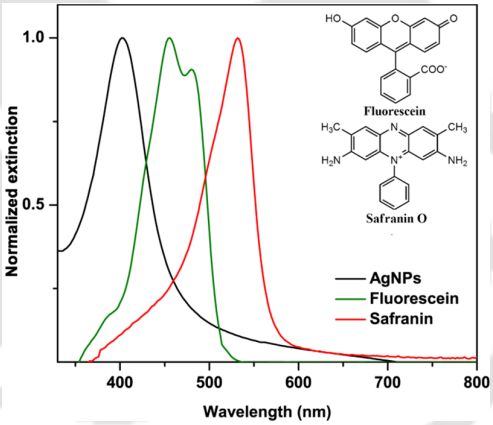

Scheme 5.1: Overlap of extinction spectra of silver nanoparticles with absorption spectra of fluorescein and safranin along with chemical structure of fluorescein (FL), and safranin O (SAF) molecule.

Interestingly, in spite of extensive use of FL dye in PF interactions (**Section 1.2**), there are several inconsistencies within different reports available in literature. For example, Lim et al. claimed 83% emission quenching when FL interacts with citrate stabilized AuNPs.[64] On the other hand Rabga et al. reported 3 fold emission enhancement when FL interacts with AgNPs synthesized using same synthetic protocol of citrate stabilization.[65] Parkin and coworkers found that trivial interaction when FL interacts with citrated capped Au or AgNPs.[66]

Here a novel controlled way to study PF interaction is developed between AgNPs and molecular fluorophores inside the restricted environment of RMs. The natural capacity of a RM is utilized to act simultaneously as a template for nanoparticle formation and to encapsulate the dye. Here, only ~1 μM of fluorophore is used and at this low concentration dye aggregation may be ignored. Moreover, the dye and the reagents required to form the nanoparticle are added together into the RM core and *in situ* spectral and the size evolution of the RM system is continuously monitored to detect any spectral or size changes occurring at any instance.

5.2. RESULTS

5.2.1. Extinction properties of the Fluorophore-Plasmon composite systems

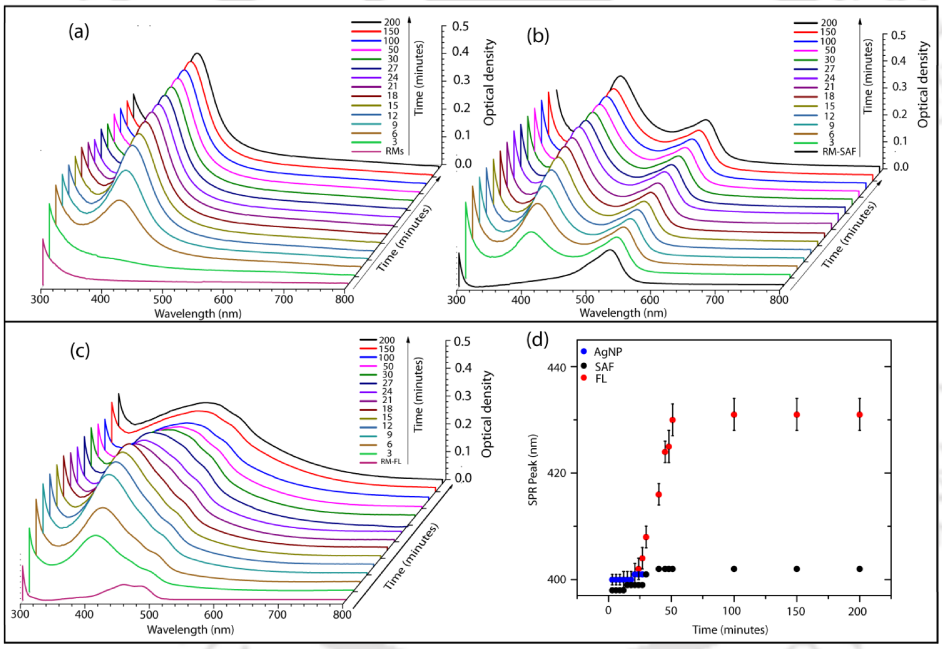

Figure 5.1: Evolution of extinction spectra of different systems with time: (a) AgNP inside AOT reverses micelle, (b) AgNP and safranin O in RM (c) AgNP and fluorescein in RM. The variation of SPR maxima with time for various systems is added in plot (d).

The growth of AgNPs after dissolution of Ag^{+} into the water pool of RM is monitored by recording the extinction spectra at different time interval. **Figure 5.1a** shows that the SPR of AgNP gradually develops with time; a clear SPR peak at ~ 400 nm can be easily visible after 6 min. With time, the SPR band intensity continues to grow for ~ 18 minutes but the SPR peak position remains invariant with time (**Figure 5.1d**).

To study the PF composite systems, fluorophore concentration was kept low (~ 1 μM) to ensure that only monomeric form of the fluorophore prevails inside the RMs. As soon as silver ions dissolve into the water pool of RMs containing a fluorophore, AgNPs formation takes place and PF interaction, if present, may observed. For both the systems containing only AgNPs and SAF-AgNPs composite have similar reduction time of ~18 minutes (**Figure 5.1b**).The absorption maxima of SAF are at 533 nm inside RM both in the absence and in the presence of AgNP. When SAF absorption spectra in the RMs solution (in the absence of silver precursor) are subtracted from the absorption spectra of the AgNP-SAF composite at different times, spectral pattern similar to SPR of AgNP (in the absence of fluorophore) can be recovered (see **Figure A.5.1** in *Appendix***)**.

In the FL-AgNP conjugate, SPR peak also reaches maximum at ~18 minutes. However, unlike SAF, with further progress of reaction, the SPR band of the FL-AgNP conjugate depletes along with a remarkable red shift (**Figure 5.1c**). At initial time (e.g. ~6 minutes), FL-AgNP conjugate shows several bands at different wavelengths designated as λ_1(~402 nm), λ_2(~455 nm) and λ_3(~483 nm). These peaks may be assigned as SPR of AgNP (λ_1) and the mono-anionic form of FL dye (λ_2 and λ_3). These three peaks persisted up to~18 minutes (i.e. time need to complete the reduction process). λ_1 peak shifting starts at ~18 minutes and the shifting process continued unto ~100 minutes and finally the λ_1 peak was shifted by ~ 30 nm. Saini et al. reported similar type of depletion along with splitting of AgNPs SPR when Chlorine-P6 dye gradually added to poly-*l*-lysine capped AgNP.[62] The spectral characteristics observed here may appear that nanoparticles undergo aggregation; however, structural characterization reveals that FL has trivial effect on the size and distribution of AgNP which will be discussed later in the chapter.

To represent the FL coupling more effectively we have performed a simple convolution analysis (**Figure 5.2**). We assume that if there is no interaction between the SPR and fluorophore, the extinction spectrum of the SPR-fluorophore composite should be similar in appearance to the added spectrum of the two separate systems. It is evident from **Figure 5.2** that the bands of the composite system do appear at the same position like that of the individual systems. However, for AgNP-FL system, the spectrum of the composite system does not have any similarity with the calculated

combined systems. The combined spectrum shows three peaks at ~430 nm ,~ 455 nm and ~483 nm which are close to the peaks of the AgNP (400 nm) and FL (455 nm and 483 nm) alone. The composite system only shows a broad peak at ~ 430 nm indicating formation of a very different hybrid system.

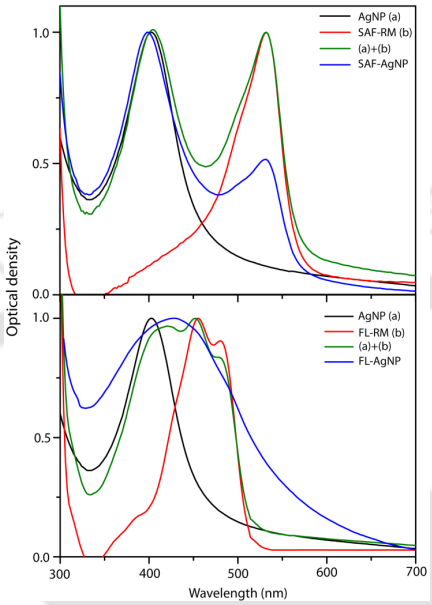

Figure 5.2: Normalized UV-visible extinction spectra of only AgNP, only fluorophore and AgNP-fluorophore composite and calculated combined (AgNP+fluorophore) extinction spectrum. Safranine O (SAF) and fluorecein (FL) are respectively used in the top and bottom panels. Extinction spectrum of the AgNP-SAF system has strong similarity with the comibed spectrum but the extinction spectrum of the AgNP-FL system deviates much from the calculated spectrum.

Modification of the spectrum can be attributed to either aggregation of AgNPs or hybridization of SPR and molecular absorbance via PF coupling. Kitching et al. reported modification of SPR due to aggregation of AgNPs or AuNPs.[66] However, Wang et al. and other researchers claimed the PF coupling induced spectral modification.[7, 40]

5.2.2. Structural Characterization of AgNPs and AgNPs-FL Composite System

Figure 5.3 shows the changes in the hydrodynamic diameters of FL containing RMs when AgNPs gradually form. The hydrodynamic diameter is found to be 6.9 nm, approximately matching with the expected diameter (**Equation 1.6**). After 18 minutes

(time need for complete reduction of AgNPs), hydrodynamics diameter increases from 6.9 to 8.7 nm (see **Table A.5.1** in *Appendix*). The enlargement of RM may be due to swelling of RMs upon formation of AgNP within the core of RM. Thereafter, no abrupt change in hydrodynamic diameter is observed at longer time delay, although a minor increase in polydispersity is observed at very long time (~ 1000 minutes). Thus, time dependent DLS measurements give a clear indication that spectral change in SPR band in the presence of FL is not merely due to the change in morphology of AgNPs. DLS measurements are further augmented by TEM measurements (see **Figure A.5.2** in *Appendix*); FL has only trivial effect on the mean size and the distribution of AgNPs. The average diameter of the AgNPs is found to be 6.1 ± 2.6 nm and 6.5 ± 3.1 nm in the presence and in the absence of FL, respectively.

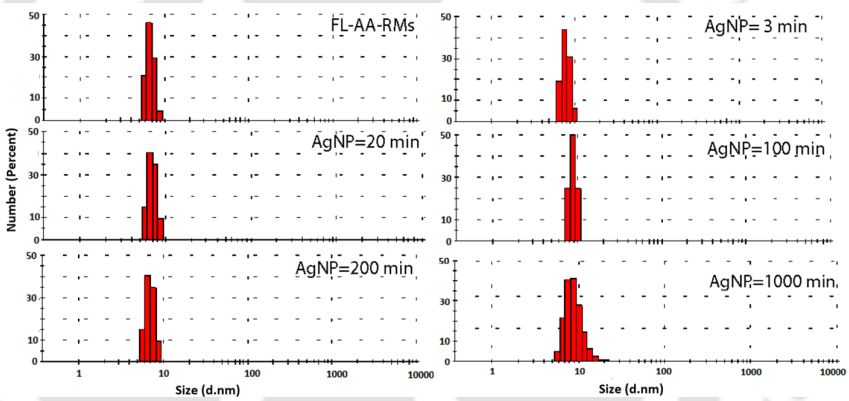

Figure 5.3: Dynamic light scattering measurements of FL-AgNPs composites at different time.

5.2.3. Emission properties of the Fluorophore-Plasmon composite systems with time

In order to check, whether AgNPs formation and corresponding SPR has any impact on the optical properties of the fluorophore, the excitation and emission spectrum of the fluorophore inside the RMs is measured in the absence and in the presence of AgNPs (**Figure 5.4**). No notable peak shift is observed either for the excitation or emission spectrum, when AgNPs is formed inside RMs. Invariance of peak position gives clear indication of invariance in the chemical form of FL and SAF before and after AgNPs formation. However, emission intensity of FL decreases with gradual formation of AgNPs within the RM. The fluorescence intensity steadily

decreases up to ~ 40 minutes; thereafter, no appreciable change in quenching is observed. This can be rationalized on the basis of the fact that during the growth of AgNPs the free FL molecule may be adsorbed on the surface of AgNPs. Attachment process of dye is further enhanced due to the presence of both dye and AgNPs inside restrict confined environment of RMs. The quenching is more prominent for FL; almost ~ 62 % of the initial fluorescence decreases after AgNP formation. The quenching is almost insignificant (<10%) for SAF in the presence of AgNP. The quenching in fluorescence intensity of FL after AgNP formation is very apparent when the systems are viewed under a hand held UV lamp (362 nm) but no detectable change is observed for SAF (see **Figure A.5.3**. in *Appendix*).

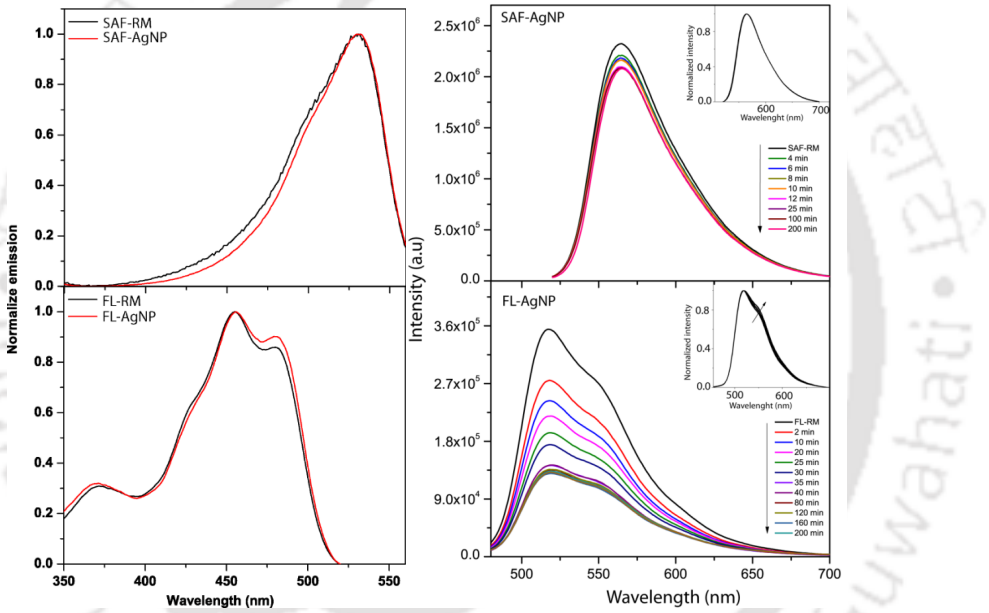

Figure 5.4: Variation of steady state excitation (left panel) and emission intensity of safranin (λ_{ex} = 510, λ_{em} = 570 nm) and fluorescein (λ_{ex} = 445 nm, λ_{em} = 530 nm) in the presence of growing silver nanoparticle with time inside reverse micellar solution. Inset of right panel shows normalized intensity of respective fluorophore and arrow indicates increase in shoulder peak with time. For clear visibility of peak position in excitation spectrum only spectra before and after complete growth of AgNPs are provided.

5.2.4. Time-resolved fluorescence properties Fluorophore-Plasmon composite

Fluorescence anisotropy decays of FL and SAF are shown in **Figure 5.5** before and after complete growth of AgNPs. It is evident that the anisotropy decay of both the dyes becomes faster upon AgNPs formation. The average rotational correlation time

($\langle\tau_r\rangle$) for FL in RMs is found to be ~ 2.46 ns (**Table 5.1**). This agrees the average rotational time (τ_r = 2.50 ns) of FL in AOT RMs for FL at w_0 = 7 reported by Dutt.[225] As seen from **Table 5.1** the fluorescence anisotropy becomes slightly faster upon AgNP formation within the RMs. A marginal decrease of rotation time is observed when system changes from RMs to AgNP RMs. On other hand for SAF, a substantial decrease of $\langle\tau_r\rangle$ from ~ 3.70 ns to ~ 2.07 ns is observed by changing the system from RMs to AgNP-RMs.

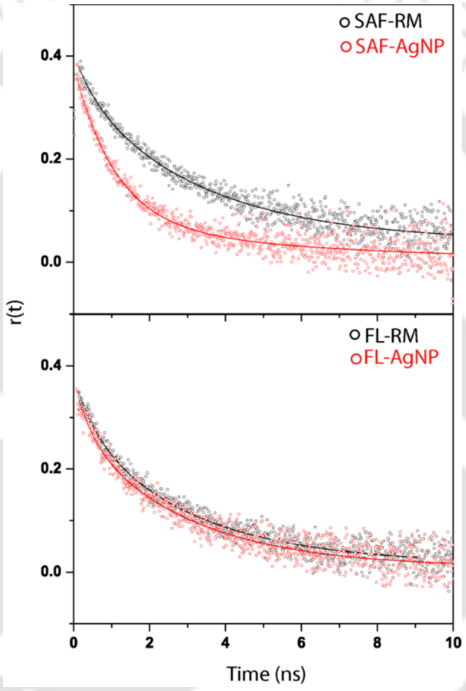

Figure 5.5: Fluorescence anisotropy decays, r(t), of safranin (λ_{ex} = 510 nm, λ_{em} = 565 nm) and fluorescein (λ_{ex} = 405 nm, λ_{em} = 520 nm) before and after complete growth of AgNPs.

The very different anisotropy behaviours of the two fluorophores upon AgNP formation can be rationalized on the basis of location of the fluorophores inside RM prior to AgNPs formation. FL mainly remains inside the water pool whereas SAF predominately resides at the interfacial region of RMs.[124, 225] The large change in the anisotropy decay of SAF may be associated with the marked reorganization of RM interface upon AgNP formation. Interface may become less organized upon formation of AgNP which may expose SAF more into the external non-polar phase. This may

increase the local motion of the fluorophore, resulting in faster fluorescence anisotropy decay. Note that the rotational relaxation time of free SAF in homogenous solvent is quite fast.[226] On the other hand, since FL resides in water pool, it may have minor change in microenvironment.

Table 5.1: Time resolved anisotropy decay parameters of the safranin and fluorescein in RM before and after complete growth of silver nanoparticle (AgNP).

Fluorophore	System	a_1	τ_1/ns	a_2	τ_2/ns	$\langle\tau\rangle$/ns[§]	$\langle\chi^2\rangle$
Safranin	RM	0.16	5.97	0.84	3.27	3.70	1.08
	AgNP	0.20	6.01	0.80	1.08	2.07	1.05
Fluorescein	RM	0.21	0.56	0.79	2.96	2.46	1.16
	AgNP	0.24	0.43	0.76	2.85	2.27	1.07

[§]$\langle\tau_r\rangle = a_1\tau_{r1} + a_2\tau_{r2}$

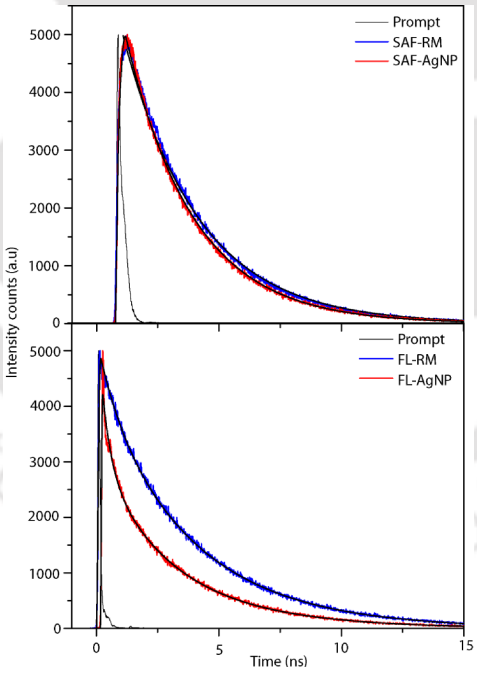

Figure 5.6: Fluorescence decays of safranin (λ_{ex} = 510 nm, λ_{em} = 565 nm) and fluorescein (λ_{ex} = 405nm, λ_{em} = 520 nm) inside AOT reverse micellar solution, before and after AgNPs nanoparticle formation.

Figure 5.6 represents fluorescence decays of both FL and SAF in RMs before and after complete growth of AgNPs. The decay of SAF almost remains unaffected upon nanoparticle formation. This is consistent with the negligible change in the steady state emission. However, the fluorescence decay of FL becomes much faster after formation of AgNP. The decay of FL in RMs can be fitted with a bi-exponential function with time constants of 1.20 ns (16%) and 3.8 ns (84%) as shown in **Table 5.2.** Interestingly, in FL-AgNPs system, FL decay becomes more non-exponential and a reasonable fit needs at least three exponential components- 0.35ns (34%), 2.71 ns (28%) and 3.9 ns (38%). The average decay time shortens significantly from 3.4 ns in RMs to 2.2 ns in AgNP-RM. For SAF, only a marginal decrease in average decay time from 3.0 ns in RMs to 2.78 ns in AgNP-RM is observed.

Table 5.2: Fluorescence decay analysis, radiative and non-radiative rates and energy transfer efficiencies of the safranin and fluorescein inside RMs and after complete growth of silver nanoparticles (AgNP).

Dye	System	a_1	τ_1 (ns)	a_2	τ_2 (ns)	a_3	τ_3 (ns)	$<\tau>^{\S}$ (ns)	ϕ^*	k_r (ns^{-1})	k_{nr} (ns^{-1})	ϕ_{ET} (%)
SAF	RMs	1	3.07	-	-	-	-	3.07	0.25	0.081	0.24	
	AgNP	1	2.78	-	-	-	-	2.78	0.22	0.081	0.27	9
FL	RMs	0.16	1.20	0.84	3.88	-	-	3.45	0.03	0.009	0.28	
	AgNP	0.34	0.35	0.28	2.17	0.38	3.9	2.20	0.01	0.005	0.44	36

$^{\S}<\tau_r>= a_1\tau_{r1}+ a_2\tau_{r2}$, $^*\phi$=quantum yield,

According to radiative plasmon model proposed by Lakowicz et al., the presence of metal NPs near vicinity of fluorophore, substantially modifies the decay rates of fluorophores.[44] Thus, strong decrease of FL decay time indicates modification of either radiative (k_r) or non-radiative (k_{nr}) pathways of FL in the presence of AgNPs. From quantum yield and excited state life time measurements, k_r and k_{nr} can be easily calculated as follows

$$k_r = \frac{\phi}{\tau} \quad \textbf{(5.1)}$$

$$k_{nr} = \frac{1-\phi}{\tau} \quad \textbf{(5.2)}$$

where, ϕ and τ_0 are quantum yield and lifetime of fluorophore, respectively. Thus, observed radiative (k_r) or non-radiative (k_{nr}) decay rates of FL in RMs solution 0.081ns^{-1}and 0.27ns^{-1}, respectively. Interestingly, in the presence of AgNPs substantially modifies non-radiative decay rates (from 0.28 ns^{-1}to 0.440 ns^{-1}). Thus, it is inferred that the observed changes in PL emission time is primarily due to non-radiative energy transfer from photo-excited FL to AgNPs, which is mentioned in steady state quenching studies. The non-radiative energy transfer efficiency (η) and rate of energy transfer (k_{ET}) can be calculated by using following equations

$$\eta = 1 - \frac{\tau_{DA}}{\tau_D} \qquad \textbf{(5.3)}$$

$$k_{ET} = \frac{1}{\tau_{DA}} - \frac{1}{\tau_D} \qquad \textbf{(5.4)}$$

Where, τ_D and τ_{DA} represent life time of donor (FL) in the absence and presence acceptor (AgNPs). As seen from **Table 5.2** the calculated energy transfer efficiencies and energy transfer rate for FL-AgNPs pair found to be 36% and ~1.6×10^8 s^{-1}, respectively. For SAF energy transfer efficiency and rate found to be 9% and 0.3×10^8 s^{-1} respectively. Thus energy transfer can be effectively tuned by precise selection of molecular dye. From steady state and time resolved data, it is clear that FL molecule may be located in the close vicinity of AgNPs. Since rate of energy transfer depends on the spectral overlap between donor and acceptor besides separation distance between the coupling pair, FL dye satisfies both the criteria and hence, a high rate of energy transfer occurs. Conversely, low rate of energy transfer for SAF-AgNPs pair can be rationalized on the basis of the fact that SAF predominantly present in interfacial region and no appreciable overlap with AgNPs SPR.

5.3. DISCUSSION

Our main objective of the present investigation is to probe the modification of the absorption and emission characteristics of a molecular fluorophore by SPR of AgNPs inside the confinement of AOT RMs. AgNP is chosen as its SPR band shows around 5 times stronger excitation coefficient than AuNPs; additionally, AgNPs are also known to exhibit stronger PF coupling than AuNPs.[227-228] Usually, the extent of PF coupling depends on spectral overlap and distance between the molecular absorber and the metal nanoparticle. Thus, the two representative pairs, uncoupled (SAF-AgNPs)

and coupled (FL-AgNPs) are produced by judicious selection of fluorophores. Steady-state and time-resolved studies revealed that indeed a strong interaction between FL and AgNPs takes place but only a trivial interaction is observed for SAF-AgNPs conjugates.

Usually, interaction of metal nanoparticle with a closely placed molecular absorber occurs via two well accepted mechanisms: electromagnetic and chemical. The interaction of electric field of the surface plasmons with the absorption or emission transition dipole of the molecule constitutes the electromagnetic part. On the other hand, mixing of metal states with the electronic states of the molecule is considered as the chemical mechanism.[20, 44, 227] Interaction with AgNP does not alter the excitation or emission maxima of the either of the fluorophores which implies that the energy levels of the fluorophore remains same before and after coupling with the SPR. A strong reduction of emission intensity and lifetime is noted for FL upon interaction with nanoparticle. These are in accordance with the electromagnetic influence of the PF coupling.

The fluorophore FL may remain in different chemicals forms depending on the pH of the medium. A concern is that AA used as reducing agent here may change the pH of the medium. The effect of AA on the optical characteristics of fluorescein in water and in micellar medium has been investigated in detailed by De and coworkers.[53] They demonstrated that AA has significant effect on the protonation equilibrium of FL in aqueous medium. In aqueous solution FL mainly exists in dianionic form but with the increase of AA concentration, monoanionic, neutral and even cationic form may dominate at very high concentration. However, they have not reported any reduction of FL molecules in the presence of AgNP. Here a control experiment is performed to study the effect of AA on spectroscopic properties of FL dye inside AOT RMs at $w_0 = 6$ (see **Figure A.5.4** in *Appendix*). In the absence of AA, the absorption and the excitation spectrum of FL shows two peaks of similar strengths at 483 nm and 455 nm. This feature is mainly characteristics of the monoanionic form of FL.[225] With the increase of AA concentration, the relative contribution of 455 nm increases compared to 483 nm peak. In addition, fluorescence intensity of FL is also quenched significantly with the increase of AA concentration. These observations clearly indicate gradual conversion of the monoanionic form of FL molecule into neutral form inside RMs core with increase of AA and is consistent with the observation of De and co-workers.[53]

The pH of the medium before and after nanoparticle formation is also estimated (see **Figure A.5.5** in *Appendix*)**.** Since, FL is a pH-sensitive probe, its excitation and fluorescence spectra may change with the concentration of AA. This may complicate the observed fluorescence quenching. However, it is well known that the water pool of AOT RM displays a buffer-like behaviour. This means that pH of the internal water pool is relatively less sensitive with respect to externally added acid or base. A number of studies have been devoted to study such buffer like action of water pool of RMs.[113, 122] Using a ratio-metric approach on the excitation spectrum of fluorescein, Hasegawa showed that water pool of AOT RMs behaves as a buffer for a wide range of bulk pH (2-12).[113] I estimated the pH of the water pool at different conditions from the calibration curve obtained from the FL excitation spectra. The pH of the medium changes very slightly in the presence of various additives such as AA (AA-FL), silver nanoparticles (AgNP-FL). Thus, it is evident that very negligible change in pH is occurred in presence of different additives.

The possibility of aggregation of FL in the presence of AgNP may an important concern. Hence, deliberately take very low concentration of fluorophore (~1 μM) is taken to avoid any aggregation. Simple calculation reveals that the number of RMs is 2-3 order of magnitude higher than the number of FL molecule. Thus, it is very unlikely that two FL molecule may reside in same reverse micellar core in order to form aggregates In addition, the excitation spectrum of FL is known to be very sensitive to aggregation.[53] The invariance of the excitation peak position of FL before and after AgNPs formation further supported that no aggregation of FL takes place (**Figure 5.4**).

Now, the distribution of nanoparticle and fluorophores inside the reverse micellar system is considered. As residual positive charges may exist on AgNPs surface, therefore, surface attachment with negatively charged FL molecule is highly probable (**Scheme 5.2**). It is reported that the nucleation process for the AgNP formation inside RM takes place via Ag_4^+ clusters which finally converted into AgNP.[229] Furthermore, invariance of time-resolved anisotropy decays suggests that FL molecules may not penetrate the AOT surfactant barrier when AgNPs is formed, in other words most of the FL molecule attached with AgNPs surface. As residual positive charge on AgNPs interface are stabilized by negatively charged capping agent AOT, after formation of AgNPs inside the RMs no water pool practically exists. It is unlikely that SAF molecule penetrates the negatively charged surfactant layer and attach with

AgNPs surface, rather it may present in interfacial region (**Scheme 5.2**). Note that interfacial region is the place where maximum perturbation is expected when AgNPs formed inside RMs core. Significantly faster anisotropy decay of SAF after AgNPs formation may arise from its presence in the interfacial region. A minor decrease (~10%) of QY of SAF indicate a trivial interaction with AgNPs and the reduction of QY may be due to emitted photons are reabsorbed by AgNP by means of inert filter effect. This also supported by lifetime measurement where no change in fluorescence decays is observed. Based on above discussion **Scheme 5.2** is design showing probable distribution of dyes and plasmon-fluorophore interaction of silver nanoparticles inside AOT reverse micellar system.

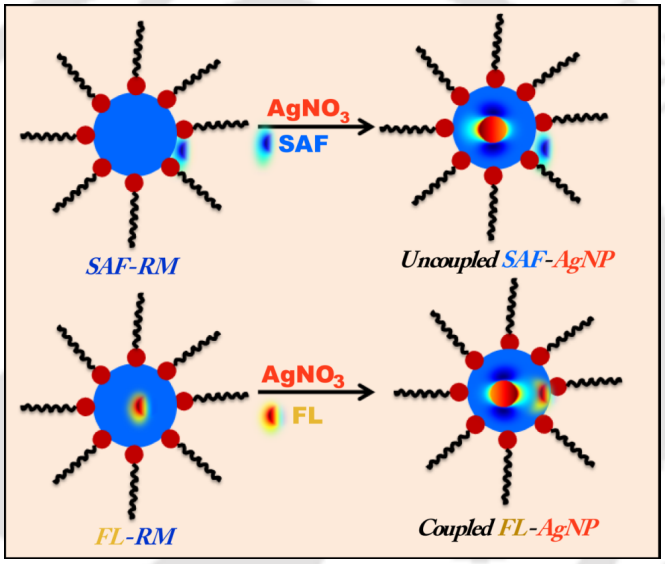

Scheme 5.2: Probable distribution of dyes and plasmon-fluorophore interaction of silver nanoparticles inside AOT reverse micellar system.

The remarkable modification of the extinction spectrum of the SPR band of AgNPs during the progress of the FL−AgNP composite can be due to the PF coupling, change of refractive index around the nanoparticle or due to aggregation of nanoparticles induced by the fluorophore. Since, any appreciable difference in the TEM image of the composite system do not observed from that of the AgNP in RM, thus one may exclude the possibility of aggregation. However, possibility of nanoscale aggregation of small AgNPs (say < 3 nm) cannot ruled out the within the RM core induced by FL because TEM and DLS are not sensitive to these microscopic aggregations. A strong coupling of the SPR band of the metal NPs with the excitation

state of the fluorophore may generate two new states with upper and lower energies. A significant change in the local refractive index around NPs may occur when a molecular fluorophore binds to the NP surface. In all of the aforementioned cases, usually a red shift is noticed in the PF composite system. Because one can only resolve the low-energy SPR band (at~430 nm) but not the high-energy one, hence the shift of the SPR may ascribe to the change in the refractive index. However, because of significant spectral broadening, the presence of a high-energy peak cannot be ruled out, and hence other possibilities may also prevail.

5.4. CONCLUSION

In conclusion, an easy and convenient way to study *in situ* plasmon-fluorophore coupling is demonstrated by confining both the fluorophore and gradually developing nanoparticle inside RMs. For two fluorophores FL and SAF, very different spectral modification is observed. For the SAF-AgNPs composite, the extinction spectrum is simple superposition of the SPR band of AgNP and the absorption spectrum of SAF. However, for the FL-AgNPs composite, extinction spectrum modulates strongly; the original SPR band at ~ 400 nm depletes strongly while a new peak develops at ~ 430 nm. However, the absorption, excitation and emission spectra of FL do not show any shift of its molecular transition frequencies in the presence of AgNP. Moreover, TEM and DLS measurements revealed very less morphological change of the AgNP in the presence of FL. Thus, the modification of the extinction spectrum of the SPR band may not be because of the aggregation of AgNPs but is attributed to the plasmon-fluorophore coupling. In the FL-AgNPs composite system, quenching of the fluorescence intensity and the decrease of lifetime of FL is attributed to the energy transfer from the fluorophore to the metal nanoparticle. The very different spectral behaviour of the FL-AgNPs and SAF-AgNPs was due to a combination of different fluorophore-plasmon distance distribution inside the RM and different spectral detuning of the molecular transitions from the SPR band of AgNP.

Chapter-6

Anomalous Spectral behavior of 4-Aminophthalimide inside Non-Aqueous Acetonitrile Microemulsion: Implication on Reverse Micelle to Bi-Continuous Microemulsion Transition[#]

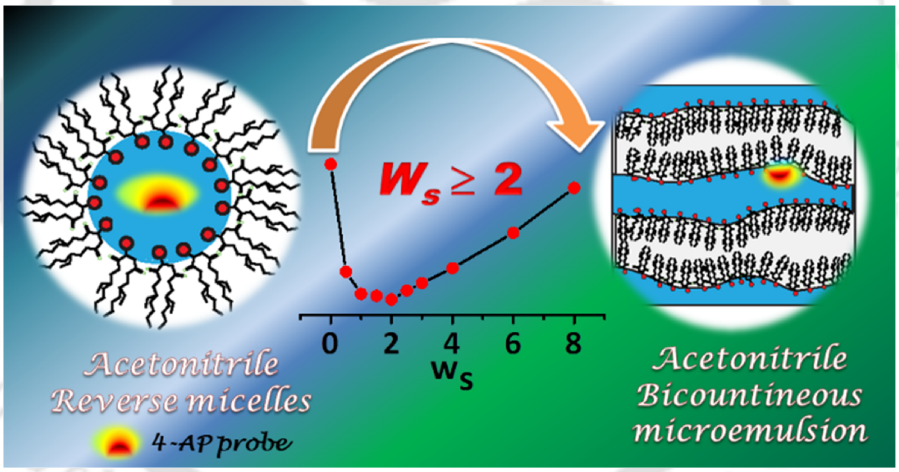

[#]This work has been published in *J. Phys. Chem. B* **2018**, *122*, 6966-6974.

CHAPTER 6: ANOMALOUS SPECTRAL BEHAVIOR OF 4-AMINOPHTHALIMIDE INSIDE NON-AQUEOUS ACETONITRILE MICROEMULSION: IMPLICATION ON REVERSE MICELLE TO BI-CONTINUOUS MICROEMULSION TRANSITION

6.1. INTRODUCTION

Microemulsions are primarily composed of two immiscible (or partially miscible) solvents and a surfactant (**Section 1.3**). Since, initial studies are carried out with water and oil, microemulsions are usually classified as oil-in-water (o/w), water-in-oil (w/o) and another non continuous phase is bi-continuous microemulsions (BMCs).[125] BMCs mostly arises at an intermediate polar solvent content, in which both polar and non-polar solvents form nanochannels delineated by a layer of surfactants (**Scheme 6.1**).[230]

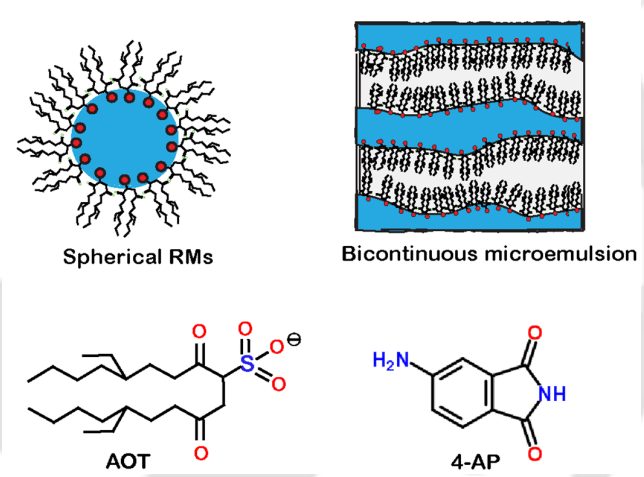

Scheme 6.1: Representation of RM and bi-continuous microemulsion models along with the chemical structures of the surfactant sodium 1,4-bis(2-ethylhexyl)sulfosuccinate (AOT) and the fluorophore 4-aminophthalimide (4-AP).

The nature of the microemulsion remains debated when acetonitrile is used as a polar solvent. Despite of numerous investigations, whether acetonitrile is effectively sequestered by AOT molecules to form true RM droplets at any w_s still remains ambiguous and consequently, Levinger and co-workers define this system as *problem system*.[77] Early DLS measurements revealed that hydrodynamic radii of the microemulsions do not change upon variation of acetonitrile content.[81] The absence of swelling is considered to be a clear deviation from true RMs characteristics and hence, Levinger and co-workers suggested that acetonitrile based system should better be

termed as microemulsion without definite interfacial boundary and these microemulsions may behave as BMC.[81]

Solvation dynamics in acetonitrile microemulsion behaves very differently compared to that in aq-RMs (aqueous RMs) and other nonaq-RMs (non-aqueous RMs). Shirota and Horie first reported that the solvation dynamics of an anionic fluorophore C343 does not change with variation of w_s inside acetonitrile microemulsion.[89] Sarkar and co-workers also found only trivial change of average solvation time with variation of w_s for several coumarins– C152, C152A, C153 and C490.[86-88, 231] In these studies, they assumed formation of RM first and then explained the w_s-independent solvation dynamics behavior based on the absence of H-bonding inside encapsulated acetonitrile and weak intermolecular interaction of acetonitrile with SO_3^- group of AOT.[86-88, 231] Noticeably, in all these studies, starting acetonitrile-microemulsions above w_s = 2. However, a majority of nonaq-RMs such as formamide and ethylene glycol etc. show RM characteristics at very low w_s (<2) and therefore, it may be interesting to know the property of acetonitrile containing microemulsions particularly at lower w_s content.

In this chapter the controversial acetonitrile/AOT/*n*-heptane microemulsion is probed with a hydrophilic fluorophore 4-aminophthalimide (4-AP) and the modulation of spectral and dynamical response is monitored with variation of w_s. The advantage of the use of 4-AP is that it is completely insoluble in *n*-heptane and ultrasensitive to environmental properties. Steady-state and time-resolved spectroscopic behaviors of 4-AP modulate very differently in the low ($w_s < 1$) and high ($w_s > 1$) w_s regimes indicating a phase transition from RM to BMC.

6.2. RESULTS

6.2.1. Absorption and Emission spectra of 4-AP in acetonitrile/AOT/n-heptane microemulsion

Absorption spectrum of 4-AP in AOT solution of heptane ($w_s = 0$) shows two prominent bands at 305 nm and 363 nm (**Figure 6.1a**) corresponding to two different electronic transitions, $S_0 \rightarrow S_2$ (B_2 band) and $S_0 \rightarrow S_1$ (B_1 band), respectively.[180, 232] Upon addition of acetonitrile, the peak positions most remain same but the absorbance of both the bands increases. This may be due to enhancement of the solubility of 4-AP at higher acetonitrile content.

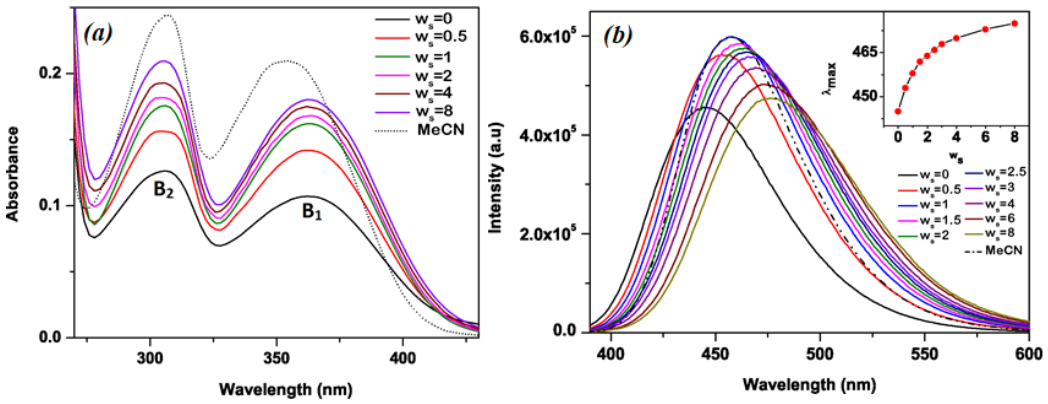

Figure 6.1: (a) Absorption spectra of 4-AP in acetonitrile/AOT/*n*-heptane microemulsion at different w_s. Absorption spectrum of neat acetonitrile (dotted line) is also included for comparison (b) Emission spectra ($\lambda_{ex.}$=360 nm) of 4-AP in acetonitrile/AOT/*n*-heptane microemulsion at different w_s values. Inset shows emission maxima (in nm) vs w_s plot.

Emission maximum of 4-AP gradually shifts to longer wavelength with increase of w_s (**Figure 6.1b**). The emission spectrum displays a red-shift of ~30 nm from 445 nm at $w_s = 0$ to 475 nm at $w_s = 8$. Note that almost half of the peak shift (~15 nm) occurs in the lower w_s region (w_s = 0-1) but the other half occurs over a large w_s range (w_s 1-8) (inset of **Figure 6.1b**). The red-shifting of emission spectrum is quite common for aq-RM (AOT/water/*n*-heptane) with increase in water content; the emission maximum shifts from 445 nm (at w = 0) to 542 nm (at w = 30).[180] Note that the emission maximum, even at highest water content (w_0 = 30), is significantly shorter compared to the emission maximum in neat water (550 nm). However, the emission maximum of 4-AP in acetonitrile microemulsion becomes similar to neat acetonitrile (λ_{em}^{max} = 458 nm) at an intermediate w_s (~ 1) and further shifts to longer wavelength at higher w_s. Thus, the nature of the spectral shift in the case of acetonitrile microemulsion is quite different from that in the aqueous microemulsion.

Moreover, variation of emission intensity with w_s is found to be an anomalous; a gradual enhancement of emission intensity is also noticed in lower w_s region (w_s = 0 to 1) but the emission intensity gradually decreases at higher w_s (1-8). The quantum yield (QY) of 4-AP is slightly higher in acetonitrile (0.63) compared to dry AOT microemulsion (0.60).[112] Thus, the initial enhancement of emission intensity with the addition of acetonitrile can be obvious and 4-AP may be sensing more polar

environment. However, if the acetonitrile exposure of 4-AP is solely responsible for emission enhancement, then it should be observed throughout the w_s range (0-8). Thus, the unusual modulation of emission QY may be indicative of an abrupt change in the microenvironment around 4-AP after $w_s = 1$.

6.2.2. Red-edge excitation shift (REES) in acetonitrile/AOT/n-heptane microemulsion

In order to investigate the motional restriction of the solvent environment around the fluorophore, shift of the emission spectra are measured with variation of excitation wavelengths. A shift of emission maximum toward higher wavelengths, caused by a shift in the excitation wavelength toward the red edge of absorption band, is termed as red edge excitation shift (REES).[233-235] The effect is primarily observed for polar fluorophores in restricted environments when solvent relaxation time is comparable or longer than the lifetime of the fluorophore.[235] The amount of REES may indicate the level of motional restrictions imposed on the environment.

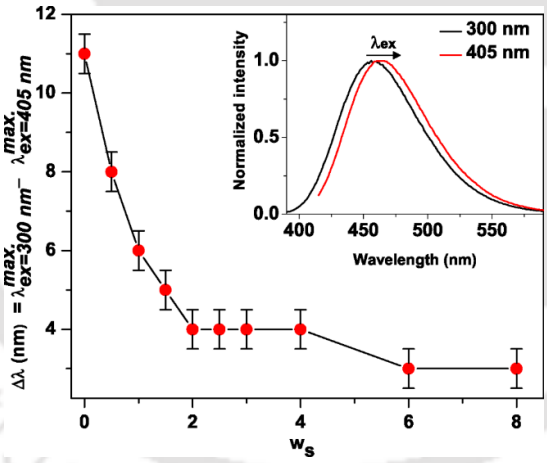

Figure 6.2: Variation of the red-edge excitation shift (REES, Δν in nm) of 4-AP inside acetonitrile/AOT/*n*-heptane microemulsion with gradual increment in the w_s. Inset shows emission spectra of 4-AP at various excitation wavelengths (λ_{ex}) at $w_s = 1$.

Figure 6.2 shows the variation of the magnitude of REES inside acetonitrile/AOT/*n*-heptane microemulsion at different w_s. The REES is represented as the difference between the two emission maxima corresponding to excitation at two extreme wavelengths (300 nm and 405 nm) of the absorption spectrum. In dry AOT microemulsion ($w_s = 0$), the REES values was quite significant (~11 nm) which implies

that 4-AP may resides in a very a restricted environment (see **Figure A.6.1** and **Table A.6.1** in *Appendix*). Upon gradual increment in acetonitrile concentration, REES steeply decreases to ~4 nm at w_s = 2 and thereafter, decreases only slightly. This suggests that the solvent relaxation becomes faster with increase of w_s.

6.2.3. Steady state anisotropy of 4-AP in the acetonitrile/AOT/n-heptane microemulsion

In order to guess the structural morphology of acetonitrile microemulsion, steady-state anisotropy (r_{ss}) at varying w_s content is measured (**Figure 6.3**). The anisotropy value at $w_s = 0$ is quite high and may be due to strong confinement of 4-AP within the AOT surfactant molecules. The r_{ss} value gradually decreases up to $w_s = 1.5$, thereafter it becomes unaltered upon further addition of acetonitrile. It seems that 4-AP faces molecular restrictions at lower w_s region and the restriction subsequently releases at higher w_s.

6.2.4. Fluorescence lifetime of 4-AP in acetonitrile/AOT/n-heptane microemulsion

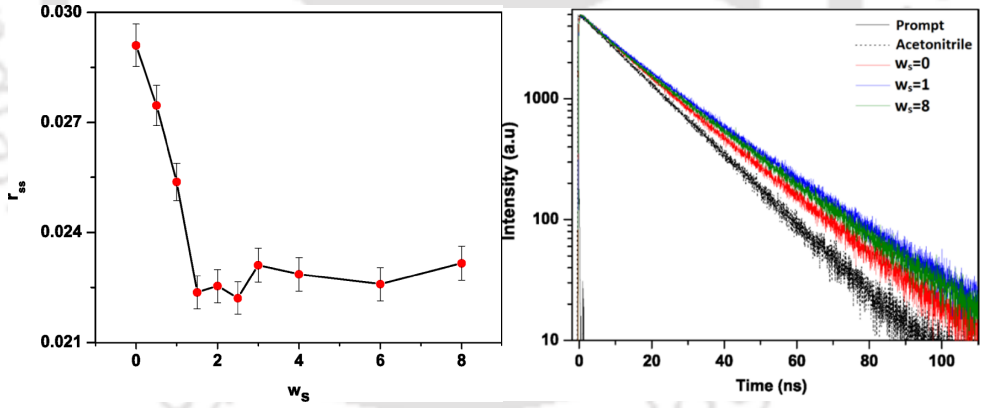

Figure 6.3: Steady state fluorescence anisotropy (left panel) of 4-AP inside acetonitrile/AOT/*n*-heptane microemulsion at various acetonitrile contents measured at the emission maxima (λ_{ex} = 360 nm). Fluorescence decays of 4-AP (right panel) inside acetonitrile/AOT/*n*-heptane microemulsion at various w_s measured at the corresponding emission maximum (λ_{ex} = 375 nm).

Fluorescence decays may provide valuable information about location of fluorescent inside a micro-heterogeneous medium. **Figure 6.3** displays fluorescence

decays of 4-AP inside acetonitrile/AOT/*n*-heptane microemulsion at some representative w_s and also the fluorescence decay in neat acetonitrile. All decays are fitted to bi-exponential function except in neat acetonitrile (single exponential) and the decays parameters are summarized in **Table 6.1**. It is evident from the **Figure 6.3** that the fluorescence decays are significantly slower in the microemulsion compared to that in bulk acetonitrile. The average fluorescence lifetime first gradually increases up to w_s = 1, remains almost unchanged between w_s = 1 to w_s = 2 and thereafter, gradually becomes faster with increase in w_s. The anomalous change in fluorescence lifetime may suggest a strong modulation of the microenvironment of 4-AP at an intermediate w_s.

Table 6.1: Fluorescence decay parameters and quantum yields of 4-AP inside acetonitrile/AOT/*n*-heptane microemulsion at various w_s.

System	ϕ	a_1	τ_1 (ns)	a_2	τ_2 (ns)	$^{\S}\langle\tau\rangle$ (ns)	χ^2
Microemulsion, w_s=0	0.61	0.23	9.2	0.77	18.1	16.1	1.09
Microemulsion, w_s=0.5	0.66	0.24	9.4	0.76	21.1	18.3	1.01
Microemulsion, w_s=1	0.65	0.29	12.7	0.71	21.1	18.7	1.10
Microemulsion, w_s=2	0.58	0.26	11.9	0.74	21.3	18.9	1.08
Microemulsion, w_s=4	0.53	0.21	9.2	0.79	20.5	18.2	1.10
Microemulsion, w_s= 8	0.48	0.21	7.3	0.79	19.6	17.0	1.02
Acetonitrile	0.63	1	14.8	-	-	14.8	1.06
40 mM AOT in acetonitrile	0.46	0.39	6.5	0.61	16.9	12.8	1.12

$^{\S}\langle\tau\rangle = a_1\tau_1 + a_2\tau_2$

6.2.5. Solvation dynamics of 4-AP inside the acetonitrile/AOT/n-heptane microemulsion

Fluorescence decays of 4-AP in acetonitrile/AOT/*n*-heptane microemulsion at a blue (λ_{em} = 410 nm) and a red (λ_{em} = 580 nm) wavelength are taken at various w_s values (see **Figure A.6.2** in *Appendix*). It is evident that the decays recorded at a blue-end of emission band are distinctly different from the decays recorded at red-end of the spectrum. A distinct rise component characteristic of solvation dynamics is clearly visible at the red-wavelength transients.

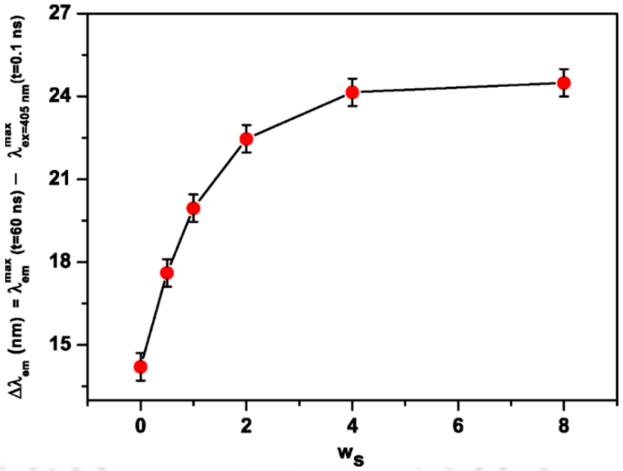

Figure 6.4: The relative shift in time resolved emission maxima $\Delta\lambda_{em}^{max} = \lambda_{em}^{max}\ (t = 60\ ns) - \lambda_{em}^{max}\ (t = 0.1\ ns)$ of probe 4-AP in acetonitrile/AOT/*n*-heptane microemulsion at different w_s.

Using spectral reconstruction protocol of Maroncelli and Fleming,[191] TRES at different times is constructed (see *Appendix* **Figure A.6.3**). TRES progressively shift to the longer wavelength upon increasing time without any appreciable change in the band shape. The dynamics Stokes shift is represented by $\Delta\lambda_{em}^{max}$ (nm) as a difference between the emission maximum of the TRES at a long time (60 ns) and initial time (0.1 ns).

$$\Delta\lambda_{em}^{max} = \lambda_{em}^{max}\ (t = 60\ ns) - \lambda_{em}^{max}\ (t = 0.1\ ns) \qquad \textbf{(6.1)}$$

The initial time at t = 0.1 ns (not at t = 0) is deliberately chosen due to limited resolution of our set up (IRF < 100 ps). $\Delta\lambda_{em}^{max}$ values at different w_s values are given in the **Figure 6.4**. The TRES of 4-AP in AOT/*n*-heptane system in the absence of acetonitrile also undergoes a relatively small red shift (~ 14 nm) with time. The result is consistent with the report of Correa and co-workers[180] and suggest that 4-AP undergoes significantly slower solvation dynamics. This also support existence of organized structure (RM) at this AOT concentration even without presence of any polar solvent ($w_s = 0$).

A steep increase of the $\Delta\lambda_{em}^{max}$ value is noticed with increase in w_s value up to $w_s = 2$ (**Figure 6.4**). The increase of the dynamics Stokes shift within same observation time window (0.1-60 ns) suggests that the solvent relaxation occurs in relatively faster time scales. At higher w_s (> 2) it is found that the change in the dynamic Stokes shift is

very less. This implies that the solvation dynamics occurs at similar times scales at high w_s regimes. Thus, the dynamics Stokes shift measurements clearly show existence of two different regions. The w_s dependent solvation dynamics behaviours in lower w_s region (w_s = 0-2) however at higher w_s region (w_s = 4-8) the dynamics Stokes shift remains unchanged which is observed by number of authors with different probes inside acetonitrile microemulsion. [86-87, 231] TRES shift thus corroborates with steady state anomalous spectral response of 4-AP and indicates modulation of acetonitrile microemulsion structure.

6.2.6. Spectral properties of 4-AP in acetonitrile in the presence of AOT

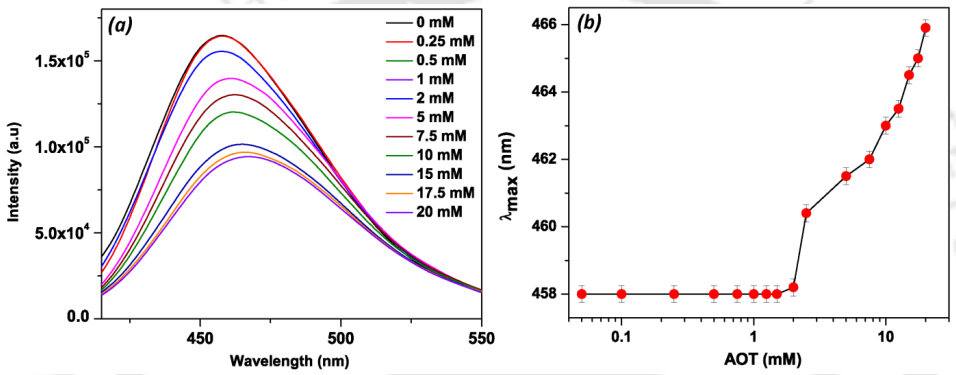

Figure 6.5: (a) Emission spectra and (b) emission maxima (λ_{max}) of 4-AP ($\lambda_{ex.}$=360 nm) in acetonitrile solvent as a function of AOT concentration.

The emission behavior of 4-AP in neat acetonitrile is also studied and in the presence of different concentration of AOT (**Figure 6.5**). The emission maximum of 4-AP in neat acetonitrile appears at 458 nm and emission spectrum remains invariant under different excitation wavelengths. The emission spectrum does not shift in the presence of AOT up to 2 mM but at higher concentration of AOT significant red shift of the emission maxima is observed (**Figure 6.5b).** Furthermore, at high AOT concentration, the emission maxima depend on the excitation wavelength and finite REES is observed. TRES measurement cannot detect any time dependent spectral shift in neat acetonitrile and in the presence of low concentration (< 2 mM) of AOT (see **Figure A.6.4** in *Appendix*). This suggest that the solvation dynamics in these systems are much faster than the time resolution of our set up. It is inferred that no organized structure exist in neat acetonitrile or in the presence of low concentration of AOT. However, at high concentration, significant time dependent spectral shift is observed

indicative of slow solvation dynamics. No sudden alteration (like that of 4-AP in acetonitrile microemulsion) in emission intensity was observed; QY gradually decreases with the increase of AOT concentration. Moreover, lifetime measurements also reveal that 4-AP strongly interact with AOT molecule, lifetime decreases from 14.9 ns to 12.9 ns when 40 mM AOT was added to neat acetonitrile (**Table 6.1**).

4-AP may resides at the AOT reverse micellar interface and interact with the head group of AOT molecule.[180] Moreover, Mukherjee et al. have shown that 4-AP emission maxima mostly depends on H-bond donation (α) or H-bond accepting capability (β).[236] They demonstrated this behavior by comparing λ_{max} of 4-AP in acetonitrile and in DMSO, 4-AP exhibits ~18 nm red shift from 458 nm in acetonitrile (α = 0.19 and β = 0.40) to 478 nm in DMSO (α = 0 and β = 0.76). Analogous to DMSO molecule, AOT head group contains two S=O linkages (**Scheme 6.1**) and hence, a superior H-bonding interaction is expected. This interaction may be responsible for the red-shifting of the λ_{max} of 4-AP. However further studies are needed to understand the nature of this interaction more deeply.

6.2.7. Dynamic light scattering studies of acetonitrile/AOT/n-heptane microemulsion

In order to get an idea whether acetonitrile RMs forms true RMs or not, DLS measurements are performed. Size of the dry AOT RMs is found to be ~ 3 nm which agrees well with the reported diameter of ~ 3.0±0.6.[237] **Figure 6.6** show the presence of two regimes. The hydrodynamic diameter gradually increases from ~ 3 nm at $w_s = 0$ to ~ 5.2 nm at $w_s = 1$ with the increase in acetonitrile content (See **Table A.6.2** in *Appendix*). Furthermore, in this regime ($w_s \leq 1$), size obtained from distribution fit and cumulant (z-average) fit agrees to each other. This implies that the system is not very polydispersed, which is also evident from low polydispersity index (PDI ~ 0.2-0.3). However, at higher w_s the system becomes very poly dispersed (PDI ~ 0.6-1) and hence, the results are less accurate in this regime (w_s 1-8). The difference in the scattering pattern in two regimes can be best viewed through the scattering autocorrelation function (See **Figure A.6.5** in *Appendix*) A lower w_s, the autocorrelation vanished after ~ 200 μs. However, for higher w_s, the autocorrelation persist over 100 s. More importantly, the drastic change of the autocorrelation pattern strongly suggests a dramatic change of the nature of the microemulsion.

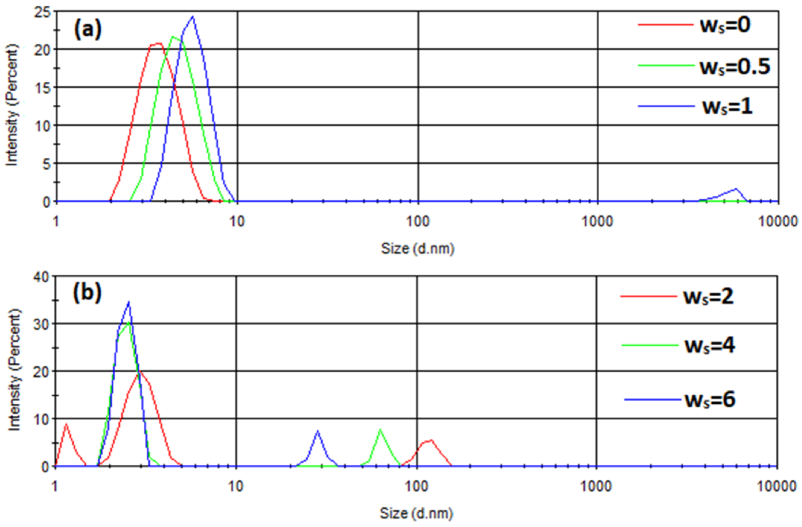

Figure 6.6: Hydrodynamic diameter of acetonitrile/AOT/*n*-heptane microemulsion at different w_s values obtained from dynamic light scattering (DLS) measurements.

6.3. DISCUSSION

The main objective is to characterize the controversial acetonitrile microemulsion systematically and to identify the parameters that lead to the formation of true RMs or BMC. The fluorophore 4-AP is insoluble in *n*-heptane, and hence may be completely absent from the continuous non-polar part of the microemulsion and can provide effective information about core formation (in the case of RMs) or channel formation (in the case of BMC) by added acetonitrile. Moreover, 4-AP is an excellent fluorophore as its quantum yield; emission maximum and lifetime are sensitive to environmental condition.[112, 180] The spectral properties of 4-AP modulates very differently at low and high w_s regimes. If it is assumed that the microemulsion changes its morphology from RM to BMC in between w_s = 1 and 2 (**Scheme 6.2**), satisfactory all the observations can be explain.

The emission spectrum shifts quite significantly with increase of the amount of acetonitrile in the lower w_s region (w_s = 0 -1) but the shift is much smaller at high w_s range (w_s 1-8). This is consistent with RM formation at low w_s and consequently, a dramatic change in polarity can be expected upon formation of acetonitrile pool. The emission maximum of 4-AP at w_s = 1 matches with neat acetonitrile. Note that it is argued that unlike water or alcohol, acetonitrile cannot involve in H-bonding with the headgroup of AOT.[89, 112] Thus, it may not be surprising that the emission maximum of

4-AP in RM becomes equal to neat acetonitrile. But it is more surprising that the emission maximum shifts to longer wavelength and even surpasses the emission maximum in neat acetonitrile at higher w_s. It is observed that the emission maximum of 4-AP in acetonitrile can shift to longer wavelength upon addition of a certain amount of AOT (> 2mM). In the polar solvent acetonitrile, the surfactant AOT molecules can form micelles and 4-AP may sense a polar environment at the micelle interface due to the presence of the polar head group. Note that a striking similarity is found between the emission maximum of 4-AP in acetonitrile solution in the presence of high AOT (30 mM) with the microemulsion at high w_s. Thus, there may be similarity between the polarity of the medium and the arrangement of AOT around 4-AP. This is only reasonable if BMC formation at higher w_s is assumed . In the BMC phase, some AOT molecules may reside in the acetonitrile nano-channels and may interact with 4-AP.

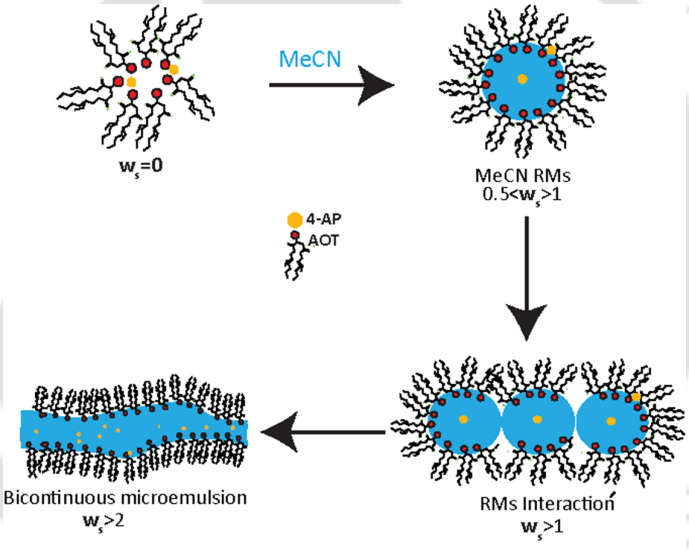

Scheme 6.2: Systematic conversation of acetonitrile/AOT/*n*-heptane reverse microemulsion to bi-continuous microemulsion with gradual addition acetonitrile.

The emission intensity and lifetime variation are also consistent with the RM to BMC transition. Fluorescence intensity and lifetime first increase with increase in w_s up to w_s = 1, and thereafter decreases. In the low w_s, because of RM formation, 4-AP may be distributed more into the acetonitrile core, which causes the enhancement of emission intensity. On the other hand, after BMC formation, interaction of AOT with 4-AP leads to decrease of lifetime and emission intensity.

Strong modulation of solvation response and the REES values within the low w_s regimes but much less variation occurring thereafter is also consistent with the RM to BMC transition. The organization of AOT rapidly changes in the RM region (low w_s) which may be responsible for progressively faster solvation dynamics (or lower dynamics Stokes shift). Inside the BMC phase, the confinement may be much less and may be invariant of acetonitrile constant. Low REES and faster solvation dynamics indicate formation of BMC in the high w_s range.

From DLS measurements, a moderate w_s dependent behavior at low w_s region (from ~ 3 nm at $w_s = 0$ to 5.20 nm at $w_s = 1$) is found. The swift swelling upon polar acetonitrile incorporation provides a clear evidence for the formation of reverse micellar type assemblies specifically at low w_s regimes. Conversely, with gradual increase in acetonitrile content, DLS measurements detect presence of large structures with high polydispersity (PDI~1.0). Thus, the presence of large microemulsion structures provide clear insights transition of spherical reverse micellar structure to non-continuous BMC type structure and transition occurred above $w_s = 1$. BMC structure is less organized compared to RM and hence a high PDI index is expected.

6.4. CONCLUSION

In this chapter, a novel systematic attempt is made to study structural transition of the controversial acetonitrile/AOT/n-heptane microemulsion by employing photophysical behaviors of the fluorophore 4-AP. A detailed analysis of steady-state and time-resolved emission spectroscopy results revealed that structure of the microemulsion depends on the amount of acetonitrile content. Structural characterization by DLS measurement validates the existence of two different w/o microemulsion structures and transition from RM to bi-continuous microemulsion type structure occurring at an intermediate $w_s \geq 1$. At lower acetonitrile content ($w_s < 1$), reverse micellar type droplets are formed and with further increase in the acetonitrile content ($w_s > 2$), reverse micellar droplets fuse among themselves owing to strong attractive interaction and transform into bi-continuous microemulsion (**Scheme 6.2**). Selective formation of RM and bi-continuous microemulsion type structures by simply varying polar content may open the door for synthesis of nanoparticles and will be discussed elaborately in subsequent chapter.

Chapter-7

Hydropobic Silver nanoparticle Synthesis inside Acetonitrile Microemulsion and Its Implication in Probing the Structural Transition of the Microemulsion[#]

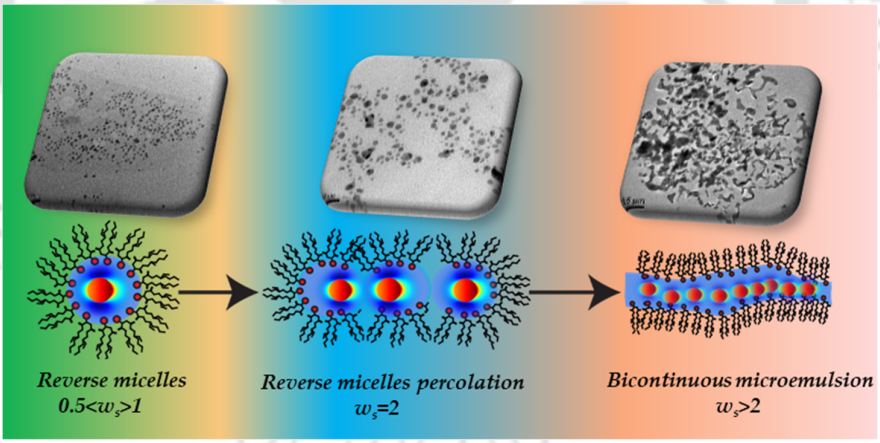

[#]This work has been published in *Colloids Surf. A* ***2019****, 574, 171-177.*

CHAPTER 7: HYDROPOBIC SILVER NANOPARTICLE SYNTHESIS INSIDE ACETONITRILE MICROEMULSION AND ITS IMPLICATION IN PROBING THE STRUCTURAL TRANSITION OF THE MICROEMULSION

7.1. INTRODUCTION

In the previous *Chapter,* we have shown that acetonitrile microemulsion undergo structural transition from RM to BMC after certain w_s. In this Chapter, a unique strategy is formulated to probe the structural transition by using microemulsion itself as a template for synthesis of silver colloids. Both silver nitrate and AA are insoluble in *n*-heptane phase and thus, Ag colloids formation occur solely inside the acetonitrile fraction and therefore, the structural morphology of the Ag colloids provides valuable information regarding the structure of the template where Ag colloids formation occur.

In principle, the acetonitrile/AOT/*n*-heptane microemulsion is a very suitable medium for AgNP synthesis. Silver nitrate has unusually high solubility (up to 9 M) in acetonitrile.[238] It is reported that acetonitrile forms coordination complex with silver (I) ion. [238-240] Moreover, AA has moderate solubility in acetonitrile and the solubility increases with increase in temperature.[241] Exploiting these convenient characteristics, here a very simple strategy is furnished for AgNPs synthesis inside the acetonitrile microemulsion at various w_s values. The polydispersity and optical quality of the AgNPs shows a robust correlation with microemulsion structure. Moreover, the synthesized AgNPs are found to be very stable, redispersable and can be easily coated on a glass plate.

7.2. SYNTHESIS OF HYDROPHOBIC SILVER NANOPARTICLES

Usually reducing agents are incorporated inside microemulsion as solution of the core-forming polar solvent (e.g. dissolve in water in the case of aqueous microemulsion). However, AA exhibits moderate solubility in acetonitrile. Thus, if AA is incorporated as a solution of acetonitrile, the required concentration of AA in the stock solution would exceed its solubility limit. To avoid this, different route is taken. First, AA (5 mM) solution of acetonitrile is evaporated so that solid AA remained in the container. Then, dissolution of the AA inside AOT/*n*-heptane solution is followed through absorption spectroscopy (see **Figure A.7.1** in *Appendix*). AA has a strong absorption maximum at 262 nm and the absorbance at this wavelength is developed linearly with increase in AA concentration indicating that RM is dissolved completely

into the AOT containing non-polar phase. The extinction coefficient of AA in the system is found to be 13.4 ± 0.4 × 10^3 M^{-1} cm^{-1}. As AA is not soluble in *n*-heptane, it is inferred that AA may bind to AOT possibly through H-bonding. After AA solubilisation, $AgNO_3$ solution is incorporated as acetonitrile solution. UV-Vis spectrum is recorded when no further change in absorption is noted.

2.5 mL 90 mM AOT solution is prepared in *n*-heptane. A stock solution of 5 mM AA is prepared in acetonitrile by mild heating (50 °C) and stirring. Required amount of this stock solution is spreads into a glass vial and dried gently until all the solvent evaporates. To the same vial, the AOT/n-heptane solution added and stirred at 1000 rpm for 3 hours for complete dissolution of AA into the AOT/heptane solution. The overall AA concentrations are 0, 0.05, 0.10, 0.2, 0.3 mM, respectively, in different sets. To this AA/AOT/heptane solution, $AgNO_3$ is added as an acetonitrile solution. The concentration of $AgNO_3$ in the acetonitrile solution is adjusted so that a fixed overall concentration of Ag^+ (0.3 mM) is maintained at all w_s's. After addition of $AgNO_3$, the colourless solution changes to deep yellow with elapse of ~ 2 hours' time indicating formation of AgNPs.

7.3. RESULTS

7.3.1. Extinction spectra of AgNPs formed inside of microemulsion at different w_s

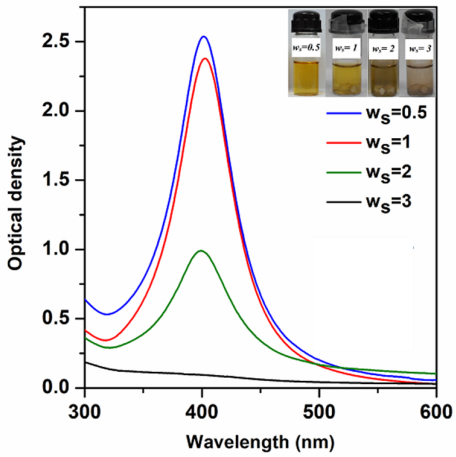

Figure 7.1: The UV-Vis spectra of Ag colloids formed in the acetonitrile/AOT/*n*-heptane microemulsions at w_s = 0.5, 1, 2 and 3. The concentration of $AgNO_3$ and AA

is fixed at 0.3 mM and 0.20 mM, respectively. Photographs of each solution are given in the inset.

Figure 7.1 shows the SPR band of Ag colloids synthesized at various w_s values (0.5-3) for a fixed AA concentration of 0.20 mM. Optimum concentration of the AA is determined by varying different concentrations of AA (see **Figure A.7.2** in *Appendix*). The details of the SPR maxima and FWHM (full width at half maxima) of the SPR bands at different AA concentrations and at various w_s values are provided in *Appendix* **Table A.7.1**. From **Figure 7.1**, it is evident that optical quality gradually depletes with increase in the w_s values; the maximum absorbance (A_{max}) decreases from at 2.5 (at w_s = 0.5) to 0.90 (at w_s = 2) with a concomitant increase of the FWHM from 62 nm to 71 nm. Surprisingly, SPR peak almost vanishes at w_s = 3; the solution becomes almost colorless (inset of **Figure 7.1**). SPR band of AgNPs attained at w_s = 0.5 and 1 are quite similar in optical quality, however, in the case of w_s =2, the SPR band contains an extended tail up to 600 nm. This may indicate coexistence of large nanoparticles in addition to un-associated nanoparticles. Note that in the previous *Chapter* change in microemulsion phase from RM to BMC is predicted. These two phases may exert very different templating effect for the nanoparticle formation.

7.3.2 Variation of hydrodynamic diameter of AgNPs with w_s value of microemulsion

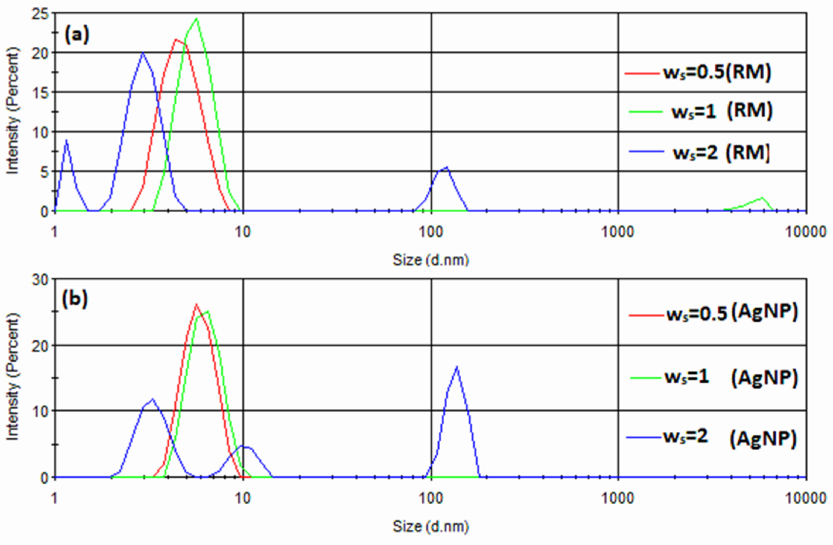

Figure 7.2: Hydrodynamic diameter of acetonitrile/AOT/*n*-heptane microemulsion at different w_s values obtained from DLS measurements in absence of silver nanoparticles

(a) and in presence of AgNP (b). The concentration of $AgNO_3$ and AA is fixed at 0.3 mM and 0.20 mM, respectively. Note that the DLS spectra in absence of AgNP is taken from *Chapter 6*.

In order to know the effect of incorporation of Ag colloids on the hydrodynamic diameters of the acetonitrile microemulsion, DLS measurements on Ag colloids are performed (**Figure 7.2**). It is apparent that at lower w_s region, Ag colloids containing microemulsion exhibit unimodal distribution with hydrodynamic diameter ~ 5.8 nm (w_s = 0.5) and ~ 6.4 nm (w_s = 1), along with low PDI ~ 0.2 (see **Table A.7.2** in *Appendix*). However, at higher w_s regimes, multimodal distribution of the hydrodynamic diameter with large PDI value (~ 0.4-0.6) is seen, hence, the results are less accurate in this region. The obtained hydrodynamic diameters of AgNPs microemulsion at lower w_s region larger (~ 5.8 nm and ~ 6.4 nm at w_s = 0.5 and w_s = 1 respectively) than of hydrodynamic diameters pure microemulsion (~ 4.7 nm and ~ 5.6 nm at w_s = 0.5 and w_s = 1 respectively).[242] Thus, the swelling of RM upon nanoparticle formation is evident at lower acetonitrile content. Therefore, at lower acetonitrile content the microemulsion may pre-exist as reverse micellar type aggregates and such aggregates serves as flexible template for nanoparticle formation. This trend clearly corroborates with our photophysical probing in *Chapter 6*, at lower acetonitrile content ($w_s \leq 1$); reverse micellar type droplets are formed. These droplets start percolation at $w_s > 1$ which may be the reason for multimodal distribution along with high PDI.

7.3.3 Correlation of AgNPs size and distribution w_s value of microemulsion

To understand effect of w_s on the final size, shape and distribution of synthesized Ag colloids, TEM measurement at w_s = 0.5, 1, 2 and 3 are performed (**Figure 7.3**). TEM micrographs reveal that Ag colloids particles are exclusively spherical and size distributions quite narrow at w_s = 0.5 and 1, and at w_s = 2 the majority of the particles deviated from spherical shape and aggregation is clearly visible in the system. Surprisingly, at w_s = 3 presence of spherical Ag colloids is very scare rather channel-like large Ag nanostructures are prominent. The diameter of AgNPs are found to be 5.6 ± 1.9 nm, 6.8 ± 3.10 nm and 9.5 ± 4.0 nm at w_s = 0.5, 1 and 2, respectively. Enlargement of diameter is nicely correlated with SPR spectra where a gradual depletion AgNPs SPR with w_s values is noticed. Moreover, the observed diameter

nicely correlated with hydrodynamic diameter of acetonitrile microemulsion obtained from DLS measurement especially for $w_s = 0.5$ and 1 (see **Table A.7.2** in *Appendix*).

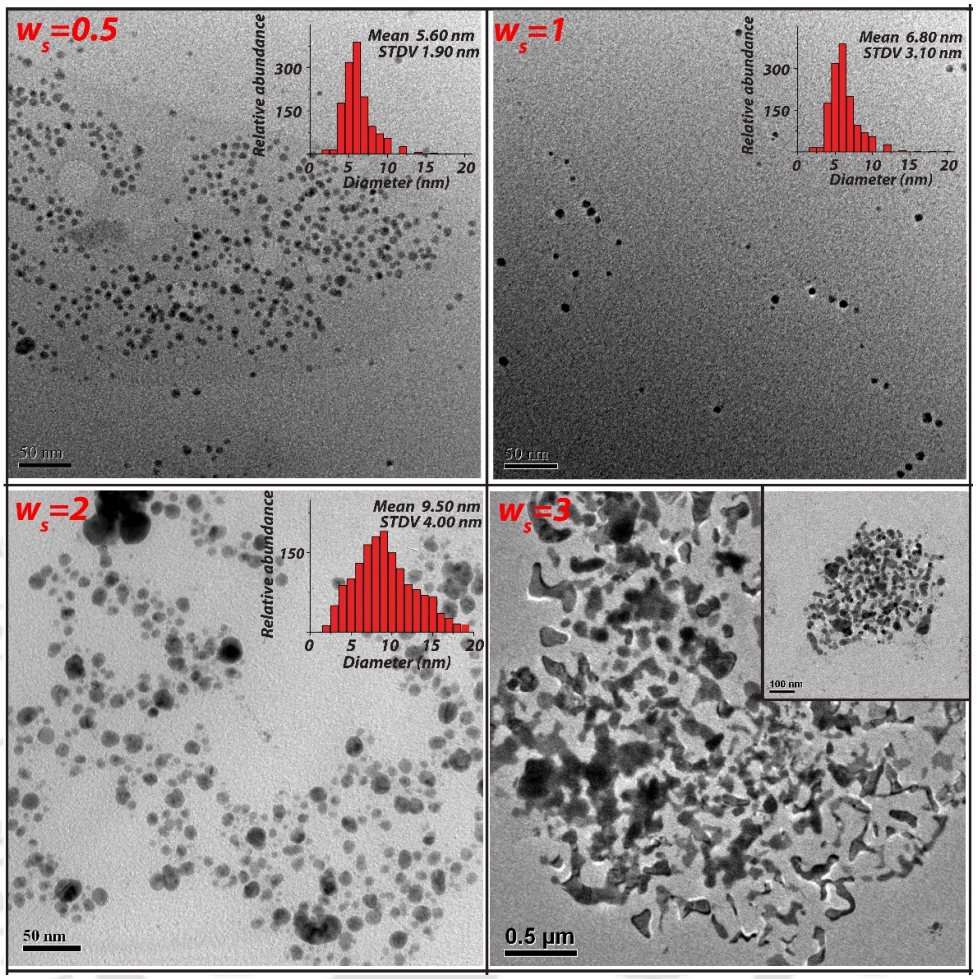

Figure 7.3: TEM images and size distribution histograms of Ag colloids synthesized by AA reduction at w_s = 0.5, 1, 2 and 3 respectively. The overall concentrations of $AgNO_3$ and AA are 0.30 and 0.20 mM, respectively. Histograms are generated by excluding larger AgNP aggregates and TEM micrograph at $w_s = 3$ are represented in lower resolution (500 nm scale bar).

The details inspection of several TEM pictures at w_s =2 shows that large aggregated particles size around 20 to 30 nm are present in all portion of copper grids, it seems that several AgNPs fuses among themselves to produce large AgNP aggregates. Abrupt change in the AgNPs size and shape along with polydisperisty at w_s = 2 may be due to reverse micellar percolation phenomena. Since RMs is spherical in shape and percolation phenomena may distort spherical shape and produce various

labile structure, which may act as template of AgNPs. Thus, different types of templates may produce Ag colloids of various morphologies and hence, high degree of polydispersity may be observed. On other hand, presence of channel-like Ag nanostructures may be due to presence of BMC structures that contains numerous nanochannels.[100, 230]

7.3.4 Properties of AgNPs synthesized inside acetonitrile/AOT/n-heptane microemulsion

7.3.4.1 Superior optical quality compare to all other methods based on AOT microemulsion

To the best of our knowledge, the optical quality of the AgNPs synthesized inside acetonitrile/AOT/*n*-heptane microemulsion found to be much superior than previously reported other aqueous and non-aqueous AOT microemulsion routes for details see Appendix (**Table A.1.1** and **Figure A.7.3**). Moreover, the optical quality is even superior than our previously reported aqueous route (*Chapter* 3). The optical quality of the SPR band is very important, as it is directly correlated with size and polydispersity Ag colloids.

7.3.4.2 Superior thermal stability and re-dispersibility

It is reported that with temperature, a substantial change in both the optical and structural properties AgNPs are noticed (both for AOT micelles and RMs route).[243-244] Thus, in order to check thermal stability of AgNPs, the temperature of the suspension is gradually varied using a peltier attached inside UV-visible spectrophotometer (see **Figure A.7.4** in *Appendix*). The temperature adjustment can be easily controlled from outside without disturbing the AgNPs solution. The successive absorption spectra are taken after equilibrating the solution for 20 minutes. The main advantage of this approach is that even a minute change in SPR with temperature can be easily detected. No appreciable change in SPR peak is noticed when the system *in situ* temperature gradually altered. Invariance in the optical properties gives clear indication of invariance in the size and morphology of AgNPs.

To check the stability of the AgNPs and its usability in different medium, solvents (heptane and acetonitrile) are evaporated by drying the AgNPs solution with hot air and re-dispersed it in equal volume of *n*-heptane. The re-dispersed solution of AgNPs in *n*-heptane at w_s = 0.5 shows negligible change in UV-Visible spectrum

compared to the as-synthesized nanoparticle (**Figure 7.4**). The plasmonic peak at ~ 402 nm remains invariant before and after air drying; only a very little change in absorption maxima is observed. The property that the AgNPs remains stable under dry conditions can be exploited in easy storage and transport of the nano-materials for future use.

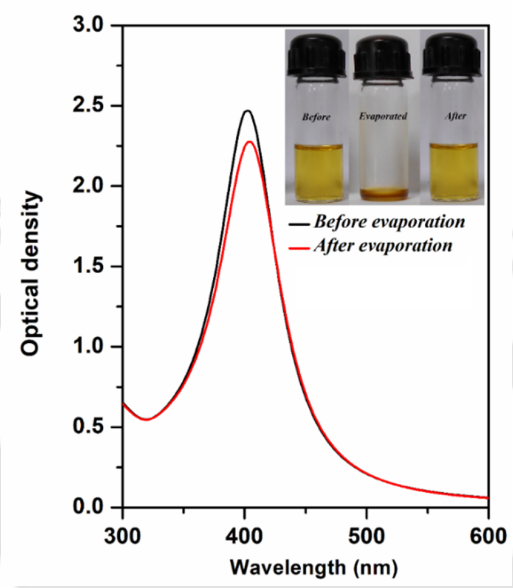

Figure 7.4: Comparison of UV-Vis spectra of as prepared AgNPs formed in the acetonitrile/AOT/*n*-heptane microemulsions at $w_s = 0.5$ and after evaporation followed by re-dispersing in n-heptane. Photographs of as prepared, evaporated and re-dispersed solutions are given in the inset.

7.4. DISCUSSION

The main objective is to see whether there is any correlation between initial microemulsion structure (template structure) and the properties (optical or structural) of the synthesized MNPs. In previous *Chapter*, it is found that acetonitrile microemulsion may undergo a structural transformation after a certain w_s. As both the $AgNO_3$ (precursor) and the reducing agent (AA) are insoluble in continuous non-polar phase (*n*-heptane),[97, 109, 241] and thus, AgNP formation occur exclusively inside the acetonitrile confined within the organized microemulsion structure and therefore, the structural morphology of the AgNPs may provide valuable information regarding the structure of the template where AgNPs formation occur. The transformation of one type of structural assemblies (spherical RMs) to another type of assemblies (nanochannel like BMC) may reflect in the structure and shape of AgNPs.

Synthesis of AgNPs inside non-aqueous acetonitrile microemulsion is possible as $AgNO_3$ exhibits unusually high solubility in acetonitrile and AA can be extracted into interfacial region of dry RMs (**Scheme 7.1**). Note that AA is not very effective reducing agent for room temperature synthesis of AgNPs in aqueous solution,[196-197, 245] however, through this and our earlier studies,[18, 57] it is shown that AA is indeed a very handy reducing agent for AgNP synthesis inside both aqueous and non-aqueous microemulsions.

The sequence of nanoparticle formation at different types of microemulsion types can be understood as follows (**Scheme 7.1**). First, RM is taken up within the AOT layer at the interface in the absence of any polar solvent. This is evident as AA can be dissolved directly into the AOT/n-heptane mixture in the absence of acetonitrile. Since AA is also miscible in acetonitrile, it may also distribute within the acetonitrile core. However, since the amount of AA used here is quite high, it may reside mostly inside the AOT layer. Then, silver nitrate is fed into the system as a solution in acetonitrile. The silver ion may reside at the negatively charged interface due to favorable electrostatic interaction. Subsequently, reduction of silver ion may produce neutral silver atoms or silver clusters (probably Ag_4^+) that finally grow into nanoparticles of specific size.[18, 109] The reduction may be favored over homogeneous medium because of the spatial proximity of the silver ion and reducing agent inside the AOT interface.

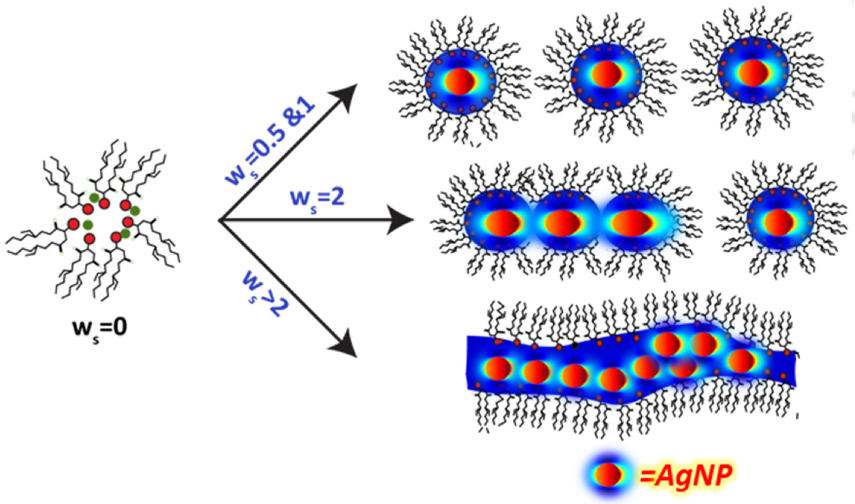

Scheme 7.1: Template-directed expected growth of silver nanoparticles within acetonitrile/AOT/*n*-heptane microemulsion at different w_s.

Droplet percolation and droplet coalescence/de-coalescence are assumed to be two major processes by which structural transition of RMs may takes place.[77, 108, 131] In previous *Chapter*, it is suggested that acetonitrile microemulsion percolation may start above $w_s = 1$ and spherical RMs may convert into BMC-type structures above $w_s = 2$. One of the main indications of the presences RMs in a microemulsion, is that hydrodynamic diameter must increase with increase of the core-forming polar solvent.[77, 180, 220] Since, AgNP formation occurs inside the confined polar core and hence, the size of the AgNPs may also increase with the polar solvent content (w_s). Thus, the size of the AgNPs should increase with increase in acetonitrile content which is observed for $w_s = 0.5$ and 1. Moreover, the AgNPs at $w_s = 0.5$ and 1 are found to be exclusively spherical in shape which further support existence of spherical reverse micellar structure at $w_s = 0.5$ and 1. Presence of highly monodisperse spherical AgNPs may result in superior optical quality SPR band. Note that the position and width of the SPR band AgNPs depends strongly on size, shape, and dielectric constant of the medium.

On other hand, due percolation phenomena, RMs fuse among themselves and hence a variety of labile arrangements of RMs may be generated.[77, 131] At $w_s = 2$, formation of AgNPs occur in these labile structures and therefore, polydispersed AgNPs are formed. Furthermore, the presence of polydispersed AgNPs may result in depletion of SPR band and an extended tail. Thus, optical quality and stability of the AgNPs provides evidence of presence of RMs type structure in these systems.[17, 245-246]

The main problem may have associated with synthesis in BMC region is stability of the colloidal dispersion, when Sarkar and co-workers tried to synthesize above $w_s > 5$ (may be BMC region for MeOH) the solution trends to become opaque and AgNPs synthesis not at all possible.[174] Surprisingly, similar characteristics is also found, at $w_s = 3$ the solution completely losses its bright yellow color (**Figure 7.1**). However, the TEM image clearly reveals that existence of interconnected channels silver nano-structures (**Figure 7.3**). Lopez and coworkers also found similar type of Ag nanostructures when they tried to synthesis AgNP synthesis inside BMC made of AOT/SDS mixed surfactant.[247] Presence of Ag nanostructures can only be explained on the basis of channel-forming ability of BMC, as the name bi-continuous suggest both the oil and water is in continuous phase inform of nano channels.[100, 134, 248]

7.5. CONCLUSION

In conclusion, a new way to characterize structures of the non-aqueous acetonitrile/AOT/*n*-heptane microemulsion is demonstrated by synthesizing Ag colloids *in situ*. The synthesized Ag colloids have direct correlation with the structure of the microemulsion template; at low w_s = 0.5 and 1, superior optical quality and spherically monodisperse AgNPs (size ~ 5-6 nm) are obtained which suggests the template is reverse micellar type. On other hand, at high at w_s = 2, polydispersed AgNPs (size ≥10 nm) with poor optical quality are observed. The polydispersity at w_s = 2 is explained on the basis of percolation phenomena of acetonitrile droplets above w_s > 1.[242] Moreover, above w_s = 2 SPR peak completely vanishes and channel like large Ag nanostructures are noticed. The presence of Ag nanostructures explained based on channel forming ability of acetonitrile/AOT/n-*h*eptane microemulsion. Thus, this templet -directed Ag colloids synthesis is directly correlated with *Chapter* 6 and provides further evidences of structural transformation of acetonitrile/AOT/*n*-heptane microemulsion. Additionally, the synthesized AgNPs are very stable at dry conditions and have superior optical quality compared to all other AOT microemulsion based synthesis (both aqueous and non-aqueous).

SUMMARY AND FUTURE OUTLOOK

In the present thesis, a facile synthesis method has been developed to obtain high optical quality AgNPs inside aqueous and non-aqueous (acetonitrile) microemulsion. This has been achieved by using a mild reducing agent ascorbic acid (AA). Usually, AA is considered too weak to reduce $AgNO_3$ solution at room temperature. However here, for the first time, it has been shown that, AA can reduce $AgNO_3$ solution inside AOT microemulsion at room temperature. The synthesized AgNPs exhibits superior optical quality compared to other reports based on AOT microemulsion. Formation of the AgNPs inside RMs core perturbed structural organization of the reverse micellar interface and perturbation was probed with molecular probe C343. It has been found that the interfacial region of the RMs become more hydrated, less packed upon nanoparticle formation particularly at low w_0 region. The usefulness of superior optical quality AgNPs were demonstrated in probing plasmon-fluorophore interaction inside natural cavity of RMs. The fluorophores, fluorescein and safranine O were studied and it had been found that fluorescein undergone a strong coupling with AgNPs whereas for safranine no such effects were noticed. Dissimilar effect was explained on the basis of spectral overlap and spatial distribution of fluorophores with respect to AgNPs. Thereafter, synthesis of AgNPs inside non-aqueous acetonitrile microemulsion was attempted, as acetonitrile microemulsion provides suitable medium for AgNPs synthesis. However, the structure acetonitrile microemulsion remains debated in literature and hence the structure microemulsion at different w_s was studied using a solvatochromic probe 4-AP. It has been found that structure of microemulsion depends on w_s values; RMs type droplet formed at $w_s < 1$ whereas bi-continuous microemulsion were formed at $w_s > 2$. Finally, Ag colloids were synthesized inside acetonitrile microemulsion at different w_s. It has been found that optical properties and morphologies of Ag colloids depends on w_s values; at low w_s =0.5 and 1, superior optical quality and spherically monodisperse AgNPs are obtained which suggests the template is reverse micellar type. Above $w_s = 2$ SPR peak completely vanishes and channel like large Ag nanostructures formed suggests the template is bi-continuous type. Thus, the characteristics of Ag colloids (i.e. size distribution and optical quality) provide valuable information about structure of the microemulsion and provides further evidences of structural transformation of acetonitrile microemulsion.

The presented synthesis of AgNPs inside microemulsion will bring a new paradigm towards understanding the role of various mild reducing agents on synthesis of nanoparticles with high optical qualities. As biocompatible AA (vitamin C) is used in AgNPs formation and therefore the synthesized AgNPs may also have high degree of biocompatibility. Hence may have tremendous potential in biological and clinical applications. Microemulsion is a multicomponent system and hence various metal precursors, reducing agents, and their combination can be used in nanoparticle formation. Thus, it is expected to open new avenue towards synthesis of various other metal nanoparticles, bimetallic nanoparticles, metal oxides and sulphide nanoparticles etc. It will be very interesting to see the optical properties of other metal nanoparticles especially copper and gold synthesized by this route. The knowledge of perturbation of interfacial layers of microemulsion upon nanoparticle formation will certainly help to understand growth process of various types of nanoparticles inside a microemulsion. Here an example was presented to show the effectiveness of microemulsion confinement to explore plasmon-fluorophore interaction and this concept can be extended over a range of fluorophores and nanoparticles. Fluorescein and safranine nano-composites may have useful application in cell imaging and sensing. Here usefulness of ultrasensitive probe 4-AP was presented in probing structure of non-aqueous acetonitrile microemulsion and this concept can be extended to various other types of aqueous and non-aqueous microemulsions. Numerous organic reactions occurred inside acetonitrile/heptane medium and synthesis of AgNPs in these medium will certainly be useful from catalysis point of view. Here application of superior optical quality AgNPs was demonstrated in probing microemulsion structure and this concept can be extended in probing the structure of other non-aqueous microemulsions.

APPENDIX

For Chapter 1

Table A.1.1: Optical properties, particle sizes and various control parameters of silver nanoparticle synthesis via AOT microemulsion method.

Sl No	Microemulsion system	Ag precursor	Reducing agent	Varying parameter	w_0	SPR peak (nm)	FWHM (nm)	Avg. Size in nm
1	Water/AOT/dodecane[169-170]	$AgNO_3$	$N_2H_4{\cdot}H_2O$	C_m, C_{red} and w_0	2.5,7.5 &15	425 (C_m=0.2 mM) 415 (C_m=0.4 mM) 440 (C_m=0.8 mM)	-	1.52 (w_0=2.5) 3.39 (w_0=7.5) 4.98 (w_0=7.5)
2	Water/AOT/dodecane[177]	$AgNO_3$	$N_2H_4{\cdot}H_2O$	Time, C_{AOT}	7.5	420	-	3.9 (C_{AOT}=0.2 M), 1.6 (C_{AOT}=0.4 M)
3	Water/AOT/cyclohexane[175]	$AgNO_3$	$NaBH_4$	w_0,	5,8	-	-	5.5 (DLS, at w_0=5), 54.5 (DLS, at w_0=8)
4	Water/AOT/isooctane[175]	$AgNO_3$	$NaBH_4$	w_0, molar ratio of reagents	5,6.3, 8	416 (w_0=5), 420 (w_0=6.3), 425 (w_0=8)	-	0.7 (DLS, at w_0=5), 4.9 (DLS, at w_0=6.3), 60.0 (DLS, at w_0=8), 0.7 (w_0=5), 4.9 (w_0=6.3)
5	Water/AOT/isooctane and $C_{12}E_4$ as co-surfactant[171]	$AgNO_3$	KBH_4	w_0, pressure, C_m, C_{red}	5,10, 15	407, (λ_{abs} as function of Ag concentration when [Ag]≤0.030 mg mL^{-1})	~150-200	2-5 (w_0=5), 3-8 (w_0=15), Smaller particle at higher C_{red}
6	Water/Ag-AOT and AOT mixture/isooctane[109]	Ag-AOT $AgNO_3$	$NaBH_4$ in mM (**A**) $N_2H_4{\cdot}H_2O$ in mM (**B**)	w_0, C_m, C_{red}, kinetic study.	2,5,7.5, 10,12.5	(1) 421 (w_0=2, 0.25 mM **A**), (2) 419 (w_0=5, 0.25 mM **A**), (3) 406 (w_0=7.5, 0.25 mM **A**), (3i) 414 (w_0=7.5, 0.10 mM **A**), (3ii) 430 (w_0=7.5, 0.010 mM **A**), (4) 400 (w_0=15, 0.25 mM **A**), (4i) 409 (w_0=15, 0.10 mM **A**), (5) 406 (w_0=7.5, 68 mM **B**), (5i) 413(w_0=7.5, 6.80 mM **B**), (5ii) 420(w_0=7.5, 0.68 mM **B**), (5iii) 422(w_0=7.5, 0.1 mM **B**), (6) 406 (w_0=7.5, isooctane), (6i) 415 (w_0=7.5, cyclohexane),	(1)170, (2) 138 (3) 82 (3i)108 (3ii) 200 (4) 75 (4i) 90 (5) 80 (5i) 87 (5ii) 120 (5iii) 160 (6) 82	(2) 2.7, (3) 5.5 (3i) 4.5, (4) 7.0, (4i) 6.0, (5) 7.5, (5i) 6.5, (5ii) 5.0, (5iii) 4.5, (6) 5.5, (6i) 6.7
7	Water/AOT/heptane[172]	$AgNO_3$	$NaBH_4$	Continuous phase, C_{red}, effect of surfactant	10	(1) 406 (decane), (1i) 414 (heptane), (1ii) 422 (cyclohexane). (2) 414 (heptane), (2i)416 (heptane+SDS), (2ii) 411 (heptane+DTAB),(2iii) heptane+NP-5). (3) 414 (heptane),		(1) 6, (1i) 22.4, (1ii) 5.4, (2) 22.4, (2i) 24.5, (2ii) 18.40, (2iii) 7.14, (3) 22.4, (3i) 8.8, (3ii) 7.6

						(3i) 406 (heptane+benzyl alcohol), (3ii) 424 (heptane+toluene)		
8	Water/AOT/n-octane or n heptane[173]	$AgNO_3$	Quercetin	C_m, time, C_{red},	3.7	~400-410	-	1-1.5 (calculated)
9	Water/AOT/n-heptane[147]	$AgNO_3$	Glucose	-	4	-	-	3.5
10	Water/AOT/n-heptane[168]	$AgNO_3$	Glucose (**A**), $NaBH_4$ (**B**)	w_0, C_{red}	4,8	-	-	3.6 (w_0=4 by **A**), 3.3 (w_0=8 by **A**). ~7 (w_0=4 & 8 by **B**).
11	Ethylene glycol/AOT/iso octane[176]	$AgNO_3$	Glucose	w_0	1 &2	420	-	~3.6 (1 &2)
12	Methanol/ AOT/n-heptane[174]	$AgNO_3$	$NaBH_4$	w_0, time	2-5	436 (w_0=2), 421 (w_0=3,4 & 5).	-	4.3 (w_0=2 @40 hour), 3.8 (w_0=4@40 hour), 8.2 (w_0=2 @16 days), 4.8 (w_0=4@16 hour).

w_0= [polar]/[AOT], C_m=concentration of $AgNO_3$, C_{red}= concentration of reducing agent, FWHM=Full width at half maxima.

For Chapter 3

Table A.3.1: Summary of optical characteristics of SPR band of the AgNP prepared in water/AOT/n-heptane RMs under different conditions. Overall concentrations [$AgNO_3$] = 0.3 mM; [AOT]= 90 mM.

w_0	Reducing agent	[Red](mM)	λ_{max}(nm)	FWHM(nm)
2	AA	0.01	405	178*
		0.05	405	146*
		0.10	410	138*
		0.20	411	135*
6	AA	0.01	408	102
		0.05	402	86
		0.10	402	102
		0.20	402	75
10	AA	0.01	410	118
		0.05	408	103
		0.10	403	97
		0.20	402	103
6	$NaBH_4$	0.05	-	-
		0.10	-	-
		0.30	408	174*
6	$N_2H_4.H_2O$	0.05	406	142*
		0.10	403	150*
		0.30	403	-

*FWHM is calculated at half-width in the higher wavelength side and then multiply by 2. The symmetric nature of the SPR band is assumed in this calculation and used as a estimate where true FWHM was not possible to determine.

Table A.3.2: Hydrodynamic diameter obtained from dynamic light scattering (DLS) measurements for pure RMs and AgNP containing RMs at w_0=2, 6 and 10.

System	W_0	Hydrodynamic diameter	TEM measurement
RM	2	4.8	-
AgNP-RM	2	5.3	5.7
RM	6	5.9	-
AgNP-RM	6	6.1	6.1
RM	10	8.8	-
AgNP-RM	10	8.9	8.3

For Chapter 4

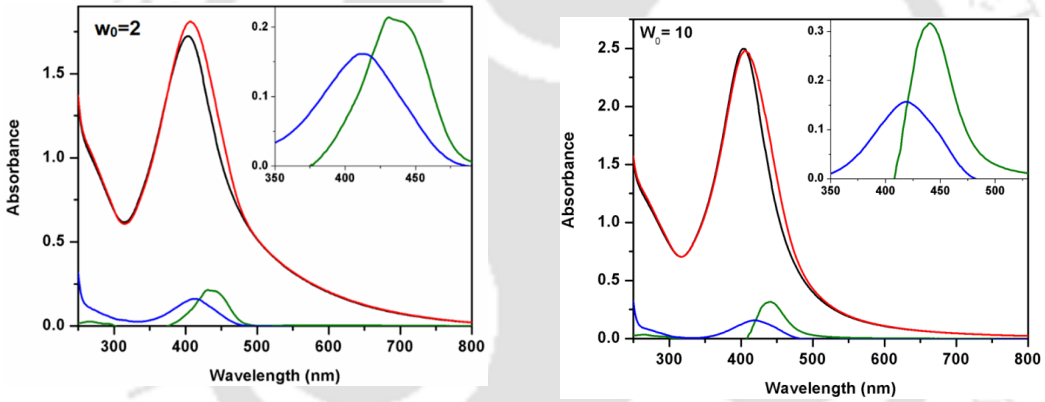

Figure A.4.1: The UV-visible spectra of water/AOT/n-heptane reverse micellar system at w_0 = 2 and 10 comprising (a) AgNPs only (black), (b) C343 and AgNPs (red), (c) C343 only (blue). The green curve represents the difference spectrum [(b)-(c)] (green). The absorption spectrum of C343 in the pure RMs and the difference spectrum are compared in a magnified scale in the inset.

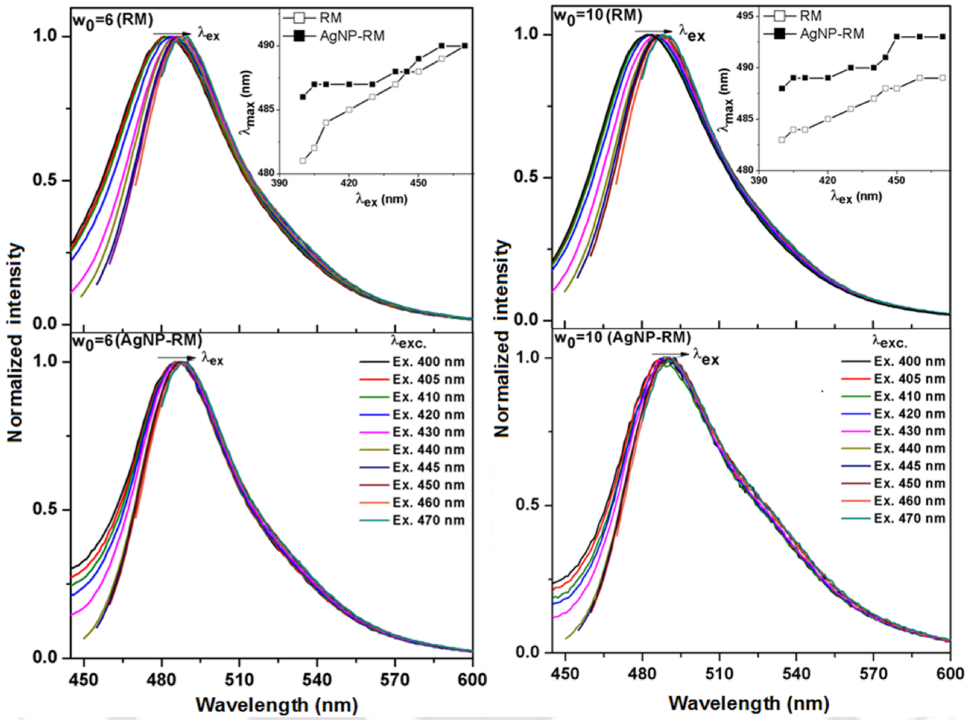

Figure A.4.2: Plot of emission maxima against excitation wavelength for the pure and the AgNP containing RMs at w_0= 6, 10. The total shift of the emission maxima (i.e. REES) in AgNP containing system is much lower compared to the pure RMs.

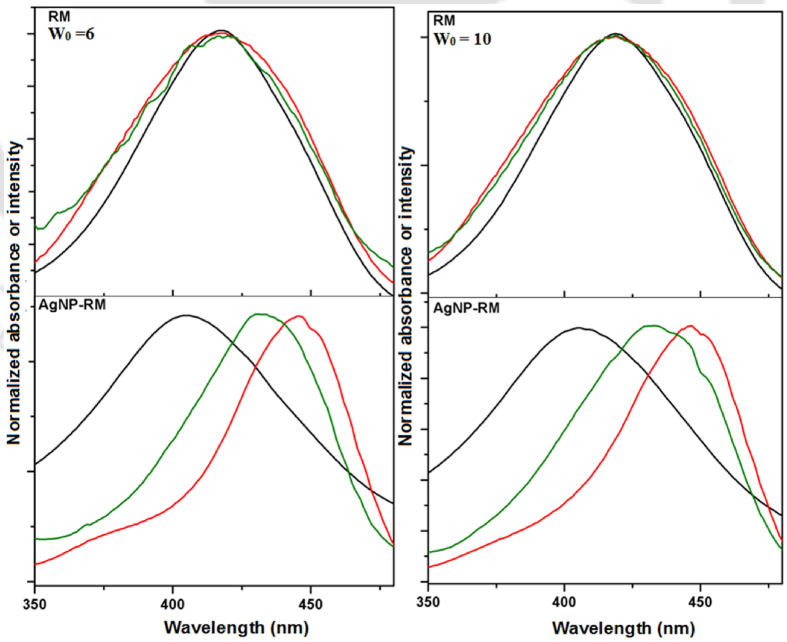

Figure A.4.3: Absorption spectrum (black), excitation spectra using a standard 10 mm cuvette (red, green) and in a glass capillary tube (0.8 mm internal diameter) (green) of C343 in pure RMs (top panel) and in AgNP containing RMs at (bottom panel). The excitation spectra are recorded at an emission wavelength of 490 nm.

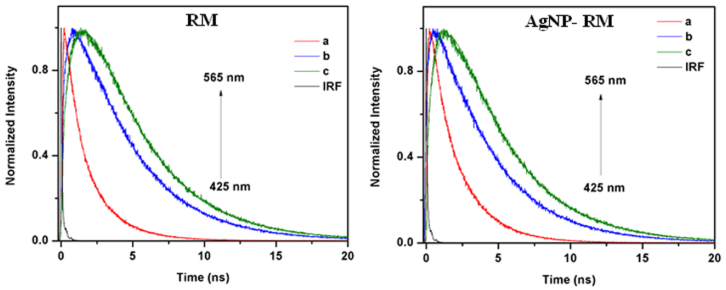

Figure A.4.4: Fluorescence decays of C343 water/AOT/n-heptane reverse micellar system at w_0= 2 in pure (RM) and silver nanoparticle containing RMs (AgNP-RM) at (a) 425 nm (b) 485 nm and (c) 565 nm.

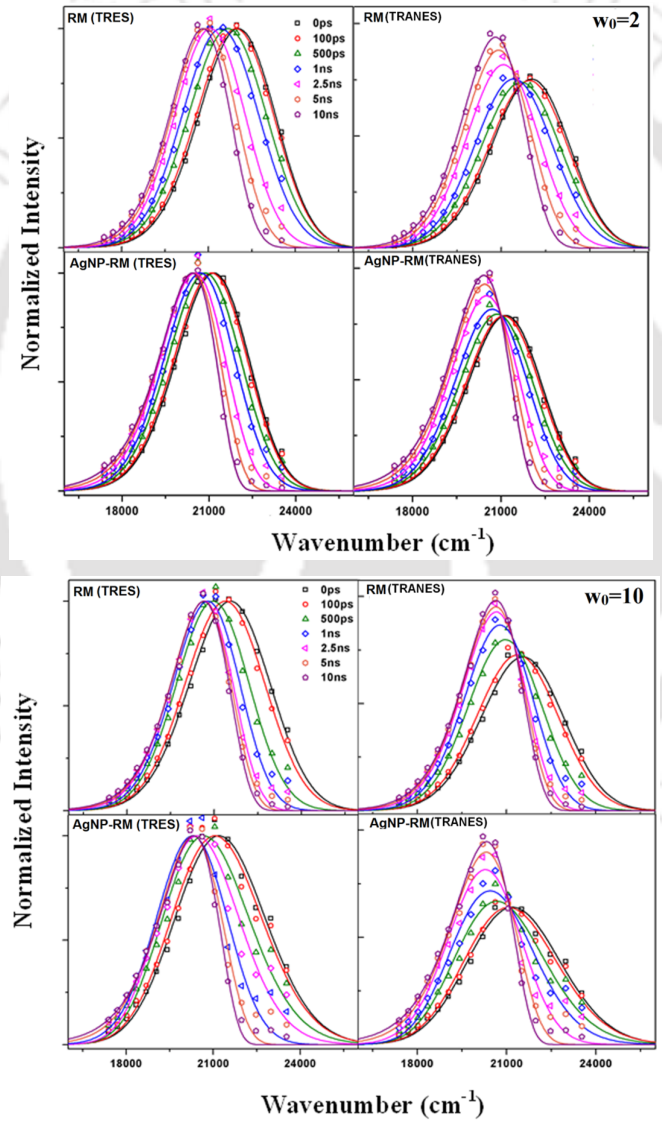

Figure A.4.5: Time resolved emission spectra (TRES) and time resolved area-normalised emission spectra (TRANES) spectra of the C343 at different time in pure

(RM) and silver nanoparticle containing (AgNP-RM) water/AOT/n-heptane reverse micellar system at $w_0 = 2,10$.

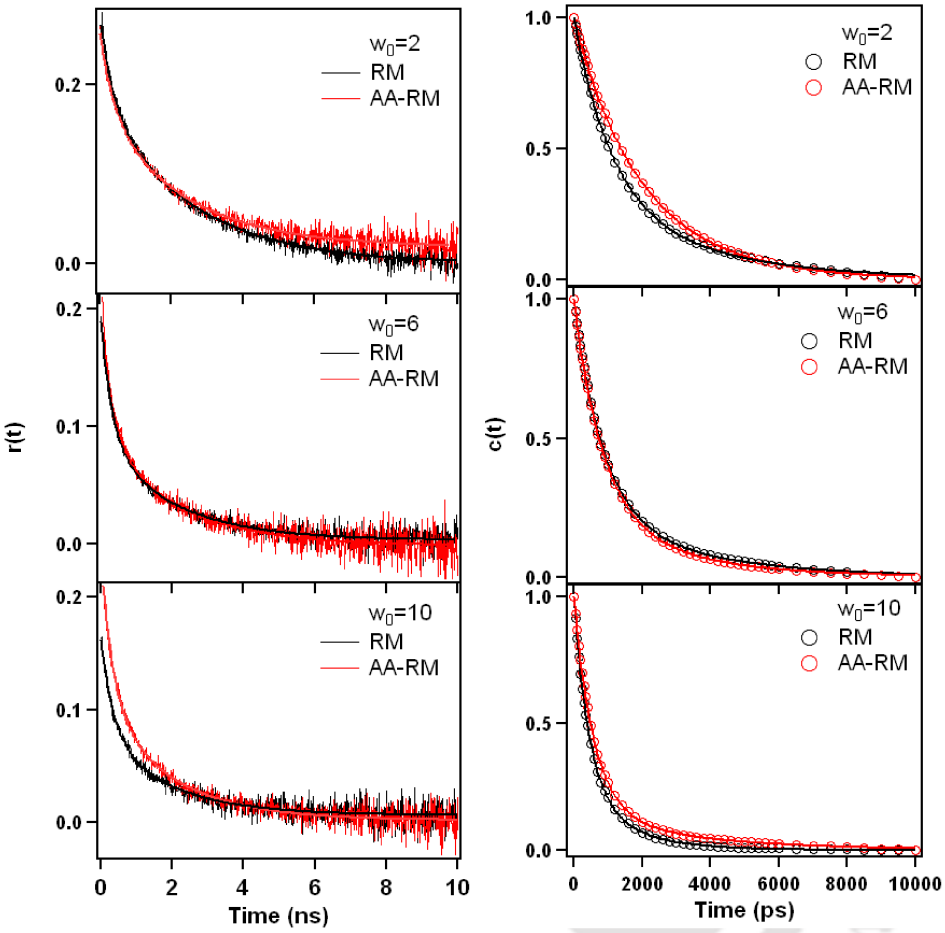

Figure A.4.6: Fluorescence anisotropy decays, r(t) and decay of the solvent response function, C(t) of C343 in pure (o) and ascorbic acid (o) RMs at w_0 values of 2, 6 and 10. The points represent the actual values while the solid lines denote the best bi-exponential fit in to the pure and ascorbic acid containing RMs.

Table A.4.1: The absorption maxima (λ_{abs}^{max}), Excitation maxima (λ_{ex}^{max}) and Emission maxima (λ_{em}^{max}) at 405 nm excitation of the coupled (C343 in AgNP-RM) and the individual (AgNPs, C343 in RMs) systems at different w_0 values.

System	w_0	λ_{abs}^{max}(nm)	λ_{ex}^{max}(nm)	λ_{em}^{max} (nm)
Silver nanoparticles (AgNPs) (i)	2	410	-	-
	6	402	-	-
	10	404		-
C343 in aqueous (RM)	2	412	412	475
	6	417	417	481
	10	420	420	484
C343 in AgNP-RM (ii)	2	414	430	481
	6	404	434	487
	10	406	438	489
(ii)-(i)	2	431	-	-
(ii)-(i)	6	434	-	-
(ii)-(i)	10	438	-	-

Table A.4.2: The fluorescence maxima ν_{em}^{max}(in cm^{-1}) at various excitation wavelengths (λ_{ex}) and the corresponding REES (red edge excitation shifts) of the coupled (C343 in AgNP-RM) and the individual (AgNPs or C343 in RM) systems at different w_0 values.

System		ν_{em}^{max} (cm^{-1})		
		$\lambda_{ex} = 400\ nm$	$\lambda_{ex} = 470\ nm$	Shift ($\Delta\nu$ cm^{-1})
w_0=2	RM	21100	20530	570
	AgNP-RM	20830	20530	300
w_0=6	RM	20790	20410	380
	AgNP-RM	20580	20410	170
w_0=10	RM	20700	20450	250
	AgNP-RM	20490	20280	210

For Chapter 5

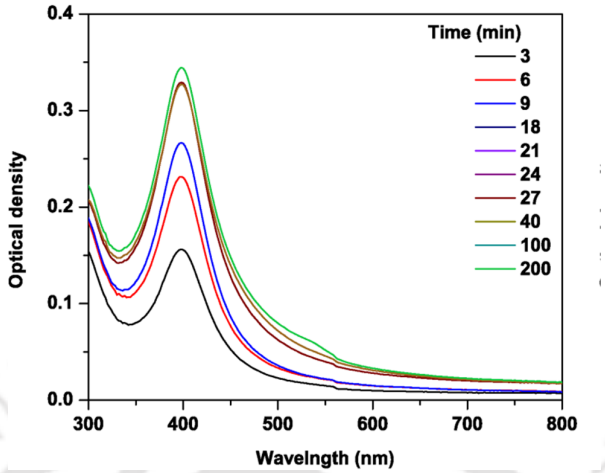

Figure A.5.1: Difference spectra generated mathematically by subtracting fluorophore safranin absorbance spectra from safranin-silver nanoparticles composite absorption spectrum at different time during the growth of silver nanoparticles.

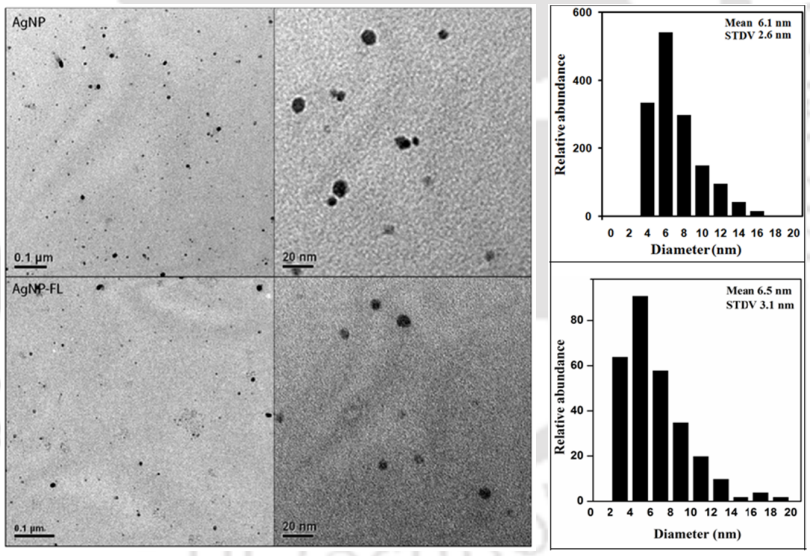

Figure A.5.2: Transmission electron microscopy images and size distribution histograms of AgNP within AOT RM with and without probe fluorescein.

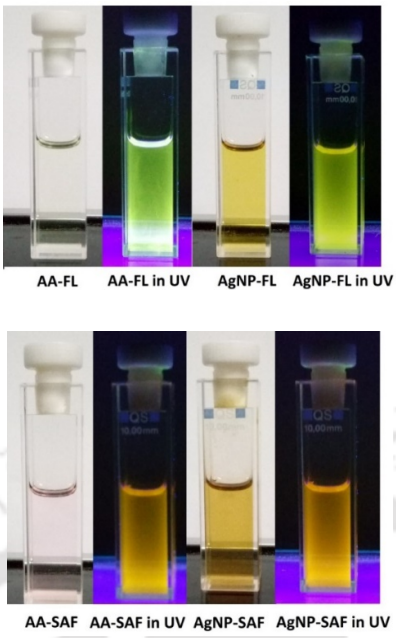

Figure A.5.3: Photographs of the solutions in normal light and under UV irradiation (362 nm) before and after silver nanoparticles formation. AgNP-FL composite system (upper panel) and AgNP-SAF composite system (lower panel).

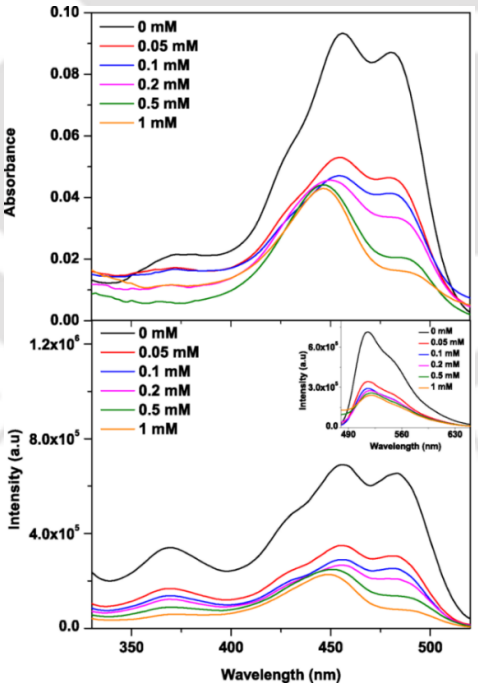

Figure A.5.4: Absorption spectrum (a), excitation spectrum(b) at (λ_{em}= 530 nm) and emission spectrum (c) at (λ_{ex}= 445 nm) of fluorescein in AOT reverse micellar solution at various ascorbic acid concentration.

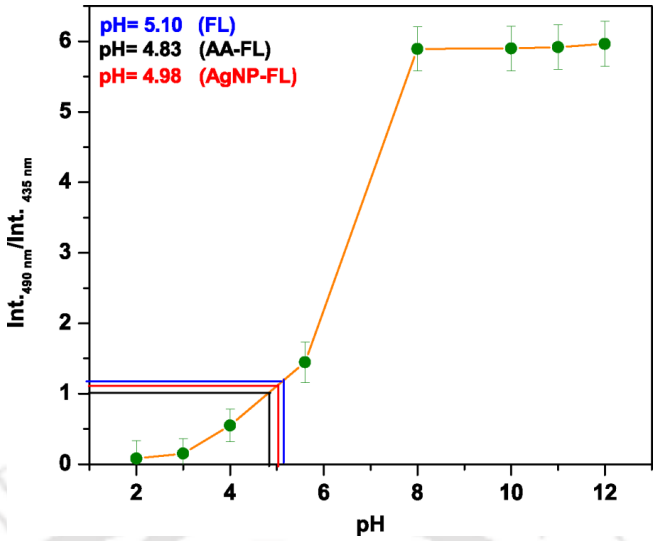

Figure A.5.5: Estimation of pH insdie the water pool of AOT RMs in presence of various additives such as ascorbic acid (AA-FL), silver nanoprticles (AgNP-FL) and only water (FL). For genration of calibration curve using fluorescein as a pH probe Masatoshi Hasegawa method was followed.[113] Briefly, excitation band intensity ratio (I_{490}/I_{435}) of fluorescein in aquesous solution ploted as a function of pH adjusted by using NaOH/HCl.

Table A.5.1: Summary of dynamic light scattering(DLS) measurementsdata of AOT reverse micellar system solution contaning fluorescein dye and growing silver nanoparticlein the core of reverse micelles at different time.

System	Time(minutes)	Hydrodynamic diameter (nm)
Fluorescein (FL)	-	6.86
FL+ silver nanoparticle(AgNPs)	3	7.17
Fl-AgNPs	20	8.72
Fl-AgNPs	100	8.12
Fl-AgNPs	200	8.00
Fl-AgNPs	1000	8.40

For Chapter 6

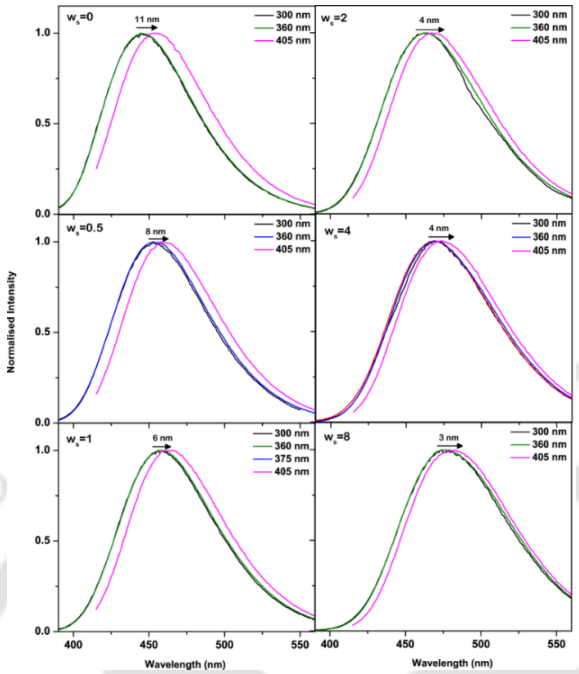

Figure A.6.1: The fluorescence spectra at various excitation wavelengths (λ_{ex}) and the corresponding REES (red-edge excitation shifts) of fluorophore 4-AP inside acetonitrile/AOT/*n*-heptane microemulsion at different w_s values.

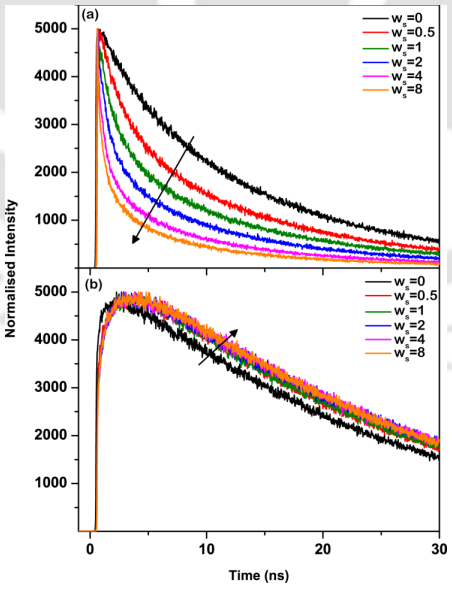

Figure A.6.2: Representative fluorescence transients of 4-AP in acetonitrile/AOT/*n*-heptane microemulsion various acetonitrile contents measured at (a) a short wavelength (λ_{em} = 410 nm) and (b) a long wavelength (λ_{em} = 580 nm).

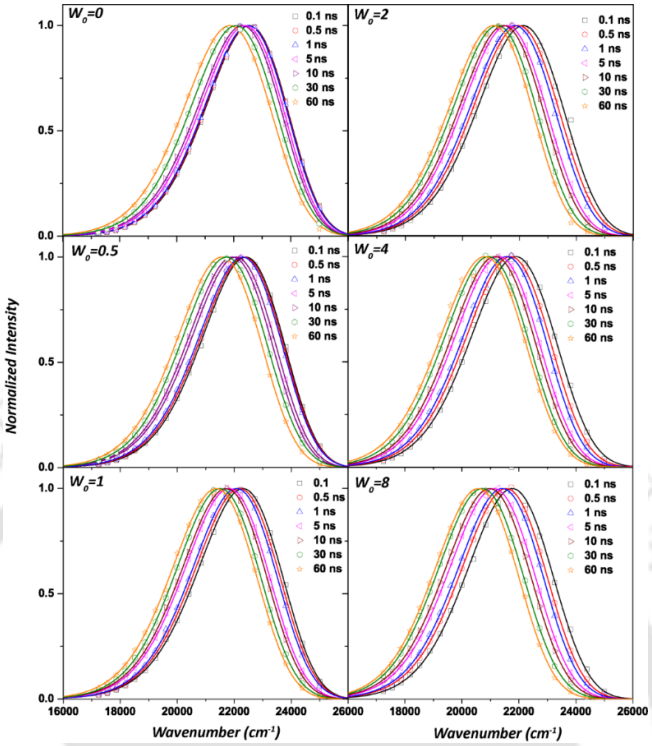

Figure A.6.3: Time resolved emission spectra (TRES) of the 4-AP inside acetonitrile/AOT/*n*-heptane microemulsion at different w_s.

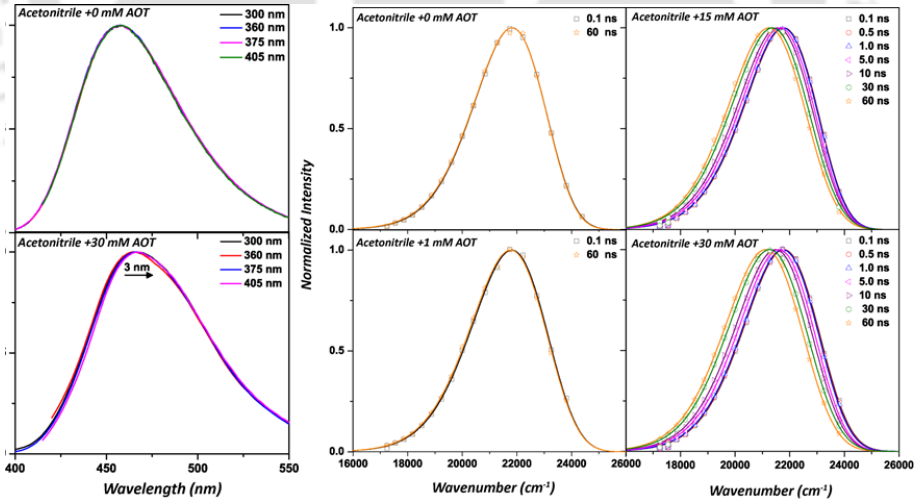

Figure A.6.4: Emission spectra of 4-AP in neat acetonitrile and in the presence of 30 mM AOT at various excitation wavelengths (left panel). Time resolved emission spectra (TRES) of the 4-AP at various nanosecond timescale in acetonitrile/AOT mixture at different AOT concentration (right panel). Note that no REES was observed

for neat acetonitrile but a small value (3 nm) was observed in the presence of 30 mM AOT.

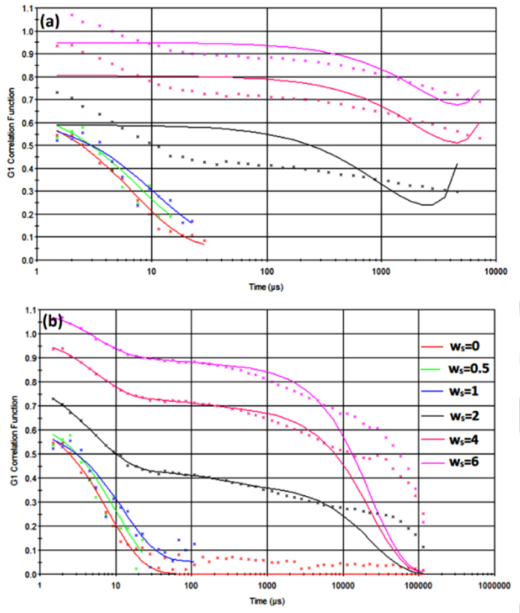

Figure A.6.5: Plot of cumulants fit (a) and distribution fits (b) of the autocorrelation function of acetonitrile/AOT/*n*-heptane microemulsion at different w_s values.

Table A.6.1: The fluorescence maxima in nm at various excitation wavelengths and the corresponding REES (red edge excitation shifts) of fluorophore 4-AP inside acetonitrile/AOT/*n*-heptane microemulsion at different w_s values.

System	ν_{em}^{max} (nm)		
	$\lambda_{ex} = 300\ nm$	$\lambda_{ex} = 405\ nm$	Shift (Δν nm)
w_s=0	443	454	11
w_s=0.5	452	460	8
w_s=1	457	463	6
w_s=1.5	460	465	5
w_s=2	463	467	4
w_s=2.5	465	469	4
w_s=3	467	471	4
w_s=4	468	472	4
w_s=6	474	477	3
w_s=8	476	479	3

Table A.6.2: Size obtained from dynamic light scattering (DLS) measurements for acetonitrile/AOT/*n*-heptane microemulsion at different w_s values.

w_s	Size (Z.avg) nm	Peak size (distribution size) nm	PDI
0	3.00	3.60	0.2
0.5	3.60	4.70	0.2
1	5.20	5.60	0.2
1.5	347.0	2.30, 148.0	0.3
2	598.5	1.80, 2.90,117.0	0.6
4	2103.0	2.40, 64.0	1.0
6	2930.0	2.50, 28.0	1.0

For Chapter 7

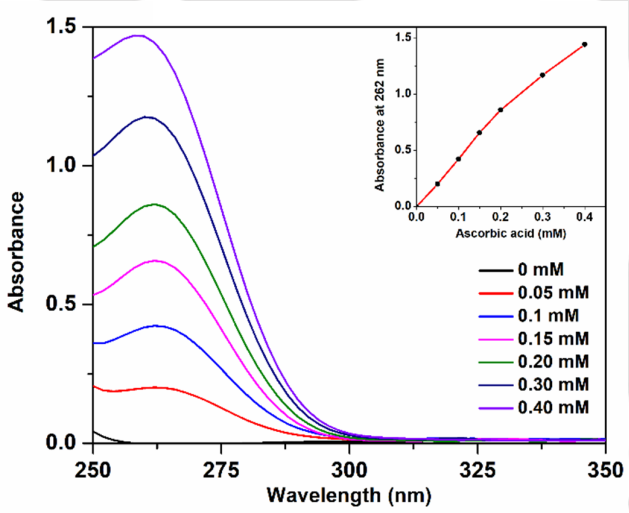

Figure A.7.1: Absorption spectra showing gradual dissolution of AA into AOT (90 mM)/*n*-heptane solution (w_s = 0). The concentrations of AA are given in the legend considering complete dissolution. The inset shows the linear increase of the absorbance at 262 nm, which supports complete dissolution inside the acetonitrile free microemulsion.

Table A.7.1. Summary of optical characteristics of SPR band of the AgNP prepared in acetonitrile/AOT/*n*-heptane microemulsion at different w_s values at different AA concentration. Overall concentrations [$AgNO_3$]=0.3 mM; [AOT]=90 mM.

w_s	AA (mM)	λ_{max} (nm)	A $_{max}$	§FWHM (nm)
0.5	0	-	-	-
	0.05	405	1.12	114
	0.10	400	1.19	73
	0.20	401	2.53	62
	0.30	401	2.44	55
1	0	-	-	-
	0.05	406	1.57	96
	0.10	401	1.58	81
	0.20	402	2.38	58
	0.30	402	2.64	66
2	0	-	-	-
	0.05	405	1.11	101
	0.10	401	1.27	94
	0.20	400	0.99	71
	0.30	400	0.92	67

§

FWHM=Full width at half maxima.

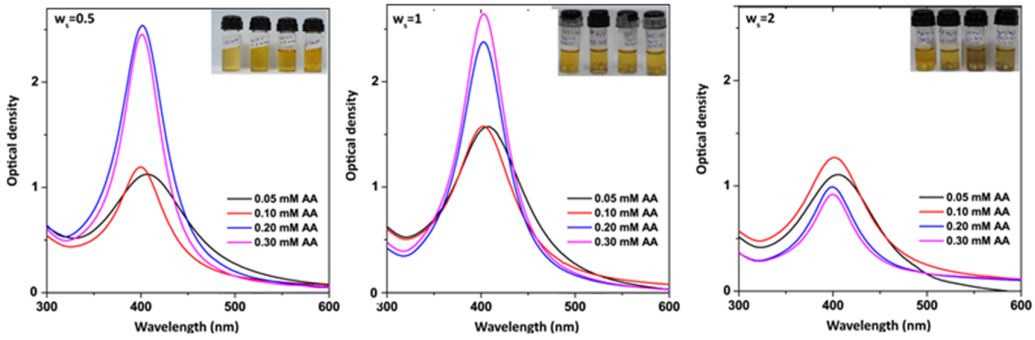

Figure A.7.2: The UV-Vis spectra of AgNPs formed in the acetonitrile/AOT/*n*-heptane microemulsions at w_s = 0.5, 1 and 2. The concentration of $AgNO_3$ was fixed at 0.3 mM while AA concentrations were varied at 0.05, 0.10, 0.20 and 0.30 mM, respectively. Photographs of each solution are given in the inset.

Table A.7.2. Hydrodynamic diameter of acetonitrile/AOT/*n*-heptane microemulsion at different w_s values obtained from dynamic light scattering (DLS) measurements in absence of silver nanoparticles and in presence of silver nanoparticles. The concentration of $AgNO_3$ and AA was fixed at 0.3 mM and 0.20 mM, respectively.

w_s	Size (Z.avg) nm	Peak size (distribution size) nm	§PDI
0.5 (RM)	3.60	4.70	0.2
1 (RM)	5.20	5.60	0.2
2 (RM)	-	-	0.6
0.5 (AgNP)	4.80	5.80	0.2
1 (AgNP)	5.30	6.40	0.2
2 (AgNP)	-	-	0.7

§ PDI=Polydispersity index.

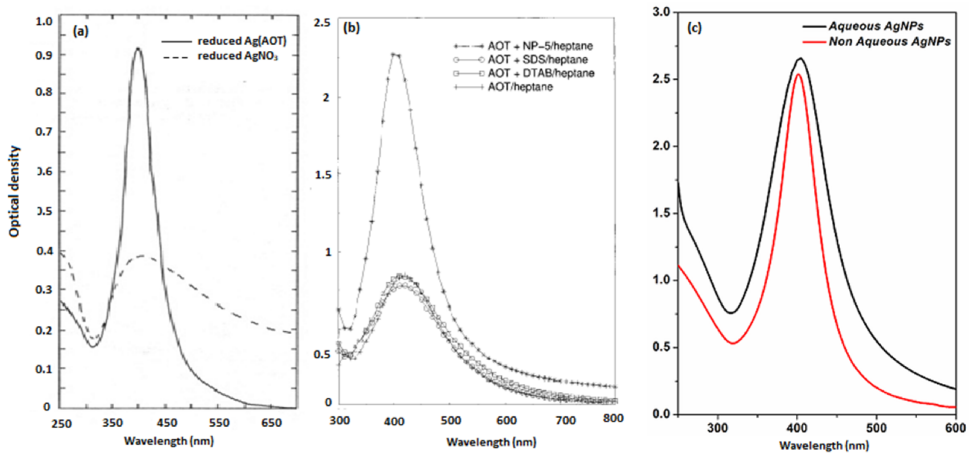

Figure A.7.3: Comparison of optical quality of the AgNPs SPR band synthesized inside aqueous AOT micro emulsion at w_0=10 by the work of (a) Petit et al.[109], (b) Bagwe et al.[172] and (c) our previous work (for details see **Figure 1.11** and **Figure 3.1**).[18] It is appearent that optical quality AgNPs synthesized here by the nonaqueous acetonitrile microemulsion route is superior compared to all other previously reported microemulsion routes.

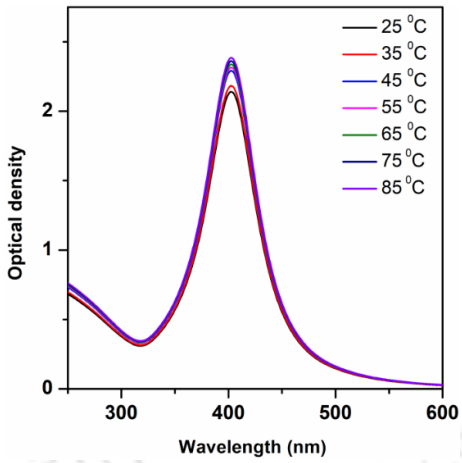

Figure A.7.4: The UV-Vis spectra of AgNPs/AOT/*n*-heptane microemulsions at w_s = 0.5 at different temperature. The concentration of $AgNO_3$ and AA was fixed at 0.3 mM and 0.20 mM, respectively.

REFERENCES

1. Barchiesi, D., Lycurgus Cup: Inverse Problem Using Photographs for Characterization of Matter. *J. Opt. Soc. Am. A* **2015**, *32*, 1544-1555.
2. Barber, D. J.; Freestone, I. C., An Investigation of the Origin of the Colour of the Lycurgus Cup by Analytical Transmission Electron Microscopy. *Archaeometry* **1990**, *32*, 33-45.
3. Merga, G.; Cass, L. C.; Chipman, D. M.; Meisel, D., Probing Silver Nanoparticles During Catalytic H2 Evolution. *J. Am. Chem. Soc.* **2008**, *130*, 7067-7076.
4. Zheng, L.; Zhang, R.; Ni, Y.; Du, Q.; Wang, X.; Zhang, J.; Li, W., Catalytic Performance of Ag Nanoparticles Templated by Polymorphic DNA. *Catal Lett* **2010**, *139*, 145-150.
5. Jain, P.; Huang, X.; El-Sayed, I.; El-Sayed, M., Review of Some Interesting Surface Plasmon Resonance-Enhanced Properties of Noble Metal Nanoparticles and Their Applications to Biosystems. *Plasmonics* **2007**, *2*, 107-118.
6. Schwiertz, J.; Wiehe, A.; Gräfe, S.; Gitter, B.; Epple, M., Calcium Phosphate Nanoparticles as Efficient Carriers for Photodynamic Therapy against Cells and Bacteria. *Biomaterials* **2009**, *30*, 3324-3331.
7. Ni, W.; Chen, H.; Su, J.; Sun, Z.; Wang, J.; Wu, H., Effects of Dyes, Gold Nanocrystals, Ph, and Metal Ions on Plasmonic and Molecular Resonance Coupling. *J. Am. Chem. Soc.* **2010**, *132*, 4806-4814.
8. Choi, Y.; Kang, T.; Lee, L. P., Plasmon Resonance Energy Transfer (Pret)-Based Molecular Imaging of Cytochrome C in Living Cells. *Nano Lett.* **2009**, *9*, 85-90.
9. Zheng, Y. B.; Yang, Y.-W.; Jensen, L.; Fang, L.; Juluri, B. K.; Flood, A. H.; Weiss, P. S.; Stoddart, J. F.; Huang, T. J., Active Molecular Plasmonics: Controlling Plasmon Resonances with Molecular Switches. *Nano Lett.* **2009**, *9*, 819-825.
10. Sondi, I.; Salopek-Sondi, B., Silver Nanoparticles as Antimicrobial Agent: A Case Study on E. Coli as A model for Gram-Negative Bacteria. *J. Colloid. Int. Sci.* **2004**, *275*, 177-182.
11. Xiu, Z.-M.; Ma, J.; Alvarez, P. J. J., Differential Effect of Common Ligands and Molecular Oxygen on Antimicrobial Activity of Silver Nanoparticles Versus Silver Ions. *Environ. Sci. Technol.* **2011**, *45*, 9003-9008.
12. Mulvaney, P., Surface Plasmon Spectroscopy of Nanosized Metal Particles. *Langmuir* **1996**, *12*, 788-800.
13. Kelly, K. L.; Coronado, E.; Zhao, L. L.; Schatz, G. C., The Optical Properties of Metal Nanoparticles: The Influence of Size, Shape, and Dielectric Environment. *J. Phys. Chem. B* **2003**, *107*, 668-677.
14. Henry, A.-I.; Bingham, J. M.; Ringe, E.; Marks, L. D.; Schatz, G. C.; Van Duyne, R. P., Correlated Structure and Optical Property Studies of Plasmonic Nanoparticles. *J. Phys. Chem. C* **2011**, *115*, 9291-9305.
15. Mayer, K. M.; Hafner, J. H., Localized Surface Plasmon Resonance Sensors. *Chem. Rev.* **2011**, *111*, 3828-3857.
16. Liang, Z.; Sun, J.; Jiang, Y.; Jiang, L.; Chen, X., Plasmonic Enhanced Optoelectronic Devices. *Plasmonics* **2014**, *9*, 859-866.
17. Stamplecoskie, K., Silver Nanoparticles: From Bulk Material to Colloidal Nanoparticles. In *Silver Nanoparticle Applications: In the Fabrication and Design of Medical and Biosensing Devices*, Alarcon, E. I.; Griffith, M.; Udekwu, K. I., Eds. Springer International Publishing: Cham, 2015; pp 1-12.

18. Singha, D.; Barman, N.; Sahu, K., A Facile Synthesis of High Optical Quality Silver Nanoparticles by Ascorbic Acid Reduction in Reverse Micelles at Room Temperature. *J. Colloid Interface Sci.* **2014**, *413*, 37-42.
19. Lakowicz, J. R., *Principles of Fluorescence Spectroscopy*; Springer: New York, 2006.
20. Ni, W.; Ambjörnsson, T.; Apell, S. P.; Chen, H.; Wang, J., Observing Plasmonic−Molecular Resonance Coupling on Single Gold Nanorods. *Nano Lett.* **2010**, *10*, 77-84.
21. Maier, S. A., *Plasmonics: Fundamentals and Applications*; Springer US, 2007.
22. Kreibig, U.; Vollmer, M., *Optical Properties of Metal Clusters*; Springer Berlin Heidelberg, 1995.
23. Alarcon, E. I.; Griffith, M.; Udekwu, K. I., *Silver Nanoparticle Applications: In the Fabrication and Design of Medical and Biosensing Devices*; Springer International Publishing, 2015.
24. Agnihotri, S.; Mukherji, S.; Mukherji, S., Size-Controlled Silver Nanoparticles Synthesized over the Range 5-100 Nm Using the Same Protocol and Their Antibacterial Efficacy. *RSC Adv.* **2014**, *4*, 3974-3983.
25. Sherry, L. J.; Chang, S.-H.; Schatz, G. C.; Van Duyne, R. P.; Wiley, B. J.; Xia, Y., Localized Surface Plasmon Resonance Spectroscopy of Single Silver Nanocubes. *Nano Lett.* **2005**, *5*, 2034-2038.
26. Maier, S. A.; Kik, P. G.; Atwater, H. A.; Meltzer, S.; Harel, E.; Koel, B. E.; Requicha, A. A. G., Local Detection of Electromagnetic Energy Transport Below the Diffraction Limit in Metal Nanoparticle Plasmon Waveguides. *Nature Mat.* **2003**, *2*, 229-232.
27. Tegg, L.; Cuskelly, D.; Keast, V. J., Plasmon Responses in the Sodium Tungsten Bronzes. *Plasmonics* **2017**.
28. N'Gom, M.; Li, S.; Schatz, G.; Erni, R.; Agarwal, A.; Kotov, N.; Norris, T. B., Electron-Beam Mapping of Plasmon Resonances in Electromagnetically Interacting Gold Nanorods. *Physical Review B* **2009**, *80*, 113411.
29. Doherty, M. D.; Murphy, A.; Pollard, R. J.; Dawson, P., Surface-Enhanced Raman Scattering from Metallic Nanostructures: Bridging the Gap between the near-Field and Far-Field Responses. *Physical Review X* **2013**, *3*, 011001.
30. Baruah, B.; Miller, T.-A., Polyoxovanadate Fabricated Gold Nanoparticles: Application in Sers. *J. Colloid. Int. Sci.* **2017**, *487*, 209-216.
31. Mie, G., Articles on the Optical Characteristics of Turbid Tubes, Especially Colloidal Metal Solutions. *Annalen der Physik* **1908**, *25*, 377-445.
32. Mohammadi Bilankohi, S., *Optical Scattering and Absorption Characteristics of Silver and Silica/ Silver Core/Shell Nanoparticles*, 2015; Vol. 31, p 2259-2263.
33. Durante, N.; Fortunelli, A.; Broyer, M.; Stener, M., Optical Properties of Au Nanoclusters from Td-Dft Calculations. *J. Phys. Chem. C* **2011**, *115*, 6277-6282.
34. Garcia, M. A., Surface Plasmons in Metallic Nanoparticles: Fundamentals and Applications. *J. Phys. D appl. Phys.* **2011**, *44*, 283001.
35. Baruah, B., In Situ and Facile Synthesis of Silver Nanoparticles on Baby Wipes and Their Applications in Catalysis and Sers. *RSC Adv.* **2016**, *6*, 5016-5023.
36. Kneipp, J.; Kneipp, H.; Wittig, B.; Kneipp, K., Novel Optical Nanosensors for Probing and Imaging Live Cells. *Nanomedicine-UK* **2010**, *6*, 214-226.
37. Jain, P.; Pradeep, T., Potential of Silver Nanoparticle-Coated Polyurethane Foam as an Antibacterial Water Filter. *Biotechnol. Bioeng.* **2005**, *90*, 59-63.

38. Tan, T. T. Y.; Yip, C. K.; Beydoun, D.; Amal, R., Effects of Nano-Ag Particles Loading on Tio2 Photocatalytic Reduction of Selenate Ions. *Chem. Eng. J.* **2003**, *95*, 179-186.
39. Solanki, J. N.; Murthy, Z. V. P., Preparation of Silver Nanofluids with High Electrical Conductivity. *J Disper Sci Technol.* **2011**, *32*, 724-730.
40. Ni, W.; Yang, Z.; Chen, H.; Li, L.; Wang, J., Coupling between Molecular and Plasmonic Resonances in Freestanding Dye−Gold Nanorod Hybrid Nanostructures. *J. Am. Chem. Soc.* **2008**, *130*, 6692-6693.
41. Lee, K.-C.; Lin, S.-J.; Lin, C.-H.; Tsai, C.-S.; Lu, Y.-J., Size Effect of Ag Nanoparticles on Surface Plasmon Resonance. *Surf. Coat. Technol.* **2008**, *202*, 5339-5342.
42. Saha, A.; Basiruddin, S. K.; Sarkar, R.; Pradhan, N.; Jana, N. R., Functionalized Plasmonic−Fluorescent Nanoparticles for Imaging and Detection. *J. Phys. Chem. C* **2009**, *113*, 18492-18498.
43. Williams, T. A.; Lee, J.; Diemler, C. A.; Subir, M., Magnetic Vs. Non-Magnetic Colloids – a Comparative Adsorption Study to Quantify the Effect of Dye-Induced Aggregation on the Binding Affinity of an Organic Dye. *J. Colloid. Int. Sci.* **2016**, *481*, 20-27.
44. Lakowicz, J. R., Radiative Decay Engineering: Biophysical and Biomedical Applications. *Anal. Biocchem.* **2001**, *298*, 1-24.
45. Pramanik, S.; Bhattacharya, S. C.; Imae, T., Fluorescence Quenching of 3,7-Diamino-2,8-Dimethyl-5-Phenyl Phenazinium Chloride by Agcl and Ag Nanoparticles. *J. Lumin.* **2007**, *126*, 155-159.
46. Su, H.; Zhong, Y.; Ming, T.; Wang, J.; Wong, K. S., Extraordinary Surface Plasmon Coupled Emission Using Core/Shell Gold Nanorods. *J. Phys. Chem. C* **2012**, *116*, 9259-9264.
47. De Luca, A.; Dhama, R.; Rashed, A. R.; Coutant, C.; Ravaine, S.; Barois, P.; Infusino, M.; Strangi, G., Double Strong Exciton-Plasmon Coupling in Gold Nanoshells Infiltrated with Fluorophores. *Appl. Phys. Lett.* **2014**, *104*, 103103.
48. Lakowicz, J. R.; Ray, K.; Chowdhury, M.; Szmacinski, H.; Fu, Y.; Zhang, J.; Nowaczyk, K., Plasmon-Controlled Fluorescence: A New Paradigm in Fluorescence Spectroscopy. *Analyst* **2008**, *133*, 1308-1346.
49. Chowdhury, M. H.; Gray, S. K.; Pond, J.; Geddes, C. D.; Aslan, K.; Lakowicz, J. R., Computational Study of Fluorescence Scattering by Silver Nanoparticles. *J.Opt. Soc. Am. B* **2007**, *24*, 2259-2267.
50. Mayergoyz, I. D.; Zhang, Z.; Miano, G., Analysis of Dynamics of Excitation and Dephasing of Plasmon Resonance Modes in Nanoparticles. *Phys. Rev. Lett.* **2007**, *98*, 147401.
51. Dutta Choudhury, S.; Badugu, R.; Ray, K.; Lakowicz, J. R., Silver–Gold Nanocomposite Substrates for Metal-Enhanced Fluorescence: Ensemble and Single-Molecule Spectroscopic Studies. *J. Phys. Chem. C* **2012**, *116*, 5042-5048.
52. L.-Viger, M.; Brouard, D.; Boudreau, D., Plasmon-Enhanced Resonance Energy Transfer from a Conjugated Polymer to Fluorescent Multilayer Core−Shell Nanoparticles: A Photophysical Study. *J. Phys. Chem. C* **2011**, *115*, 2974-2981.
53. De, S.; Kundu, R., Spectroscopic Studies with Fluorescein Dye—Protonation, Aggregation and Interaction with Nanoparticles. *J. Photochem. Photobiol. A* **2011**, *223*, 71-81.
54. Narband, N.; Uppal, M.; Dunnill, C. W.; Hyett, G.; Wilson, M.; Parkin, I. P., The Interaction between Gold Nanoparticles and Cationic and Anionic Dyes: Enhanced Uv-Visible Absorption. *Phys. Chem. Chem. Phys.* **2009**, *11*, 10513-10518.

55. Zhao, J.; Jensen, L.; Sung, J.; Zou, S.; Schatz, G. C.; Van Duyne, R. P., Interaction of Plasmon and Molecular Resonances for Rhodamine 6g Adsorbed on Silver Nanoparticles. *J. Am. Chem. Soc.* **2007**, *129*, 7647-7656.
56. Gersten, J.; Nitzan, A., *Spectroscopic Properties of Molecules Interacting with Small Dielectric Particles*, 1981; Vol. 75, p 1139-1152.
57. Singha, D.; Sahu, D. K.; Sahu, K., Coupling of Molecular Transition with the Surface Plasmon Resonance of Silver Nanoparticles inside the Restricted Environment of Reverse Micelles. *ACS Omega* **2017**, *2*, 5494-5503.
58. Ni, W.; Chen, H.; Su, J.; Sun, Z.; Wang, J.; Wu, H., Effects of Dyes, Gold Nanocrystals, Ph, and Metal Ions on Plasmonic and Molecular Resonance Coupling. *J. Am. Chem. Soc.*, *132*, 4806-4814.
59. Zhao, J.; Das, A.; Schatz, G. C.; Sligar, S. G.; Van Duyne, R. P., Resonance Localized Surface Plasmon Spectroscopy: Sensing Substrate and Inhibitor Binding to Cytochrome P450. *J. Phys. Chem. C* **2008**, *112*, 13084-13088.
60. Pan, S.; Wang, Z.; Rothberg, L. J., Enhancement of Adsorbed Dye Monolayer Fluorescence by a Silver Nanoparticle Overlayer. *J. Phys. Chem. B* **2006**, *110*, 17383-17387.
61. Yang, Z.; Ni, W.; Kou, X.; Zhang, S.; Sun, Z.; Sun, L.-D.; Wang, J.; Yan, C.-H., Incorporation of Gold Nanorods and Their Enhancement of Fluorescence in Mesostructured Silica Thin Films. *J. Phys. Chem. C* **2008**, *112*, 18895-18903.
62. Saini, R. K.; Gupta, P. K.; Das, K., Plasmon–Molecular Resonance Coupling: Chlorine-P6 Adsorbed on Poly-L-Lysine Stabilized Silver Nanoparticles. *J. Mol. Struct.* **2012**, *1024*, 13-17.
63. Sorokin, A. V.; Zabolotskii, A. A.; Pereverzev, N. V.; Yefimova, S. L.; Malyukin, Y. V.; Plekhanov, A. I., Plasmon Controlled Exciton Fluorescence of Molecular Aggregates. *J. Phys. Chem. C* **2014**, *118*, 7599-7605.
64. Lim, S. Y.; Kim, J. H.; Lee, J. S.; Park, C. B., Gold Nanoparticle Enlargement Coupled with Fluorescence Quenching for Highly Sensitive Detection of Analytes. *Langmuir* **2009**, *25*, 13302-13305.
65. Ragab, A. E. L. d. E. A.; Gadallah, A.; Mohamed, M. B.; Azzouz, I. M., Effect of Silver Nps Plasmon on Optical Properties of Fluorescein Dye. *Opt. Laser Technol.* **2013**, *52*, 109-112.
66. Kitching, H.; Kenyon, A. J.; Parkin, I. P., The Interaction of Gold and Silver Nanoparticles with a Range of Anionic and Cationic Dyes. *Phys. Chem. Chem. Phys.* **2014**, *16*, 6050-6059.
67. Ni, W.; Yang, Z.; Chen, H.; Li, L.; Wang, J., Coupling between Molecular and Plasmonic Resonances in Freestanding Dyeâ^'Gold Nanorod Hybrid Nanostructures. *J. Am. Chem. Soc.* **2008**, *130*, 6692-6693.
68. Cheng, D.; Xu, Q.-H., Separation Distance Dependent Fluorescence Enhancement of Fluorescein Isothiocyanate by Silver Nanoparticles. *Chem. Commun.* **2007**, 248-250.
69. Mandal, S.; Ghatak, C.; Rao, V. G.; Ghosh, S.; Sarkar, N., Pluronic Micellar Aggregates Loaded with Gold Nanoparticles (Au Nps) and Fluorescent Dyes: A Study of Controlled Nanometal Surface Energy Transfer. *J. Phys. Chem. C* **2012**, *116*, 5585-5597.
70. Rakshit, S.; Moulik, S. P.; Bhattacharya, S. C., Deciphering the Role of the Length of the Corona in Controlled Nset within Triblock Copolymers. *J. Phys. Chem. B* **2015**, *119*, 8457-8467.

71. Antonisamy, J. D.; Swain, J.; Dash, S., Study on Binding and Fluorescence Energy Transfer Efficiency of Rhodamine B with Pluronic F127-Gold Nanohybrid Using Optical Spectroscopy Methods. *Spectrochim Acta A.* **2017**, *173*, 139-143.
72. Wang, C.-y.; Liu, C.-y.; Wang, Y.; Shen, T., Spectral Characteristics and Photosensitization Effect on Tio2of Fluorescein in Aot Reversed Micelles. *J. Colloid. Int. Sci.* **1998**, *197*, 126-132.
73. Yoo, H.; Pak, J., Synthesis of Highly Fluorescent Silica Nanoparticles in a Reverse Microemulsion through Double-Layered Doping of Organic Fluorophores. *J. Nanopart. Res.* **2013**, *15*, 1-10.
74. Basiruddin, S. K.; Saha, A.; Pradhan, N.; Jana, N. R., Functionalized Gold Nanorod Solution Via Reverse Micelle Based Polyacrylate Coating. *Langmuir* **2010**, *26*, 7475-7481.
75. Schulman, J. H.; Stoeckenius, W.; Prince, L. M., Mechanism of Formation and Structure of Micro Emulsions by Electron Microscopy. *J. Phys. Chem.* **1959**, *63*, 1677-1680.
76. Barnickel, P.; Wokaun, A., Synthesis of Metal Colloids in Inverse Microemulsions. *Molecular Physics* **1990**, *69*, 1-9.
77. Correa, N. M.; Silber, J. J.; Riter, R. E.; Levinger, N. E., Nonaqueous Polar Solvents in Reverse Micelle Systems. *Chem. Rev.* **2012**, *112*, 4569-4602.
78. Levinger, N. E., Water in Confinement. *Science* **2002**, *298*, 1722-1723.
79. Sando, G. M.; Dahl, K.; Zhong, Q.; Owrutsky, J. C., Vibrational Relaxation of Azide in Formamide Reverse Micelles. *J. Phys. Chem. A* **2005**, *109*, 5788-5792.
80. Riter, R. E.; Undiks, E. P.; Kimmel, J. R.; Levinger, N. E., Formamide in Reverse Micelles: Restricted Environment Effects on Molecular Motion. *J. Phys. Chem. B* **1998**, *102*, 7931-7938.
81. Riter, R. E.; Kimmel, J. R.; Undiks, E. P.; Levinger, N. E., Novel Reverse Micelles Partitioning Nonaqueous Polar Solvents in a Hydrocarbon Continuous Phase. *J. Phys. Chem. B* **1997**, *101*, 8292-8297.
82. Falcone, R. D.; Correa, N. M.; Biasutti, M. A.; Silber, J. J., The Use of Acridine Orange Base (Aob) as Molecular Probe to Characterize Nonaqueous Aot Reverse Micelles. *J. Colloid. Int. Sci.* **2006**, *296*, 356-364.
83. Ray, S.; Moulik, S. P., Dynamics and Thermodynamics of Aerosol Ot-Aided Nonaqueous Microemulsions. *Langmuir* **1994**, *10*, 2511-2515.
84. Durantini, A. M.; Falcone, R. D.; Silber, J. J.; Correa, N. M., Effect of the Constrained Environment on the Interactions between the Surfactant and Different Polar Solvents Encapsulated within Aot Reverse Micelles. *ChemPhysChem* **2009**, *10*, 2034-2040.
85. Elles, C. G.; Levinger, N. E., Reverse Micelles Solubilizing Dmso and Dmso/Water Mixtures. *Chem. Phys. Lett.* **2000**, *317*, 624-630.
86. Hazra, P.; Chakrabarty, D.; Sarkar, N., Solvation Dynamics of Coumarin 152a in Methanol and Acetonitrile Reverse Micelles. *Chem. Phys. Lett.* **2002**, *358*, 523-530.
87. Hazra, P.; Chakrabarty, D.; Sarkar, N., Intramolecular Charge Transfer and Solvation Dynamics of Coumarin 152 in Aerosol-Ot, Water-Solubilizing Reverse Micelles, and Polar Organic Solvent Solubilizing Reverse Micelles. *Langmuir* **2002**, *18*, 7872-7879.
88. Hazra, P.; Sarkar, N., Solvation Dynamics of Coumarin 490 in Methanol and Acetonitrile Reverse Micelles. *Phys. Chem. Chem. Phys.* **2002**, *4*, 1040-1045.
89. Shirota, H.; Horie, K., Solvation Dynamics in Nonaqueous Reverse Micelles. *J. Phys. Chem. B* **1999**, *103*, 1437-1443.

90. Hazra, P.; Chakrabarty, D.; Chakraborty, A.; Sarkar, N., Effect of Hydrogen Bonding on Intramolecular Charge Transfer in Aqueous and Non-Aqueous Reverse Micelles. *J. Photochem. Photobiol. A* **2004**, *167*, 23-30.
91. Lu, R.; Zhu, R.; Zhong, R.; Yu, A., Locations of Methanol in Methanol-Containing Aot Reverse Micelles Revealed by Photophysics of Ir125. *J. Photochem. Photobiol. A* **2013**, *252*, 116-123.
92. Setua, P.; Seth, D.; Sarkar, N., To Probe the Structure of Methanol and Aerosol Ot (Aot) in Aot Reverse Micelles by Ftir Measurements. *Phys. Chem. Chem. Phys.* **2009**, *11*, 8913-8922.
93. Wang, J.-P.; Chen, J.-S.; Zhao, G.-J., Steady-State and Time-Resolved Spectroscopic Investigations on the Existence of Stable Methanol/Aot/N-Heptane Reverse Micelles. *J. Colloid. Int. Sci.* **2014**, *423*, 1-6.
94. Ganguly, A.; Paul, B. K.; Ghosh, S.; Guchhait, N., Probing the Location of Methanol in Methanol/Aot/N-Heptane System: True Microemulsion or Bi-Continuous Medium? *RSC Adv.* **2014**, *4*, 41122-41128.
95. Kwan, S.; Kim, F.; Akana, J.; Yang, P., Synthesis and Assembly of Bawo4 Nanorods. *Chem. Commun.* **2001**, 447-448.
96. Lai, W.-C.; Hong, L.-t., Preparation of Nanowire Silica inside Self-Assembled Sodium Bis(2-Ethylhexyl) Sulfosuccinate (Aot) Gels. *J. Phys. Chem. B* **2016**, *120*, 10010-10017.
97. Singha, D.; Barman, N.; Phukon, A.; Sahu, K., Selective Probing of Reverse Micelle Interfacial Layer Upon Silver Nanoparticle Formation Using Dynamic Stokes Shift Measurements. *J. Phys. Chem. C* **2014**, *118*, 10366-10374.
98. Singha, D.; Barman, N.; Sahu, K., A Facile Synthesis of High Optical Quality Silver Nanoparticles by Ascorbic Acid Reduction in Reverse Micelles at Room Temperature. *J. Colloid Interface Sci.* **2014**, *413*, 37-42.
99. Sunaina; Sethi, V.; Mehta, S. K.; Ganguli, A. K.; Vaidya, S., Understanding the Role of Co-Surfactants in Microemulsions on the Growth of Copper Oxalate Using Saxs. *Phys. Chem. Chem. Phys.* **2019**, *21*, 336-348.
100. Negro, E.; Latsuzbaia, R.; Koper, G. J. M., Bicontinuous Microemulsions for High Yield Wet Synthesis of Ultrafine Platinum Nanoparticles: Effect of Precursors and Kinetics. *Langmuir* **2014**, *30*, 8300-8307.
101. Samii, A. A.-Z.; de Savignac, A.; Rico, I.; Lattes, A., Waterless Microemulsions - Iv : Diels-Alder Reaction of Cyclopentadiene and Methylacrylate as a Probe of Formamide Microemulsions. *Tetrahedron* **1985**, *41*, 3683-3688.
102. Zhang, P.; Shao, C.; Zhang, Z.; Zhang, M.; Mu, J.; Guo, Z.; Liu, Y., In Situ Assembly of Well-Dispersed Ag Nanoparticles (Agnps) on Electrospun Carbon Nanofibers (Cnfs) for Catalytic Reduction of 4-Nitrophenol. *Nanoscale* **2011**, *3*, 3357-3363.
103. Tang, L. L.; Gunderson, W. A.; Weitz, A. C.; Hendrich, M. P.; Ryabov, A. D.; Collins, T. J., Activation of Dioxygen by a Taml Activator in Reverse Micelles: Characterization of an Feiiifeiv Dimer and Associated Catalytic Chemistry. *J. Am. Chem. Soc.* **2015**, *137*, 9704-9715.
104. Phukon, A.; Ray, S.; Sahu, K., Effect of Cosurfactants on the Interfacial Hydration of Ctab Quaternary Reverse Micelle Probed Using Excited State Proton Transfer. *Langmuir* **2016**, *32*, 10659-10667.
105. Zhu, D. M.; Feng, K. I.; Schelly, Z. A., Reverse Micelles of Triton X-100 in Cyclohexane: Effects of Temperature, Water Content, and Salinity on the Aggregation Behavior. *J. Phys. Chem.* **1992**, *96*, 2382-2385.

106. Kurtanidze, M.; Butkhuzi, T.; Rukhadze, M.; Kokiashvili, N.; Bezarashvili, G.; Marcus, J.; Kunz, W.; Sigua, K., Study of Structural Changes of Water Confined in Brij-30 Reverse Micelles: Revealing Influence of Ionic Additives. *Colloids Surf. A* **2017**, *519*, 98-105.
107. Eskici, G.; Axelsen, P. H., The Size of Aot Reverse Micelles. *J. Phys. Chem. B* **2016**, *120*, 11337-11347.
108. Falcone, R. D.; Correa, N. M.; Biasutti, M. A.; Silber, J. J., Properties of Aot Aqueous and Nonaqueous Microemulsions Sensed by Optical Molecular Probes. *Langmuir* **2000**, *16*, 3070-3076.
109. Petit, C.; Lixon, P.; Pileni, M. P., In Situ Synthesis of Silver Nanocluster in Aot Reverse Micelles. *J. Phys. Chem.* **1993**, *97*, 12974-12983.
110. Crans, D. C.; Baruah, B.; Ross, A.; Levinger, N. E., Impact of Confinement and Interfaces on Coordination Chemistry: Using Oxovanadate Reactions and Proton Transfer Reactions as Probes in Reverse Micelles. *Coord Chem Rev.* **2009**, *253*, 2178-2185.
111. Zhong, Q.; Steinhurst, D. A.; Carpenter, E. E.; Owrutsky, J. C., Fourier Transform Infrared Spectroscopy of Azide Ion in Reverse Micelles. *Langmuir* **2002**, *18*, 7401-7408.
112. Das, S.; Datta, A.; Bhattacharyya, K., Deuterium Isotope Effect on 4-Aminophthalimide in Neat Water and Reverse Micelles. *J. Phys. Chem. A* **1997**, *101*, 3299-3304.
113. Hasegawa, M., Buffer-Like Action in Water Pool of Aerosol Ot Reverse Micelles. *Langmuir* **2001**, *17*, 1426-1431.
114. Martinez, A. V.; Dominguez, L.; Małolepsza, E.; Moser, A.; Ziegler, Z.; Straub, J. E., Probing the Structure and Dynamics of Confined Water in Aot Reverse Micelles. *J. Phys. Chem. B* **2013**, *117*, 7345-7351.
115. Brown, D.; Clarke, J. H. R., Molecular Dynamics Simulation of a Model Reverse Micelle. *J. Phys. Chem.* **1988**, *92*, 2881-2888.
116. Jain, T. K.; Varshney, M.; Maitra, A., Structural Studies of Aerosol Ot Reverse Micellar Aggregates by Ft-Ir Spectroscopy. *J. Phys. Chem.* **1989**, *93*, 7409-7416.
117. Crans, D. C.; Levinger, N. E., The Conundrum of Ph in Water Nanodroplets: Sensing Ph in Reverse Micelle Water Pools. *Acc. Chem. Res.* **2012**, *45*, 1637-1645.
118. Riter, R. E.; Willard, D. M.; Levinger, N. E., Water Immobilization at Surfactant Interfaces in Reverse Micelles. *J. Phys. Chem. B* **1998**, *102*, 2705-2714.
119. Corbeil, E. M.; Riter, R. E.; Levinger, N. E., Cosurfactant Impact on Probe Molecule in Reverse Micelles. *J. Phys. Chem. B* **2004**, *108*, 10777-10784.
120. Baruah, B.; Roden, J. M.; Sedgwick, M.; Correa, N. M.; Crans, D. C.; Levinger, N. E., When Is Water Not Water? Exploring Water Confined in Large Reverse Micelles Using a Highly Charged Inorganic Molecular Probe. *J. Am. Chem. Soc.* **2006**, *128*, 12758-12765.
121. Crans, D. C.; Baruah, B.; Gaidamauskas, E.; Lemons, B. G.; Lorenz, B. B.; Johnson, M. D., Impairment of Ascorbic Acid's Anti-Oxidant Properties in Confined Media: Inter and Intramolecular Reactions with Air and Vanadate at Acidic Ph. *J Inorg Biochem.* **2008**, *102*, 1334-1347.
122. Marques, B. S.; Nucci, N. V.; Dodevski, I.; Wang, K. W. C.; Athanasoula, E. A.; Jorge, C.; Wand, A. J., Measurement and Control of Ph in the Aqueous Interior of Reverse Micelles. *J. Phys. Chem. B* **2014**, *118*, 2020-2031.
123. Pant, D.; Levinger, N. E., Dynamics of Polar Solvation at the Surface of a Zro2 Nanoparticle. *Chem. Phys. Lett.* **1998**, *292*, 200-206.

124. Bose, D.; Sarkar, D.; Girigoswami, A.; Mahata, A.; Ghosh, D.; Chattopadhyay, N., Photophysics and Rotational Relaxation Dynamics of Cationic Phenazinium Dyes in Anionic Reverse Micelles: Effect of Methyl Substitution. *J. Chem. Phys.* **2009**, *131*, 114707.
125. Danielsson, I.; Lindman, B., The Definition of Microemulsion. *Colloids and Surfaces* **1981**, *3*, 391-392.
126. Zana, R., *Dynamics of Surfactant Self-Assemblies: Micelles, Microemulsions, Vesicles and Lyotropic Phases*; CRC Press, 2005.
127. Solans, C.; Solé, I., Nano-Emulsions: Formation by Low-Energy Methods. *Curr. Opin. Colloid Interface Sci.* **2012**, *17*, 246-254.
128. Liu, D.; Ma, J.; Cheng, H.; Zhao, Z., Investigation on the Conductivity and Microstructure of Aot/Non-Ionic Surfactants/Water/N-Heptane Mixed Reverse Micelles. *Colloids Surf. A* **1998**, *135*, 157-164.
129. Sethi, V.; Mishra, J.; Bhattacharyya, A.; Sen, D.; Ganguli, A. K., Hydrotrope Induced Structural Modifications in Ctab/Butanol/Water/Isooctane Reverse Micellar Systems. *Phys. Chem. Chem. Phys.* **2017**, *19*, 22033-22048.
130. Sharma, S.; Ganguli, A. K., Spherical-to-Cylindrical Transformation of Reverse Micelles and Their Templating Effect on the Growth of Nanostructures. *J. Phys. Chem. B* **2014**, *118*, 4122-4131.
131. Borkovec, M.; Eicke, H. F.; Hammerich, H.; Das Gupta, B., Two Percolation Processes in Microemulsions. *J. Phys. Chem.* **1988**, *92*, 206-211.
132. Derouiche, A.; Tondre, C., Correlation between Maximum Water/Electrolyte Solubilizat1on and Conductivity Percolation in Aot Reversed Micelles. *J Disper Sci Technol.* **1991**, *12*, 517-530.
133. Mathew, C.; Patanjali, P. K.; Nabi, A.; Maitra, A., On the Concept of Percolative Conduction in Water-in-Oil Microemulsions. *Colloids and Surfaces* **1988**, *30*, 253-263.
134. Scriven, L. E., Equilibrium Bicontinuous Structure. *Nature* **1976**, *263*, 123.
135. Lindman, B.; Olsson, U., Structure of Microemulsions Studied by Nmr. *Berichte der Bunsengesellschaft für physikalische Chemie* **1996**, *100*, 344-363.
136. Yu, Z.-J.; Neuman, R. D., Reversed Micellar Solution-to-Bicontinuous Microemulsion Transition in Sodium Bis(2-Ethylhexyl) Phosphate/N-Heptane/Water System. *Langmuir* **1995**, *11*, 1081-1086.
137. Moore, S. A.; Palepu, R. M., Fluorometric Investigations on the Transition from Reverse Micelles to Microemulsions in Non-Aqueous Microemulsions. *J. Mol. Liq.* **2007**, *135*, 123-127.
138. Dhand, C.; Dwivedi, N.; Loh, X. J.; Jie Ying, A. N.; Verma, N. K.; Beuerman, R. W.; Lakshminarayanan, R.; Ramakrishna, S., Methods and Strategies for the Synthesis of Diverse Nanoparticles and Their Applications: A Comprehensive Overview. *RSC Advances* **2015**, *5*, 105003-105037.
139. Solanki, J. N.; Murthy, Z. V. P., Controlled Size Silver Nanoparticles Synthesis with Water-in-Oil Microemulsion Method: A Topical Review. *Industrial and Engineering Chemistry Research* **2011**, *50*, 12311-12323.
140. Zhang, S.; Tang, Y.; Vlahovic, B., A Review on Preparation and Applications of Silver-Containing Nanofibers. *Nanoscale Research Letters* **2016**, *11*, 80.
141. Sanchez-Dominguez, M.; Pemartin, K.; Boutonnet, M., Preparation of Inorganic Nanoparticles in Oil-in-Water Microemulsions: A Soft and Versatile Approach. *Curr. Opin. Colloid Interface Sci.* **2012**, *17*, 297-305.

142. Malik, M. A.; Wani, M. Y.; Hashim, M. A., Microemulsion Method: A Novel Route to Synthesize Organic and Inorganic Nanomaterials: 1st Nano Update. *Arabian Journal of Chemistry* **2012**, *5*, 397-417.
143. Boutonnet, M.; Kizling, J.; Stenius, P.; Maire, G., The Preparation of Monodisperse Colloidal Metal Particles from Microemulsions. *Colloids and Surfaces* **1982**, *5*, 209-225.
144. Zhang, W.; Qiao, X.; Chen, J.; Wang, H., Preparation of Silver Nanoparticles in Water-in-Oil Aot Reverse Micelles. *J. Colloid Interface Sci.* **2006**, *302*, 370-373.
145. Zhang, W.; Qiao, X.; Chen, J., Synthesis of Silver Nanoparticles—Effects of Concerned Parameters in Water/Oil Microemulsion. *Mater. Sci. Eng., B* **2007**, *142*, 1-15.
146. Zhang, W.; Qiao, X.; Chen, J., Formation of Silver Nanoparticles in Sds Inverse Microemulsions. *Mater. Chem. Phys* **2008**, *109*, 411-416.
147. Setua, P.; Pramanik, R.; Sarkar, S.; Seth, D.; Sarkar, N., Direct Observation of Solvation Dynamics in an Aqueous Reverse Micellar System Containing Silver Nanoparticles in the Reverse Micellar Core. *J. Phys. Chem. B* **2009**, *113*, 5677-5680.
148. Sun, K.; Qiu, J.; Liu, J.; Miao, Y., Preparation and Characterization of Gold Nanoparticles Using Ascorbic Acid as Reducing Agent in Reverse Micelles. *J. Mater. Sci.* **2009**, *44*, 754-758.
149. Lisiecki, I.; Pileni, M. P., Copper Metallic Particles Synthesized "in Situ" in Reverse Micelles: Influence of Various Parameters on the Size of the Particles. *J. Phys. Chem.* **1995**, *99*, 5077-5082.
150. Cason, J. P.; Roberts, C. B., Metallic Copper Nanoparticle Synthesis in Aot Reverse Micelles in Compressed Propane and Supercritical Ethane Solutions. *J. Phys. Chem. B* **2000**, *104*, 1217-1221.
151. Kitchens, C. L.; McLeod, M. C.; Roberts, C. B., Chloride Ion Effects on Synthesis and Directed Assembly of Copper Nanoparticles in Liquid and Compressed Alkane Microemulsions. *Langmuir* **2005**, *21*, 5166-5173.
152. Bedia, J.; Lemus, J.; Calvo, L.; Rodriguez, J. J.; Gilarranz, M. A., Effect of the Operating Conditions on the Colloidal and Microemulsion Synthesis of Pt in Aqueous Phase. *Colloids Surf. A* **2017**, *525*, 77-84.
153. Noh, J.-H.; Patala, R.; Meijboom, R., Catalytic Evaluation of Dendrimer and Reverse Microemulsion Template Pd and Pt Nanoparticles for the Selective Oxidation of Styrene Using Tbhp. *Appl. Catal., A.* **2016**, *514*, 253-266.
154. Chen, D.-H.; Wu, S.-H., Synthesis of Nickel Nanoparticles in Water-in-Oil Microemulsions. *Chem. Mater.* **2000**, *12*, 1354-1360.
155. Simakova, I. L.; Simonov, M. N.; Demidova, Y. S.; Yu. Murzin, D., Size-Controlled Reverse Microemulsion Synthesis of Ni and Co Metal Nanoparticles. *Materials Today: Proceedings* **2017**, *4*, 11385-11391.
156. Chen, D.-H.; Chen, C.-J., Formation and Characterization of Au-Ag Bimetallic Nanoparticles in Water-in-Oil Microemulsions. *J. Mater. Chem.* **2002**, *12*, 1557-1562.
157. Wang, H.-K.; Yi, C.-Y.; Tian, L.; Wang, W.-J.; Fang, J.; Zhao, J.-H.; Shen, W.-G., Ag-Cu Bimetallic Nanoparticles Prepared by Microemulsion Method as Catalyst for Epoxidation of Styrene. *J Nanomater.* **2012**, *2012*, 8.
158. Wu, M.-L.; Chen, D.-H.; Huang, T.-C., Preparation of Au/Pt Bimetallic Nanoparticles in Water-in-Oil Microemulsions. *Chem. Mater.* **2001**, *13*, 599-606.
159. Szumełda, T.; Drelinkiewicz, A.; Kosydar, R.; Góral-Kurbiel, M.; Gurgul, J.; Duraczyńska, D., Formation of Pd-Group Viii Bimetallic Nanoparticles by the "Water-in-Oil" Microemulsion Method. *Colloids Surf. A* **2017**, *529*, 246-260.

160. Kim, T.; Kobayashi, K.; Nagai, M., Preparation and Characterization of Platinum-Ruthenium Bimetallic Nanoparticles Using Reverse Microemulsions for Fuel Cell Catalyst. *J Oleo Sci.* **2007**, *56*, 553-562.
161. Ghiaci, M.; Aghaei, H.; Abbaspourrad, A., *Size-Controlled Synthesis of Zro2–Tio2 Nanoparticles Prepared Via Reverse Micelle Method: Investigation of Particle Size Effect on the Catalytic Performance in Vapor Phase Beckmann Rearrangement*, 2008; Vol. 43, p 1255–1262.
162. Jha, M.; Kumar, S.; Garg, N.; Ramanujachary, K. V.; Lofland, S. E.; Ganguli, A. K., Microemulsion Based Approach for Nanospheres Assembly into Anisotropic Nanostructures of Nimno3 and Their Magnetic Properties. *J. Solid State Chem.* **2018**, *258*, 722-727.
163. Chiu, Y.-W.; Huang, M. H., Formation of Hexabranched Geo2 Nanoparticles Via a Reverse Micelle System. *J. Phys. Chem. C* **2009**, *113*, 6056-6060.
164. Finnie, K. S.; Bartlett, J. R.; Barbé, C. J. A.; Kong, L., Formation of Silica Nanoparticles in Microemulsions. *Langmuir* **2007**, *23*, 3017-3024.
165. Nassar, N.; Husein, M., Preparation of Iron Oxide Nanoparticles from Fecl3 Solid Powder Using Microemulsions. *physica status solidi (a)* **2006**, *203*, 1324-1328.
166. Sharma, S.; Pal, N.; Chowdhury, P. K.; Sen, S.; Ganguli, A. K., Understanding Growth Kinetics of Nanorods in Microemulsion: A Combined Fluorescence Correlation Spectroscopy, Dynamic Light Scattering, and Electron Microscopy Study. *J. Am. Chem. Soc.* **2012**, *134*, 19677-19684.
167. Sharma, S.; Yadav, N.; Chowdhury, P. K.; Ganguli, A. K., Controlling the Microstructure of Reverse Micelles and Their Templating Effect on Shaping Nanostructures. *J. Phys. Chem. B* **2015**, *119*, 11295-11306.
168. Setua, P.; Ghatak, C.; Rao, V. G.; Das, S. K.; Sarkar, N., Dynamics of Solvation and Rotational Relaxation of Coumarin 480 in Pure Aqueous-Aot Reverse Micelle and Reverse Micelle Containing Different-Sized Silver Nanoparticles inside Its Core: A Comparative Study. *J. Phys. Chem. B* **2012**, *116*, 3704-3712.
169. Zhang, W.; Qiao, X.; Chen, J.; Wang, H., Preparation of Silver Nanoparticles in Water-in-Oil Aot Reverse Micelles. *J. Colloid. Int. Sci.* **2006**, *302*, 370-373.
170. Zhang, W.; Qiao, X.; Chen, J., Synthesis of Nanosilver Colloidal Particles in Water/Oil Microemulsion. *Colloids Surf. A* **2007**, *299*, 22-28.
171. Zhang, J.; Han, B.; Liu, J.; Zhang, X.; He, J.; Liu, Z.; Jiang, T.; Yang, G., Recovery of Silver Nanoparticles Synthesized in Aot/C12e4 Mixed Reverse Micelles by Antisolvent Co2. *Chem. Eur. J.* **2002**, *8*, 3879-3883.
172. Bagwe, R. P.; Khilar, K. C., Effects of Intermicellar Exchange Rate on the Formation of Silver Nanoparticles in Reverse Microemulsions of Aot. *Langmuir* **2000**, *16*, 905-910.
173. Egorova, E. M.; Revina, A. A., Synthesis of Metallic Nanoparticles in Reverse Micelles in the Presence of Quercetin. *Colloids Surf. A* **2000**, *168*, 87-96.
174. Setua, P.; Chakraborty, A.; Seth, D.; Bhatta, M. U.; Satyam, P. V.; Sarkar, N., Synthesis, Optical Properties, and Surface Enhanced Raman Scattering of Silver Nanoparticles in Nonaqueous Methanol Reverse Micelles. *J. Phys. Chem. C* **2007**, *111*, 3901-3907.
175. Solanki, J. N.; Murthy, Z. V. P., Highly Monodisperse and Sub-Nano Silver Particles Synthesis Via Microemulsion Technique. *Colloids Surf. A* **2010**, *359*, 31-38.
176. Setua, P.; Pramanik, R.; Sarkar, S.; Ghatak, C.; Das, S. K.; Sarkar, N., Synthesis of Silver Nanoparticle inside the Nonaqueous Ethylene Glycol Reverse Micelle and a Comparative Study to Show the Effect of the Nanoparticle on the Reverse Micellar

Aggregates through Solvation Dynamics and Rotational Relaxation Measurements. *J. Phys. Chem. B* **2010**, *114*, 7557-7564.
177. Zhang, W.; Qiao, X.; Chen, J., Synthesis and Characterization of Silver Nanoparticles in Aot Microemulsion System. *Chem. Phys.* **2006**, *330*, 495-500.
178. Henglein, A., Physicochemical Properties of Small Metal Particles in Solution: "Microelectrode" Reactions, Chemisorption, Composite Metal Particles, and the Atom-to-Metal Transition. *J. Phys. Chem.* **1993**, *97*, 5457-5471.
179. Peng, S.; McMahon, J. M.; Schatz, G. C.; Gray, S. K.; Sun, Y., Reversing the Size-Dependence of Surface Plasmon Resonances. *Proc. Nat. Acad. Sci.* **2010**, *107*, 14530-14534.
180. Durantini, A. M.; Darío Falcone, R.; Silber, J. J.; Mariano Correa, N., More Evidence on the Control of Reverse Micelles Sizes. Combination of Different Techniques as a Powerful Tool to Monitor Aot Reversed Micelles Properties. *J. Phys. Chem. B* **2013**, *117*, 3818-3828.
181. Swinehart, D. F., The Beer-Lambert Law. *J. Chem. Educ.* **1962**, *39*, 333.
182. Valeur, B., *Molecular Fluorescence: Principles and Applications*; Wiley, 2002.
183. Isenberg, I.; Dyson, R. D.; Hanson, R., Studies on the Analysis of Fluorescence Decay Data by the Method of Moments. *Biophys. J.* **1973**, *13*, 1090-1115.
184. Ware, W. R.; Doemeny, L. J.; Nemzek, T. L., Deconvolution of Fluorescence and Phosphorescence Decay Curves. Least-Squares Method. *J. Phys. Chem.* **1973**, *77*, 2038-2048.
185. Gafni, A.; Modlin, R. L.; Brand, L., Analysis of Fluorescence Decay Curves by Means of the Laplace Transformation. *Biophys. J.* **1975**, *15*, 263-280.
186. Small, E. W., [11] Method of Moments and Treatment of Nonrandom Error. In *Methods Enzymol.*, Academic Press: 1992; Vol. 210, pp 237-279.
187. Becker, W.; Hickl, H.; Zander, C.; Drexhage, K. H.; Sauer, M.; Siebert, S.; Wolfrum, J., Time-Resolved Detection and Identification of Single Analyte Molecules in Microcapillaries by Time-Correlated Single-Photon Counting (Tcspc). *Rev. Sci. Instrum.* **1999**, *70*, 1835-1841.
188. Livesey, A. K.; Brochon, J. C., Analyzing the Distribution of Decay Constants in Pulse-Fluorimetry Using the Maximum Entropy Method. *Biophys. J.* **1987**, *52*, 693-706.
189. Kawski, A., Fluorescence Anisotropy: Theory and Applications of Rotational Depolarization. *Crit. Rev. Anal. Chem.* **1993**, *23*, 459-529.
190. Jameson, D. M.; Croney, J. C.; Moens, P. D. J., [1] Fluorescence: Basic Concepts, Practical Aspects, and Some Anecdotes. In *Methods Enzymol.*, Academic Press: 2003; Vol. 360, pp 1-43.
191. Maroncelli, M.; Fleming, G. R., Picosecond Solvation Dynamics of Coumarin 153: The Importance of Molecular Aspects of Solvation. *J. Chem. Phys.* **1987**, *86*, 6221-6239.
192. Broglia, M. F.; Gómez, M. L.; Bertolotti, S. G.; Montejano, H. A.; Previtali, C. M., Photophysical Properties of Safranine and Phenosafranine. *J. Photochem. Photobiol. A* **2005**, *173*, 115-120.
193. Brannon, J. H.; Magde, D., Absolute Quantum Yield Determination by Thermal Blooming. Fluorescein. *J. Phys. Chem.* **1978**, *82*, 705-709.
194. Solanki, J. N.; Murthy, Z. V. P., Highly Monodisperse and Sub-Nano Silver Particles Synthesis Via Microemulsion Technique. *Colloids Surf A* **2010**, *359*, 31-38.
195. Zhang, W.; Qiao, X.; Chen, J., Synthesis of Nanosilver Colloidal Particles in Water/Oil Microemulsion. *Colloids Surf A* **2007**, *299*, 22-28.

196. Jana, N. R.; Gearheart, L.; Murphy, C. J., Wet Chemical Synthesis of High Aspect Ratio Cylindrical Gold Nanorods. *J. Phys. Chem. B* **2001**, *105*, 4065-4067.
197. Yang, X.-H.; Ling, J.; Peng, J.; Cao, Q.-E.; Wang, L.; Ding, Z.-T.; Xiong, J., Catalytic Formation of Silver Nanoparticles by Bovine Serum Albumin Protected-Silver Nanoclusters and Its Application for Colorimetric Detection of Ascorbic Acid. *Spectrochim. Acta A* **2013**, *106*, 224-230.
198. Li, H.; Xia, H.; Wang, D.; Tao, X., Simple Synthesis of Monodisperse, Quasi-Spherical, Citrate-Stabilized Silver Nanocrystals in Water. *Langmuir* **2013**, *29*, 5074-5079.
199. Lee, G.-J.; Shin, S.-I.; Kim, Y.-C.; Oh, S.-G., Preparation of Silver Nanorods through the Control of Temperature and Ph of Reaction Medium. *Mater. Chem. Phys.* **2004**, *84*, 197-204.
200. Velikov, K. P.; Zegers, G. E.; van Blaaderen, A., Synthesis and Characterization of Large Colloidal Silver Particles. *Langmuir* **2003**, *19*, 1384-1389.
201. Sondi, I.; Goia, D. V.; Matijević, E., Preparation of Highly Concentrated Stable Dispersions of Uniform Silver Nanoparticles. *J. Colloid Interface Sci.* **2003**, *260*, 75-81.
202. Fathi, H.; Kelly, J. P.; Vasquez, V. R.; Graeve, O. A., Ionic Concentration Effects on Reverse Micelle Size and Stability: Implications for the Synthesis of Nanoparticles. *Langmuir* **2012**, *28*, 9267-9274.
203. Peña, O.; Pal, U., Scattering of Electromagnetic Radiation by a Multilayered Sphere. *Comput. Phys. Commun.* **2009**, *180*, 2348-2354.
204. Solanki, J. N.; Murthy, Z. V. P., Controlled Size Silver Nanoparticles Synthesis with Water-in-Oil Microemulsion Method: A Topical Review. *Ind. Eng. Chem. Res.* **2011**, *50*, 12311-12323.
205. Kamruzzaman, M.; Alam, A.-M.; Kim, K. M.; Lee, S. H.; Suh, Y. S.; Kim, Y. H.; Kim, S. H.; Oh, S. H., Enhanced Luminescence of Lanthanide Complexes by Silver Nanoparticles for Ciprofloxacin Determination. *J. Nanosci. Nanotechno.* **2012**, *12*, 6125-6130.
206. Kim, K.-S.; Kim, H.; Kim, J.-H.; Kim, J.-H.; Lee, C.-L.; Laquai, F.; Yoo, S. I.; Sohn, B.-H., Correlation of Micellar Structures with Surface-Plasmon-Coupled Fluorescence in a Strategy for Fluorescence Enhancement. *J. Mater. Chem.* **2012**, *22*, 24727-24733.
207. Dey, S.; Mandal, U.; Adhikari, A.; Ghosh, S.; Bhattacharyya, K., Probing Dynamic Heterogeneity in Nanoconfined Systems: The Femtosecond Excitation Wavelength Dependence and Fluorescence Correlation Spectroscopy. In *Hydrogen Bonding and Transfer in the Excited State*, John Wiley & Sons, Ltd: 2010; pp 159-174.
208. Satoh, T.; Okuno, H.; Tominaga, K.; Bhattacharyya, K., Excitation Wavelength Dependence of Solvation Dynamics in a Water Pool of a Reversed Micelle. *Chem. Lett.* **2004**, *33*, 1090-1091.
209. Sen, P.; Satoh, T.; Bhattacharyya, K.; Tominaga, K., Excitation Wavelength Dependence of Solvation Dynamics of Coumarin 480 in a Lipid Vesicle. *Chem. Phys. Lett.* **2005**, *411*, 339-344.
210. Sen, P.; Ghosh, S.; Sahu, K.; Mondal, S. K.; Roy, D.; Bhattacharyya, K., A Femtosecond Study of Excitation Wavelength Dependence of Solvation Dynamics in a Peo-Ppo-Peo Triblock Copolymer Micelle. *J. Chem. Phys.* **2006**, *124*, 204905-8.
211. Learmonth, R. P.; Kable, S. H.; Ghiggino, K. P., Basics of Fluorescence. In *Fluorescence Applications in Biotechnology and Life Sciences*, Goldys, E. M., Ed. Wiley-Blackwell, Hoboken, New Jersey, USA: 2009; pp 1-26.

212. Ghosh, H. N., Charge Transfer Emission in Coumarin 343 Sensitized Tio2 Nanoparticle: A Direct Measurement of Back Electron Transfer. *J. Phys. Chem. B* **1999**, *103*, 10382-10387.
213. Singh, P. K.; Kumbhakar, M.; Pal, H.; Nath, S., Modulation in the Solute Location in Block Copolymer−Surfactant Supramolecular Assembly: A Time-Resolved Fluorescence Study. *J. Phys. Chem. B* **2009**, *113*, 1353-1359.
214. Jarzeba, W.; Walker, G. C.; Johnson, A. E.; Kahlow, M. A.; Barbara, P. F., Femtosecond Microscopic Solvation Dynamics of Aqueous Solutions. *J. Phys. Chem.* **1988**, *92*, 7039-7041.
215. Jimenez, R.; Fleming, G. R.; Kumar, P. V.; Maroncelli, M., Femtosecond Solvation Dynamics of Water. *Nature* **1994**, *369*, 471-473.
216. Koti, A. S. R.; Krishna, M. M. G.; Periasamy, N., Time-Resolved Area-Normalized Emission Spectroscopy (Tranes): A Novel Method for Confirming Emission from Two Excited States. *J. Phys. Chem. A* **2001**, *105*, 1767-1771.
217. Koti, A. S. R.; Periasamy, N., Application of Time Resolved Area Normalized Emission Spectroscopy to Multicomponent Systems. *J. Chem. Phys.* **2001**, *115*, 7094-7099.
218. Sarkar, N.; Das, K.; Datta, A.; Das, S.; Bhattacharyya, K., Solvation Dynamics of Coumarin 480 in Reverse Micelles. Slow Relaxation of Water Molecules. *J. Phys. Chem.* **1996**, *100*, 10523-10527.
219. Fee, R. S.; Maroncelli, M., Estimating the Time-Zero Spectrum in Time-Resolved Emmsion Measurements of Solvation Dynamics. *Chem. Phys.* **1994**, *183*, 235-247.
220. Correa, N. M.; Levinger, N. E., What Can You Learn from a Molecular Probe? New Insights on the Behavior of C343 in Homogeneous Solutions and Aot Reverse Micelles. *J. Phys. Chem. B* **2006**, *110*, 13050-13061.
221. Riter, R. E.; Undiks, E. P.; Levinger, N. E., Impact of Counterion on Water Motion in Aerosol Ot Reverse Micelles. *J. Am. Chem. Soc.* **1998**, *120*, 6062-6067.
222. Sugimoto, T., Underlying Mechanisms in Size Control of Uniform Nanoparticles. *J. Colloid Interface Sci.* **2007**, *309*, 106-118.
223. Lemyre, J.-L.; Lamarre, S. b.; Beaupré, A.; Ritcey, A. M., Mechanism of Yf3 Nanoparticle Formation in Reverse Micelles. *Langmuir* **2011**, *27*, 11824-11834.
224. Destrée, C.; B.Nagy, J., Mechanism of Formation of Inorganic and Organic Nanoparticles from Microemulsions. *Adv. Colloid Interface Sci.* **2006**, *123–126*, 353-367.
225. Dutt, G. B., Fluorescence Anisotropy of Ionic Probes in Aot Reverse Micelles: Influence of Water Droplet Size and Electrostatic Interactions on Probe Dynamics. *J. Phys. Chem. B* **2008**, *112*, 7220-7226.
226. Das, P.; Chakrabarty, A.; Mallick, A.; Chattopadhyay, N., Photophysics of a Cationic Biological Photosensitizer in Anionic Micellar Environments: Combined Effect of Polarity and Rigidity. *J. Phys. Chem. B* **2007**, *111*, 11169-11176.
227. Rodarte, A. L.; Tao, A. R., Plasmon–Exciton Coupling between Metallic Nanoparticles and Dye Monomers. *J. Phys. Chem. C* **2017**, *121*, 3496-3502.
228. Faucheaux, J. A.; Fu, J.; Jain, P. K., Unified Theoretical Framework for Realizing Diverse Regimes of Strong Coupling between Plasmons and Electronic Transitions. *J. Phys. Chem. C* **2014**, *118*, 2710-2717.
229. Petit, C.; Lixon, P.; Pileni, M. P., In Situ Synthesis of Silver Nanocluster in Aot Reverse Micelles. *J. Phys. Chem.* **1993**, *97*, 12974-12983.

230. Morales, D.; Gutiérrez, J. M.; García-Celma, M. J.; Solans, Y. C., A Study of the Relation between Bicontinuous Microemulsions and Oil/Water Nano-Emulsion Formation. *Langmuir* **2003**, *19*, 7196-7200.
231. Hazra, P.; Chakrabarty, D.; Sarkar, N., Solvation Dynamics of Coumarin 153 in Aqueous and Non-Aqueous Reverse Micelles. *Chem. Phys. Lett.* **2003**, *371*, 553-562.
232. Durantini, A. M.; Falcone, R. D.; Anunziata, J. D.; Silber, J. J.; Abuin, E. B.; Lissi, E. A.; Correa, N. M., An Interesting Case Where Water Behaves as a Unique Solvent. 4-Aminophthalimide Emission Profile to Monitor Aqueous Environment. *J. Phys. Chem. B* **2013**, *117*, 2160-2168.
233. Chattopadhyay, A.; Haldar, S., Dynamic Insight into Protein Structure Utilizing Red Edge Excitation Shift. *Acc. Chem. Res.* **2014**, *47*, 12-19.
234. Chattopadhyay, A.; Mukherjee, S., Red Edge Excitation Shift of a Deeply Embedded Membrane Probe: Implications in Water Penetration in the Bilayer. *J. Phys. Chem. B* **1999**, *103*, 8180-8185.
235. Kelkar, D. A.; Chattopadhyay, A., Depth-Dependent Solvent Relaxation in Reverse Micelles: A Fluorescence Approach. *J. Phys. Chem. B* **2004**, *108*, 12151-12158.
236. Mukherjee, S.; Sahu, K.; Roy, D.; Mondal, S. K.; Bhattacharyya, K., Solvation Dynamics of 4-Aminophthalimide in Dioxane–Water Mixture. *Chem. Phys. Lett.* **2004**, *384*, 128-133.
237. Zulauf, M.; Eicke, H. F., Inverted Micelles and Microemulsions in the Ternary System Water/Aerosol-Ot/Isooctane as Studied by Photon Correlation Spectroscopy. *J. Phys. Chem.* **1979**, *83*, 480-486.
238. Baddiel, C. B.; Tait, M. J.; Janz, G. J., Nonaqueous Silver Nitrate Solutions. Spectral Studies in Acetonitrile. *J. Phys. Chem.* **1965**, *69*, 3634-3638.
239. Shoeib, T.; El Aribi, H.; Siu, K. W. M.; Hopkinson, A. C., A Study of Silver (I) Ion−Organonitrile Complexes: Ion Structures, Binding Energies, and Substituent Effects. *J. Phys. Chem. A* **2001**, *105*, 710-719.
240. Godfrey Chang, T.-c.; Irish, D., Solvation and Lon Association in the System Agno3−Ch3cn: A Raman and Infrared Spectral Study. *J Solution Chem* **1974**, *3*, 161-174.
241. Shalmashi, A.; Eliassi, A., Solubility of L-(+)-Ascorbic Acid in Water, Ethanol, Methanol, Propan-2-Ol, Acetone, Acetonitrile, Ethyl Acetate, and Tetrahydrofuran from (293 to 323) K. *J. Chem. Eng. Data* **2008**, *53*, 1332-1334.
242. Singha, D.; Sahu, D. K.; Sahu, K., Anomalous Spectral Modulation of 4-Aminophthalimide inside Acetonitrile/Aot/N-Heptane Microemulsion: New Insights on Reverse Micelle to Bicontinuous Microemulsion Transition. *J. Phys. Chem. B* **2018**, *122*, 6966-6974.
243. Bulavchenko, A. I.; Popovetskiy, P. S., Structure of Adsorption Layer of Silver Nanoparticles in Sodium Bis(2-Ethylhexyl) Sulfosuccinate Solutions in N-Decane as Observed by Photon-Correlation Spectroscopy and Nonaqueous Electrophoresis. *Langmuir* **2014**, *30*, 12729-12735.
244. Jiang, X. C.; Chen, W. M.; Chen, C. Y.; Xiong, S. X.; Yu, A. B., Role of Temperature in the Growth of Silver Nanoparticles through a Synergetic Reduction Approach. *Nanoscale Res. Lett.* **2011**, *6*, 32-32.
245. Qin, Y.; Ji, X.; Jing, J.; Liu, H.; Wu, H.; Yang, W., Size Control over Spherical Silver Nanoparticles by Ascorbic Acid Reduction. *Colloids Surf. A* **2010**, *372*, 172-176.

246. Wei, J.; Schaeffer, N.; Albouy, P.-A.; Pileni, M.-P., Surface Plasmon Resonance Properties of Silver Nanocrystals Differing in Size and Coating Agent Ordered in 3d Supracrystals. *Chem. Mater.* **2015**, *27*, 5614-5621.
247. Reyes, P. Y.; Espinoza, J. A.; Trevino, M. E.; Saade, H.; Lopez, R. G., Synthesis of Silver Nanoparticles by Precipitation in Bicontinuous Microemulsions. *J. Nanomater.* **2010**, *2010*, 7.
248. Latsuzbaia, R.; Negro, E.; Koper, G., Bicontinuous Microemulsions for High Yield, Wet Synthesis of Ultrafine Nanoparticles: A General Approach. *Faraday Discussions* **2015**, *181*, 37-48.